

PROCESSING AND MECHANICAL PROPERTY ANALYSIS OF CLOSED-CELL ALUMINUM FOAM

A THESIS

*Submitted in partial fulfilment of the
requirements for the award of the degree*

of

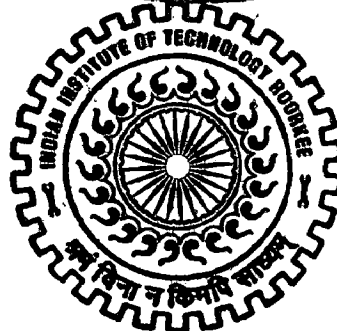
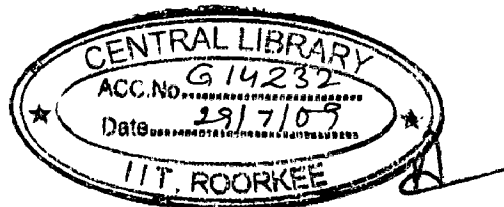
DOCTOR OF PHILOSOPHY

in

METALLURGICAL AND MATERIALS ENGINEERING

by

EDWIN RAJ R



DEPARTMENT OF METALLURGICAL AND MATERIALS ENGINEERING
INDIAN INSTITUTE OF TECHNOLOGY ROORKEE

ROORKEE-247 667 (INDIA)

MAY, 2008

**©INDIAN INSTITUTE OF TECHNOLOGY ROORKEE, ROORKEE, 2008
ALL RIGHTS RESERVED**



**INDIAN INSTITUTE OF TECHNOLOGY ROORKEE
ROORKEE**


CANDIDATE'S DECLARATIONS

I hereby certify that the work which is being presented in the thesis entitled **PROCESSING AND MECHANICAL PROPERTY ANALYSIS OF CLOSED-CELL ALUMINUM FOAM** in partial fulfilment of the requirements for the award of the degree of Doctor of Philosophy, submitted in the Department of Metallurgical and Materials Engineering, Indian Institute of Technology Roorkee, is an authentic record of my own work carried out during a period from January 2005 to May 2008 under the supervision of Dr. B.S.S. Daniel, Assistant Professor, Department of Metallurgical and Materials Engineering, Indian Institute of Technology Roorkee, Roorkee.

The matter embodied in this thesis has not been submitted by me for the award of any other degree of this or any other Institute.


(EDWIN RAJ R)

This is to certify that the above statement made by the candidate is correct to the best of my knowledge.


(B.S.S. DANIEL)
Supervisor

Date: 23 May, 2008

The Ph.D. Viva-Voce Examination of **Mr. Edwin Raj R**, Research Scholar, has been held on _____.

Signature of Supervisor

Signature of External Examiner

SYNOPSIS

Metal foams are a unique class of engineering material consisting of a rather uniform distribution of deliberately introduced void spaces. Unlike casting defects the void fraction in metal foams is fairly large, often exceeding 70 volume %. The void cavities in closed-cell metal foams are insulated from each other by the cell wall material. The relative density, which is the ratio of the density of foam to the solid material, is generally used to characterize the foam structure. Metal foams have received considerable attention in recent years due to their unique combination of properties which lend them to applications such as impact/blast energy absorption, light weight structures, sound and vibration absorption.

In recent years, several new cost effective foaming techniques are available to make metal foams with better structural control. While melt foaming route to produce closed-cell aluminum foam has the potential for commercialization, processing challenges to produce specified foam structure still exists. The mechanical property of the closed-cell aluminum foam formed by degassing titanium hydride (TiH_2) in molten aluminum is dependent on the structural parameters, such as, the relative density, pore size, cell wall thickness and aspect ratio. On the other hand, the structural parameters themselves are a function of the process parameters, such as the melt viscosity, amount of TiH_2 addition and the duration allowed for degassing. An objective of the present work is to use existing modelling techniques to establish a processing-structure-property correlation which could serve as a design guide for aluminum foam manufacture.

Chapter 1 consists of an introduction to metallic foams as a special class of engineering material with unique set of properties which can be tailored to meet specific light weight structural requirements. In chapter 2, an overview of the state of scientific and applied knowledge of metal foams with regard to processing and properties is presented. Three manufacturing methods hold promise for mass production of aluminum foam, namely, (1) powder metallurgy route, (2) melt foaming by gas injection and (3) melt foaming with blowing agents. The present work concerns the aluminum melt foaming by the decomposition of titanium hydride. Foam stability is an important parameter which establishes the time window within which the liquid foam has to be developed and quenched to solidify the structure. An understanding of the mechanism of liquid foaming is essential to improve foam stability and establish control over the foaming process.

The literature on the mechanical property of aluminum foam, such as compression modulus, plateau stress, tensile property and energy absorption is discussed along with the application potential. Analytical modelling attempts by various researches are briefed of which the Gibson and Ashby model for predicting the Young's modulus and plateau stress is the most popular. The prediction is based on the relative density, cell wall material property and a structural parameter, ϕ , which is the fraction of solid in the cell edges. Several are those reported difficulties while comparing their results with the Gibson and Ashby model. For this reason statistical modelling approach is taken to correlate the structure to the mechanical property for the first time in this work.

Chapter 3, which is titled 'Experimental procedure and the modelling tools' gives the details of the experimental and modelling tools used in this work. A special purpose top opening resistance heating furnace was designed and fabricated to process aluminum foam. Calcium is added to the melted aluminum alloy in the crucible and stirred for a stipulated period. Once the melt viscosity is appropriated, TiH_2 is added and stirred at a higher speed. Subsequently, the stirrer is removed and held inside the furnace for different holding time for foaming. Once the foams were made, structural and microstructural characterizations were carried out. The structural analysis included the relative density, average cell size and cell aspect ratio of the foam. The microstructural analysis was carried out using scanning electron microscope (SEM) along with energy dispersive spectroscopy (EDS) to look for elemental distribution within the cell walls. Subsequently, quasi-static compressing test and dynamic impact tests were carried out from which the Young's modulus, plateau stress, energy absorption and strain rate sensitivity data were collected. The later part of the chapter also contains a brief description of the modelling tools such as design of experiments (DOE), multi-linear regression analysis and artificial neural networks (ANN) which were used in this work.

Chapter 4 consists of the results and discussion of the foam process parameters, the mechanical property behaviour, and the modelling of foam processing and properties. By varying the process variables wide range of structural properties of foam are assessed. The relative density of foam obtained ranges from 0.062 to 0.40 with average pore diameter variation from 2.116 to 4.495 mm and having cell aspect ratio between 1.007 and 1.364. Design of experiments (DOE) is used to identify the major influencing parameters and also to determine and control the quality of the finished product. Based on the literature published and by conducting many pilot experiments, the process parameters which are not significant and to bring a focus to the present study, parameters

such as: composition of base alloy, stirrer design, melt temperature, stirrer speed after calcium and TiH₂ addition, holding temperature and solidification rate are maintained the same in all experiments. The process parameters selected for analysis in the first phase of the experimentation with half-fractional factorial design are: (1) amount of calcium metal addition (2) the stirring time after calcium addition (3) amount of TiH₂ addition and (4) the holding time after TiH₂ addition.

An analysis of variance (ANOVA) is then carried out separately for each of the response (structural parameters) in order to test the model signification and suitability. From those observations, it is observed that the amount of TiH₂ addition in the melt and the holding time after dispersing the TiH₂ are the prominent process parameters influencing the foam structure. Therefore, in the second phase of experiments the response surface methodology (RSM) is employed to evaluate the relevance of these two process parameters on the final cell structure in a wider range by central composite design (CCD). It is observed that both the process variables: the amount of TiH₂ added to the melt and the holding time are inversely proportional to the relative density. However, the influence of TiH₂ addition is very high in comparison with holding time. The amount of TiH₂ addition and holding time are directly proportional and have equal influence on the average pore diameter of the final foam structure. Moreover, holding time had more direct influence on the cell aspect ratio than the amount of TiH₂ addition. It is understood that the stable foam structure with less cell aspect ratio and cell wall defects is processed when the amount of TiH₂ addition is near 1.0 wt.% and the holding time around 100 s.

Particle identification of the cell wall material were done by correlating the Energy Dispersive X-ray Spectroscopy (EDS) results with X-ray powder diffraction results obtained in the 2- θ range of 20-90° using Cu K α radiation. It is found that aluminum oxide is only confined to the surface of the pores and the intermetallic particles are present within the cell wall matrix. The foam made using the graphite stirrer had Al₂₀CaTi₂ and Al₂Cu intermetallic particles, whereas the samples prepared with the stainless steel stirrer had Al₁₃Fe₄ intermetallic along with Al₂₀CaTi₂ and Al₂Cu particles dispersed within the cell wall. Al₂Cu lamella is present as fine lamella whereas Al₂₀CaTi₂ is present as blocky precipitates within the cell wall. Al₁₃Fe₄ intermetallic was formed within the matrix by the diffusion of iron from the stainless steel stirrer in spite of the alumina coating of the stirrer, is present as elongated platelets of rather high aspect ratio. Al₂Cu forms only on solidification so it has no influence on foam stability. On the other

hand, $\text{Al}_{20}\text{CaTi}_2$ and $\text{Al}_{13}\text{Fe}_4$ can be present as solids at 730°C in the cell walls and will provide stability to the liquid foam.

Foam specimens are subjected to quasi-static compression testing at the strain rate of $1 \times 10^{-3} \text{ s}^{-1}$. Dynamic impact tests at the strain rate range of about $7.5 \times 10^2 \text{ s}^{-1}$ were carried out on the split Hopkinson pressure bar (SHPB). The test results were analysed for Young's modulus, plateau stress and energy absorption capacity of the foam. It is observed that the mechanical property of aluminum foam depends mainly on their relative density. However, for the same relative density the plateau stress increases with pore diameter which is attributed to the increase in cell wall thickness. Experiments were also being carried out at higher strain rates, commensurate with automobile crash and the results showed strain rate sensitivity, especially at higher relative densities. This result is particularly encouraging for high impact absorption applications as the material displays strain rate hardening.

ANN models are developed for the prediction of compressive properties of closed-cell aluminum foam using the large experimental database from the quasi-static compression test. The input parameters chosen for development of ANN models are the relative density, average pore diameter and cell aspect ratio. All the models developed are of acceptable accuracy within the experimental data range, considering the complexity of the property correlation of metallic foams. These ANN models could be beneficial to the foam manufactures to build more general and particular property database of aluminum foam. Similarly, multiple linear regression models are developed from the observed data by correlating the structural parameters with the compressive properties and found to be satisfactory.

In summary, the closed-cell aluminum foam processing parameters were characterized and the empirical models developed to obtain tailor-made physical and morphological properties. The microstructural analysis of cell wall material has highlighted the role played by the morphology of the intermetallic particle which affect foam stability. The mechanical properties and energy absorption capacity in static and dynamic compression state are evaluated and found to be consistent with requirements for high impact applications. The modelling approach taken to correlate the process parameters to the structural parameter and in turn to the mechanical properties in this work are of acceptable accuracy.

ACKNOWLEDGEMENT

I dedicate this work to my Lord and Saviour, to His glory and honour.

I am grateful to my thesis Supervisor, Dr. B.S.S. Daniel, Assistant Professor, Department of Metallurgical and Materials Engineering, IIT Roorkee for his keen interest in me and my work has made this thesis possible. His warm personal approaches and painstaking efforts in going through the manuscript are gratefully acknowledged.

I am highly obliged to the past and present Heads of the Department of Metallurgical and Materials Engineering, several lab in-charges, and workshop employees, for their cooperation and assistance in carrying out my work. I express a sense of gratitude to all faculty members for their valuable suggestions and help. I am deeply grateful to Dr. P. Venkitanarayanan, Associate Professor, Department of Mechanical Engineering, IITK for his guidance and technical support to carry out dynamic compression test. I wish to thank my fellow research scholars, Mr. Ananth Kumar, Mr. Mahesh Anwar, Mr. Rahul Sharma, Mr. Rajaram Prasad, Dr. Sivalingappa and Mr. Vipin Chawla and my dear friend Mr. Allwyn Abraham for their help during processing and characterization of foam.

My stay in Roorkee was taken care physically, spiritually and socially by my pastor, Rev. Rajan Thomas & family. I thank my supervisor & family, Mr. Christopher & family, Mr. Venkat & family, Mr. Emmanuel & family, Dr. Jacob Reglend & family for the fellowship to cherish. My time here in Roorkee was made purposeful by the tremendous love and affection of the families in the nearby army campus: Mr. Philip & family, Mr. John Varghese & family, Mr. Gunasekaran & family, Mr. Murthy & family, Mr. Palani & family, Mr. Prakash & family and Mr. Arul.

I treasure the happy and sad moments, shared and enjoyed with my friends in IIT campus, especially with Mr. Allwyn Abraham, Mr. Ananth Kumar, Mr. Sathish Kumar & family, Mr. Ganapathy, Mr. Thangaraj & family, Dr. Bala Subramanian & family, Mr. Ramsankaran and Mr. Bala Subramanian.

At this moment, I am thankful to all of my family members and friends back home. I am highly indebted to my mother, in-laws and my sister & family for their support to me and my family. Words cannot express fully the love and affection of my wife and daughter, for being with me as flesh and bone in this endeavour. I am always grateful for you.

R. Edwin Raj

TABLE OF CONTENTS

Candidate's Declaration.....	i
Synopsis.....	iii
Acknowledgement.....	vii
Table of Contents.....	ix
List of Figures.....	xii
List of Tables.....	xxi
List of Abbreviations and Symbols.....	xxiii
Chapter 1- Introduction	
1.0. Introduction.....	1
Chapter 2 - Literature Survey	
2.1. Introduction.....	7
2.2. Metallic Foam Structure	8
2.3. Processing of Metallic Foams.....	10
2.3.1. Powder Metallurgy Route	11
2.3.2. Liquid Melt Route.....	13
2.3.2.1. Direct Gas Injection.....	14
2.3.2.2. Foaming with Blowing Agents.....	15
2.4. The Physics of Foaming.....	17
2.5. Properties of Foam.....	22
2.5.1. Mechanical Property	26
2.5.1.1. Compression Modulus.....	27
2.5.1.2. Compression Plateau Stress.....	28

2.5.1.3. Tensile Property.....	29
2.5.1.4. Energy Absorption Capacity	30
2.5.1.5. Strain Rate Dependency	31
2.5.2. Sound Absorption and Vibration Damping Property.....	32
2.5.3. Electrical and Thermal Property	33
2.6. Applications	34
2.7. Modelling.....	36
2.8. Formulation of Problem.....	38
 Chapter 3 - Experimental Procedure and Modelling Tools	
3.1. Introduction.....	41
3.2. Design and Fabrication of Experimental Set-up.....	42
3.3. Experimental Procedure.....	44
3.4. Characterization Tools	45
3.4.1. Macrostructural Quantification.....	45
3.4.2. X-ray Diffraction (XRD)	46
3.4.3. Optical Microscopy.....	46
3.4.4. Scanning Electron Microscope (SEM) with Energy Dispersive X-ray Spectroscopy (EDS).....	47
3.4.5. Transmission Electron Microscopy (TEM)	48
3.4.6. Thermo Gravimetric Analysis (TGA).....	49
3.4.7. Mechanical Testing.....	49
3.4.7.1. Quasi-Static Compression test.....	49
3.4.7.2. Dynamic compression test.....	51

3.5. Modelling Tools.....	53
3.5.1. Design of Experiments (DOE).....	54
3.5.1.1. Fractional Factorial Design	54
3.5.1.2. Central Composite Design (CCD).....	55
3.5.1.3. Response Surface Methodology (RSM).....	56
3.5.1.4. The Analysis of Variance (ANOVA).....	56
3.5.2. Multiple Linear Regression Model	59
3.5.3. Artificial Neural Network (ANN) Model	60
3.5.3.1. Activation Function	61
3.5.3.2. Learning Rules.....	62
3.5.3.3. Training Process	62

Chapter 4 - Results and Discussion

4.1. Introduction.....	65
4.2. Process Influence on Foam Structure	66
4.2.1. Design of Experiments and Analysis: Phase-I.....	68
4.2.1.1. Analysis of Relative Density Model.....	69
4.2.1.2. Analysis of Average Pore Diameter Model.....	75
4.2.1.3. Analysis of Cell Aspect Ratio Model.....	78
4.2.1.4. Inference from Phase-I Experiments	78
4.2.2. Phase-II: Central Composite Design Experiments and Results.....	79
4.2.2.1. Influence of major Process Parameters on Relative Density.....	80
4.2.2.2. Influence of major Process Parameters on Average Pore Diameter.....	84
4.2.2.3. Influence of major Process Parameters on Cell Aspect Ratio	89

4.3. Microstructural Analysis.....	91
4.3.1. X-ray Diffraction Analysis	92
4.3.2. Electron Microscopy Analysis.....	94
4.3.3. Inference from Microstructural Studies.....	99
4.4. Mechanical Property Analysis	102
4.4.1. Quasi-Static Compression Test.....	103
4.4.1.1. Plateau Stress.....	104
4.4.1.2. Young’s Modulus	107
4.4.1.3. Energy Absorption.....	110
4.4.2. Dynamic Compression Test.....	117
4.5. Statistical Modelling and Analysis	127
4.5.1. Multiple Linear Regression Model	128
4.5.2. Artificial Neural Network Model.....	131
4.5.2.1. Model Development	133
4.5.2.2. Data Analysis.....	134
4.5.2.3. Estimation of Plateau Stress	135
4.5.2.4. Estimation of Young’s Modulus.....	136
4.5.2.5. Estimation of Energy Absorption	139
4.5.3. Inference from Modelling	143
Chapter 5 - Conclusions	143
Chapter 6 - Scope for Future Work	149
References.....	151
List of Publications.....	167

LIST OF FIGURES

Figure No.	Title	Page No.
Fig. 1.1.	Definition of combination of diffusion of one phase in a second phase (Banhart, 1999).	2
Fig. 1.2.	The Young's modulus plotted against the density for the family of materials (Ashby, 2005).	3
Fig. 1.3.	The 'Strength' plotted against the density for the family of materials (Ashby, 2005).	4
Fig. 2.1.	Two-dimensional cellular materials: (a) aluminum honeycomb, (b) paper-phenolic resin honeycomb, (c) ceramic honeycomb with square cells, (d) ceramic honeycomb with triangular cells (Gibson and Ashby, 1997).	8
Fig. 2.2.	Three-dimensional polyhedral cells: (a) tetrahedron, (b) triangular prism, (c) rectangular prism, (d) hexagonal prism, (e) octahedron, (f) rhombic dodecahedron, (g) pentagonal dodecahedron, (h) tetrakaidecahedron, (i) icosahedrons (Gibson and Ashby, 1997).	9
Fig. 2.3.	Powder metallurgy route for foaming closed-cell foam (Banhart and Baumeister, 1998).	11
Fig. 2.4.	Aluminum foam sandwich (AFS) sheet (Seelinger, 2004).	13
Fig. 2.5.	Direct foaming of melts by gas injection in the manufacture of closed-cell foam (Asholt, 1999).	14
Fig. 2.6.	Effect of the amount of calcium addition and stirring time on aluminum melt viscosity at 720°C (Ma and Song, 1998).	16
Fig. 2.7.	The schematic showing the (a) nucleation, (b) growth and (c) migration of the gas bubbles to the surface of the melt.	17
Fig. 2.8.	Expansion ratio and rate of foam verses holding time in foam making process (Song and Nutt, 2007).	18
Fig. 2.9.	SEM image of the closed-cell aluminum foam cell wall showing large convex curvature from the cell wall to the cell edge.	21
Fig. 2.10.	Schematic sketch of the compression stress-strain diagram of Elastomeric, Polymeric and Metallic foams.	23

Fig. 2.11.	Gibson and Ashby model for closed-cell foam (Gibson and Ashby, 1997).	24
Fig. 2.12.	Schematic stress-strain diagram of metal and its foam in compression and tension.	26
Fig. 2.13.	Schematic representation of compressive property determination of foam from the stress-strain curve plot of compression test.	27
Fig. 2.14.	Sound absorption measured in a plane-wave impedance tube for Alporas foam (Ashby et al., 2000).	30
Fig. 2.15.	Multifunctionality of Metallic Foams.	34
Fig. 2.16.	Foam filled aluminum structure for crash energy absorption (Banhart, 2005).	35
Fig. 3.1.	Experimental arrangement used for making aluminum foam.	42
Fig. 3.2.	Photograph of the lid used to cover the top portion of the muffle furnace.	43
Fig. 3.3.	Different types of stirrers used in the manufacture of aluminum foam.	44
Fig. 3.4.	Bisected foam structure for macrostructure characterization.	45
Fig. 3.5.	D8 Advance, Bruker AXS, X-ray diffractometer used for X-ray powder analysis.	46
Fig. 3.6.	Quanta 200 FEG, FEI Company's scanning electron microscopy fitted with EDS for elemental analysis.	47
Fig. 3.7.	TECHNAI 20G2-S-TWIN, FEI Company's 200kV transmission electron microscope.	48
Fig. 3.8.	Pyrio Diamond TG/DTA, Perkin Elmer Instruments, Germany used for thermo gravimetric analysis of TiH ₂ powder.	49
Fig. 3.9.	H25KS/05, Hounsfield, England, universal testing machine used for quasi-static compression test.	50
Fig. 3.10.	Experimental setup of SHPB apparatus for dynamic testing of aluminum foam (Mechanical Engineering Department, IIT Kanpur).	51
Fig. 3.11.	Schematic sketch of the SHPB apparatus used for dynamic testing of aluminum alloy foams	53

Fig. 3.12.	Nonlinear model of a neuron in artificial neural network.	60
Fig. 3.13.	Basic functional forms of the activation functions used in the development of ANN model.	61
Fig. 4.1.	Improper foaming of 6061 aluminum alloy without addition of copper.	66
Fig. 4.2.	(a) Optical micrograph of as received 6061 aluminum alloy and (b) Backscattered SEM image of 6061+4 wt.% Cu+1.0 wt.% Ca cast metal alloy showing Al ₂ Cu intermetallic network.	67
Fig. 4.3.	Thermo gravimetric analysis showing the decomposition TiH ₂ occurs between 510 to 570°C during a 10°C/min scan.	68
Fig.4.4.	Some of the pilot experiment results conducted to identify the significant process variables and their range.	69
Fig. 4.5.	Diagnostic plots for the relative density model (a) normal probability Vs studentized residual and (b) Studentized residual Vs Predicted values.	73
Fig. 4.6.	Perturbation plot for relative density model showing the sensitivity of the individual process parameters in the half-fractional factorial design.	74
Fig. 4.7.	Response surface plot of relative density in relation with the amount of TiH ₂ and holding time (half-fractional factorial design).	74
Fig. 4.8.	Pareto chart of standardized effects signifying the effects of process variables in the design for relative density.	75
Fig. 4.9.	Pareto chart of standardized effects signifying the effects of process variables in the design for the pore diameter.	77
Fig. 4.10.	Response surfaces estimated using the CCD derived empirical model for relative density.	82
Fig. 4.11.	Perturbation plot of response surface quadratic model using CCD for relative density prediction.	83
Fig. 4.12.	Perturbation plot of response surface linear model using CCD for the average pore diameter prediction.	84
Fig. 4.13.	Response surfaces linear model in graphical form for the structural parameter the average pore diameter using CCD.	86
Fig. 4.14.	Plot showing the variation of average pore diameter of foam structure with holding time and the amount of TiH ₂ addition.	87

Fig 4.15.	The effect of holding time (a) 60s, (b) 100s and (c) 140s on average pore diameter of the foam when other parameters are maintained constant. 1.0 wt.% TiH ₂ , 1.0 wt.% Ca and 10 minutes stirring time after Ca addition.	87
Fig. 4.16.	Response surfaces quadratic model in graphical form for the structural parameter cell aspect ratio.	89
Fig. 4.17.	Perturbation plot of response surface quadratic model for the cell aspect ratio model.	90
Fig. 4.18.	(a) Secondary and (b) backscattered SEM image of 6061 aluminum alloy + 4 wt.% copper + 1 wt.% calcium showing Al ₂ Cu intermetallic network.	91
Fig. 4.19.	Elemental line analysis of 6061 aluminum alloy + 4 wt.% Cu +1 wt.% Ca in as cast condition.	92
Fig. 4.20.	Powder XRD pattern of the synthesized foam.	93
Fig. 4.21.	Powder XRD pattern of the extracted particles from the foam after leaching with dilute hydrochloric acid.	93
Fig. 4.22.	SEM microstructure of the foam cell wall along with EDS analysis at different points indicated in the microstructure.	96
Fig. 4.23.	SEM microstructure along with EDS showing the presence of iron intermetallics for some sample made by using stainless steel stirrer.	96
Fig. 4.24.	SEM micrograph and EDS mapping for the various elements present on the cell wall of the foam made with graphite stirrer.	97
Fig. 4.25.	SEM micrograph and EDS mapping for the various elements present on the cell wall of the foam made with stainless steel stirrer.	98
Fig. 4.26.	SEM micrograph and the EDS line mapping (white line on the SEM micrograph) for the various elements present on the cell wall of the foam.	99
Fig 4.27.	TEM bright field image: (a) cell wall material showing sub-grain structures. The diffraction pattern of the region confirms multi-crystalline nature. (b) & (c) nano sized intermetallic particle embedded in aluminum grain. SAD pattern confirms its single crystallinity.	100
Fig. 4.28.	Schematic of the pressure difference between cell face and edge causing movement of cell fluids towards the edge leading to thinning of cell faces/walls.	101

Fig. 4.29.	Macrograph of foam showing cell walls in various stages (1 to 5) of thinning before collapse leading to coalescence.	101
Fig. 4.30.	Stress-strain plot of Al foam with and without iron intermetallic in the cell wall showing different plateau stress behaviour (The numbers in the legends indicates the relative density of the specimen).	102
Fig. 4.31.	Sequence of photograph at different strains during the compression test of Al foam.	103
Fig. 4.32.	Stress-strain plot of closed-cell aluminum foam specimens showing increases plateau stress and reduced densification strain for samples of increasing relative density(The number in the label indicates relative density).	104
Fig. 4.33.	Comparison of the experimental plateau stress values with the Gibson and Ashby model with respect to the corresponding relative densities.	105
Fig. 4.34.	Plateau stress increases with pore diameter for a constant relative density of 0.25 as shown by the trend line.	106
Fig. 4.35.	The experimental results of the Young's modulus for the closed-cell foam with respect to the corresponding relative densities.	108
Fig. 4.36.	The Gibson and Ashby model prediction for the closed-cell foam with respect to the corresponding relative densities.	109
Fig. 4.37.	Experimental results of energy absorption capacity up to densification strain plotted corresponding to the relative densities.	109
Fig. 4.38.	Experimental densification strain of the foam samples showing an inverse trend with respect to relative density.	110
Fig. 4.39.	Typical recorded strain histories by the strain gauges while conducting dynamic compression test in SHPB apparatus on an aluminum foam specimen.	117
Fig. 4.40.	The load histories at the two interface of the sample with the incident and transmitter bar showing equilibrium of forces.	118
Fig. 4.41.	Typical plot showing the strain rate of the specimen and the velocity of striker during a dynamic compression test in SHPB apparatus.	120

Fig. 4.42.	A typical stress-strain plot of foam specimens having 0.24 relative densities tested under dynamic and quasi-static conditions.	120
Fig. 4.43.	Graph showing increase in plateau stress with respect to relative density and also to dynamic compression (higher strain rate) in comparison with quasi-static compression.	121
Fig. 4.44.	Strain rate sensitivity increase with relative density foam as seen by increase in strain rate dependent term.	121
Fig. 4.45.	Macrograph of a specimen after dynamic compression in SHPB apparatus.	122
Fig. 4.46.	Bright field TEM image of sample deformed at a strain rate of 750 s^{-1} showing increased dislocation activity within the cell wall.	123
Fig. 4.47.	Graph showing increase in energy absorption capacity up to 8% strain with respect to relative density and strain rate during compression.	124
Fig. 4.48.	Regression model predicted plateau stress values compared with experimental results.	129
Fig. 4.49.	Comparison of the Young's modulus prediction values by regression model with the experimental values.	130
Fig. 4.50.	Comparison of the energy absorption capacity prediction values by regression model with the experimental values.	131
Fig. 4.51.	Typical schematic diagram of the feed forward neural network used for the development of models.	132
Fig. 4.52.	Scattered distribution of average pore diameter of the foam with respect to relative density showing complex dependence.	133
Fig. 4.53.	Plateau stress variation with respect to average pore diameter showing a fully random and scattered plot.	134
Fig. 4.54.	Mean square error convergence during training of the ANN model 3-8-9-1 for plateau stress.	135
Fig. 4.55.	Predicted values of the test patterns for the plateau stress along with experimental values.	136
Fig. 4.56.	ANN model simulation results compared with experimental results for plateau stress shown along with the perfect match line.	136

Fig. 4.57.	Mean square error convergence during training of the ANN model 3-2-1 for Young's modulus.	137
Fig. 4.58.	Predicted values of the test patterns for the Young's modulus along with experimental values.	138
Fig.4.59.	ANN model simulation results compared with experimental results for Young's modulus shown along with the perfect match line.	138
Fig. 4.60.	Training performance plot showing convergence of MSE of the ANN model I 3-6-6-1 for energy absorption capacity evaluation.	139
Fig. 4.61.	Testing results of the ANN model I 3-6-6-1 for energy absorption prediction.	140
Fig. 4.62.	Performance evaluation of model I simulation results for energy absorption capacity in comparison with experimental values.	140
Fig. 4.63.	Training performance plot showing convergence of MSE of the ANN model II 2-2-4-1 for energy absorption capacity evaluation.	141
Fig. 4.64.	Testing results of the ANN model II 2-2-4-1 for energy absorption prediction.	142
Fig. 4.65.	Performance evaluation of model II simulation results for energy absorption by comparison with the experimental values.	142

LIST OF ABBREVIATIONS AND SYMBOLS

ΔP - Capillary pressure, the pressure difference across a curved surface

AFS - Aluminum foam sandwich

A_i - Cross-sectional area of the incident bar

ANN – Artificial Neural Network

ANOVA - Analysis of variance

A_{sp} - Cross-sectional area of the specimen

A_t - Cross-sectional area of the transmitter bar

c – Velocity of sound

CCD - Central Composite Design

DOE – Design of Experiments

E^* - Modulus of the foam

EDS - Energy Dispersive X-ray Spectroscopy

EIA - Energy Information Administration

EPMA - Electron Probe Micro-Analyzer

E_s - Modulus of the cell wall material

f – Frequency

P_e - Pressure on the melt at the cell edges

P_f - Pressure of the melt at the cell faces

p_i - Incident wave

P_m - Inner pressure of a bubble

P_o - Atmospheric pressure

p_r - Reflected wave

PRESS - Prediction Error Sum of Squares

P_{st} - Static pressure of the melt onto the bubble

R - Gas constant

R_1 - Principle radii of the curvature at the edge

R_2 - Principle radii of the curvature at the cell face

RSM - Response Surface Methodology

SAD - Selected Area Diffraction

SEM - Scanning Electron Microscope

SHPB - Split Hopkinson Pressure Bar

TGA - Thermo Gravimetric Analysis

V_b - Volume of the Bubble

V_{st} - Velocity of the Striker

W - Work done or Energy absorption per unit volume

XRD - X-ray Powder Diffraction

α - Absorption coefficient

ε - Strain

ε_d - Densification strain

ε_i - Incident signal

ε_r - Reflected signal

ε_t - Transmitted signal

η - Loss factor

ρ^* - Density of foam

ρ_i - Density of incident bar

ρ_s - Density of the solid material

σ - Surface tension of Al alloy melt

σ_{pl} - Plateau Stress

σ_{sp} - Average compressive stress in the specimen

σ_{ys} - Yield stress of the material

ν - Poisson ratio

φ - Fraction of solid contained in the cell edges

Chapter 1

INTRODUCTION

Cost effective light weight materials with high specific strength have attracted a lot of interest in the field of automotive, rail and aerospace industries, mainly for reduced fuel consumption and CO₂ emission. The double threat of dwindling oil and gas reserves and ever increasing demand for energy has put a heavy premium on growing economies worldwide. The world market oil price has doubled from nearly \$ 50 to \$ 100 a barrel in the period January 2007 to January 2008*. Moreover, governments are increasingly concerned about the greenhouse effect, which has led to stringent vehicular emission norms. Nevertheless, vehicle weight has increased for every successive vehicle generation until 2000AD due to the enhanced vehicle features related to safety, pollution control and comfort-related equipment (Renault, 2008). Light weight vehicle design along with improved aerodynamics and improved engine efficiency are recognised approaches to lower the fuel consumption. Different transport sectors place a different *premium* upon

* Source: EIA, Energy Information Administration, Official energy statistics from the U.S. Government

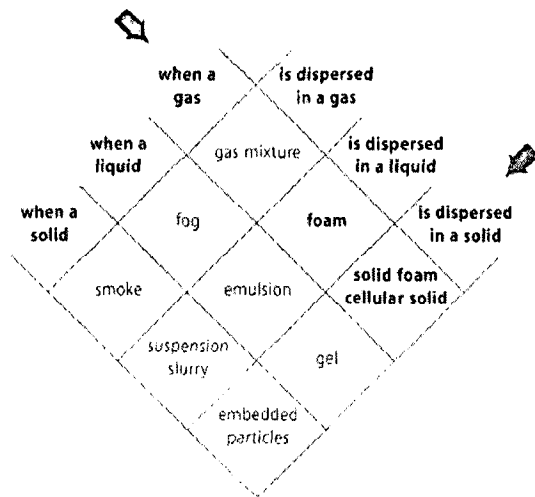


Fig. 1.1. Definition of combination of diffusion of one phase in a second phase (Banhart, 1999).

Carruthers, 2007).

Metallic foams are an important class of engineering material potential usefulness in diverse fields of engineering applications owing to the unique combination of physical, mechanical, thermal and acoustic properties. These attributes offer opportunities to be used for light weight structures, for energy absorption, and for thermal management. Nature's design is unique and all engineering evolves from its principles. Moreover, cellular materials are quite common in nature, such as wood, cork, sponge, coral, bone, etc. The term 'foam' is not always properly defined. Fig. 1.1 describes the possible combinations of dispersing of one phase in another. Foams are nothing but dispersion of gas in a liquid or solid. More specifically, solid foam or cellular solids are dispersion of gaseous phase in a solid. The solid phase is made up of an interconnected network of struts or plates which form the edges and faces of cells. The cell wall material of foams has to be chosen carefully according to the prescribed application. Polymers are flexible and don't possess fire resistance capacity, however ceramics are too brittle to be used for certain applications. Compared with polymeric foams which are widely used, metal foams offer superior properties and can operate at elevated temperatures. These materials are fully recyclable without any pollution or waste problem. It is well understood that the performance of a component is determined by a combination of different properties. For light weight designs, higher strength-to-weight ratios, σ/ρ and higher stiffness-to-weight

the value of light weighting, based on how much each sector is prepared to pay for a lighter alternative part or structure. The comparative savings achieved for weight reduction in automotive, rail and aerospace sector are \$ 3/ kg, \$ 15/kg and \$ 150/kg, respectively. Fuel saving of 5 to 6 % can be achieved for a 10 % drop in the overall vehicular weight. The choice of alternative materials for weight reduction of a certain component is based on quality-reliability, cost, availability and recyclability (Robinson and

ratio, E/ρ are important material attributes. It was Ashby who first combined the properties in a single map and introduced the concept of *merit index* to discriminate among different materials (Ashby, 2005).

The materials property map of modulus versus density chart for different classes of materials is shown in Fig 1.2. The properties of particular family of material tend to cluster together. The density of a solid depends on the atomic weight of its atoms or ions, their size, and the way they are packed. On the other hand, the modulus of most of the materials depends on the bond stiffness (S) and the density of bonds per unit volume. The wide range of moduli is due to varying bond stiffness like stiff covalent bond ($S=20-200$ N/m), or a little lesser metallic or ionic bond ($S=15-100$ N/m) or weak hydrogen or Vander-Waals bonds ($S=0.5-2.0$ N/m). The aluminum foam processed in the present work has density in the range of 0.2 to 1.0 Mg/m^3 and Young's modulus from 0.15 to 2.0 GPa (Indicated by an ellipse in the Ashby map, Fig. 1.2).

The word 'strength' has different connotations in different classes of materials. Strength for metals and polymers refers to yield strength, for ceramics the modulus of

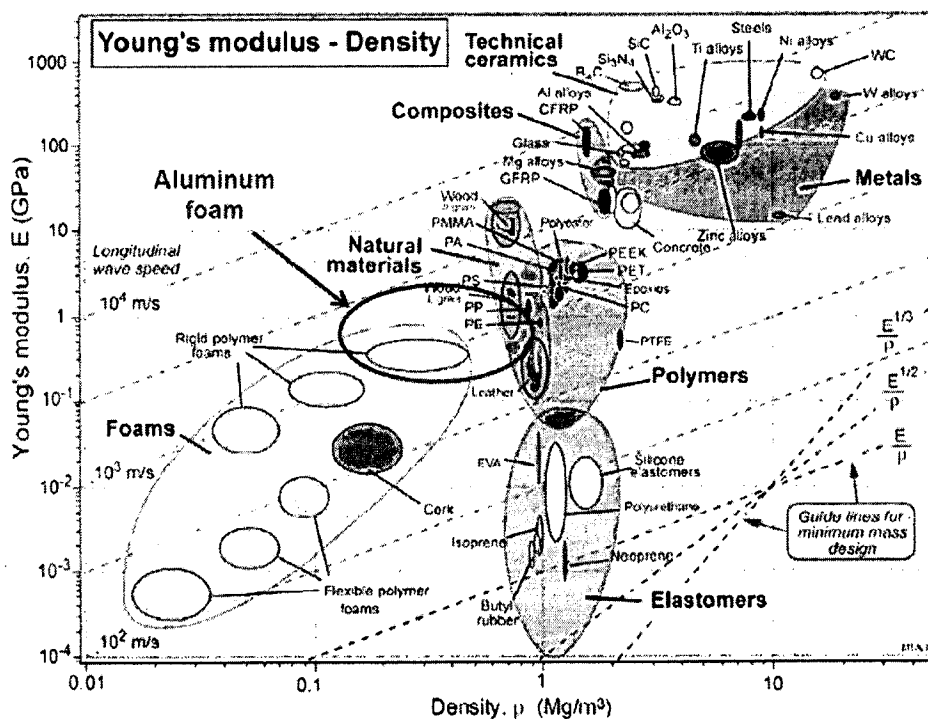


Fig. 1.2. The Young's modulus plotted against the density for the family of materials (Ashby, 2005).

rupture, for elastomers the tear strength and for composites and wood it is the tensile strength. For foam subjected to compressive loads, the word ‘strength’ refers to plateau stress, which is the extended constant stress domain beyond the elastic limit. The strength in general is defined as the lattice resistance to plastic shear. The strength versus density chart is shown in Fig 1.3. Similarly, the aluminum foam processed in this work has the density in the range of 0.2 to 1.0 Mg/m³ and the corresponding strength values range from 2.0 to 25.0 MPa (Indicated by an ellipse in the property map, Fig. 1.3). It may be noted from both the Ashby plots that metal foam properties fall rather far away from metals, ceramics and even composites, but overlap polymers, polymeric foams and natural material. This is certainly useful as it means that metal foams have extended metallic qualities into the polymeric domain. Moreover, the properties fall in such a manner that they exhibit good merit indices and will be competitive replacements for conventional material if their cost effectiveness and reliability can be established.

Metallic foams possess a unique set of properties entirely different from the bulk material due to its cellular nature. From the mechanical properties point of view, two important aspects stand out that lend themselves to several engineering applications.

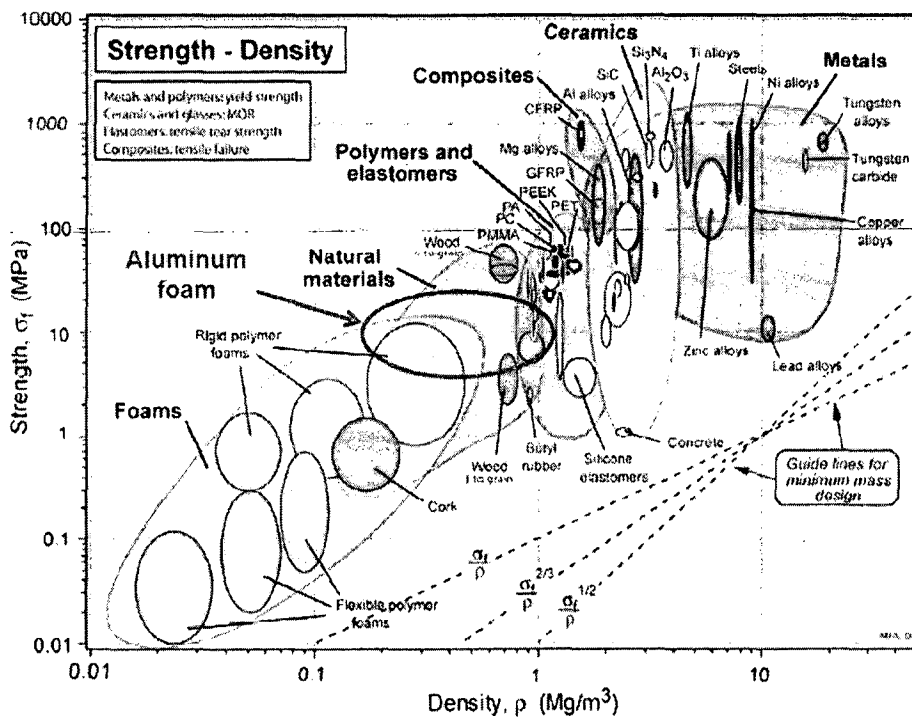


Fig. 1.3. The ‘Strength’ plotted against the density for the family of materials (Ashby, 2005).

Firstly, its high specific strength, if sandwiched between two solid face sheets is useful for light weight structural applications (Schwingel et al., 2007; Demtez and Gibson, 1987; Contorno et al., 2006). Secondly, the large compressive strains at nominally constant stress levels up to densification which is very unique to foams. This phenomenon provides the material the ability to absorb large energy at force levels appropriate for crash and blast protection systems (Nasser et al., 2007; Ramachandra et al., 2003; Sriram et al., 2006; Miyoshi et al., 1999). They hold promise for market penetration in various other applications as well due to the combination of its special features. High sound absorption is another important feature of aluminum foam, especially in the higher frequency range. Damping properties are closely related to relative density, and the loss factor is very high for low density foam. The attributes of aluminum foam in integral armour system add a new dimension on the design of lightweight armoured vehicles and blast protection systems. The increasing demand for passenger safety in the automotive industry would require stronger vehicle body, which would normally translate to building heavier vehicles (Banhart, 2005). This conflicts with the overriding demand for fuel efficiency. Light stiff structures made of aluminum foam, preferably in the form of sandwich panels, could therefore help to reduce weight in automobiles and can also absorb impact energy by exploiting the irreversible plastic deformation in the plateau regime (Baumeister et al, 1997; Edwin and Daniel, 2007a).

The two reasons metallic foams will find acceptance in the auto industry in the near future is weight reduction and safety. While stringent pollution norms and fuel economy drive the former, crash worthiness and passenger safety during impact are increasingly desired features in the passenger car. To achieve weight reduction some auto manufacturers have begun to incorporate magnesium, owing to its low density, good damping characteristics, dimensional stability and excellent machinability notwithstanding the increased cost. It is predicted that the use of magnesium in automobile increase globally at an average rate of 15% per year (Lee et al., 2000). But using metallic foams in structural elements can lead to substantial weight saving as aluminum foam densities are less than half that of magnesium. Before undertaking such a paradigm shift in materials selection the auto industry rightly demands assurance on reliability and cost effectiveness. Aluminum foams have appeared on the materials map as a viable engineering material at the turn of the century. Nevertheless, it remains a

challenge to control the process parameters to synthesize foam with desired properties. The objective of the present work is to understand and qualify the influence of process parameters, and correlate the foam structure with important mechanical properties. It is hoped that a proper understanding of the behaviour of aluminum foam in quasi-static and dynamic impact conditions will go a long way in gaining acceptance in the auto industry.

Chapter 2

LITERATURE REVIEW

2.1. Introduction

In this chapter, the state of scientific and applied knowledge in the field of metallic foams pertaining to processing, properties and modelling is reviewed. In the first part, the foam classification on the basis of structure is introduced and the various processing methods are mentioned thereafter. As the present work pertains to closed-cell metal foam, the three promising manufacturing routes under this category are discussed in detail. The physics of foaming, in particular, the stability of liquid foam during processing is a necessary criteria to achieve uniform cell structure. The salient properties of foam are then reviewed, especially the mechanical properties of foam. The most promising applications of foam are the ones that combine the unique properties of metal foams. For example, the combination of light weight with good energy absorption characteristics is an attractive property for automotive industry. Some promising areas of application of foam are also listed. Modelling and simulation of mechanical foam behaviour is an

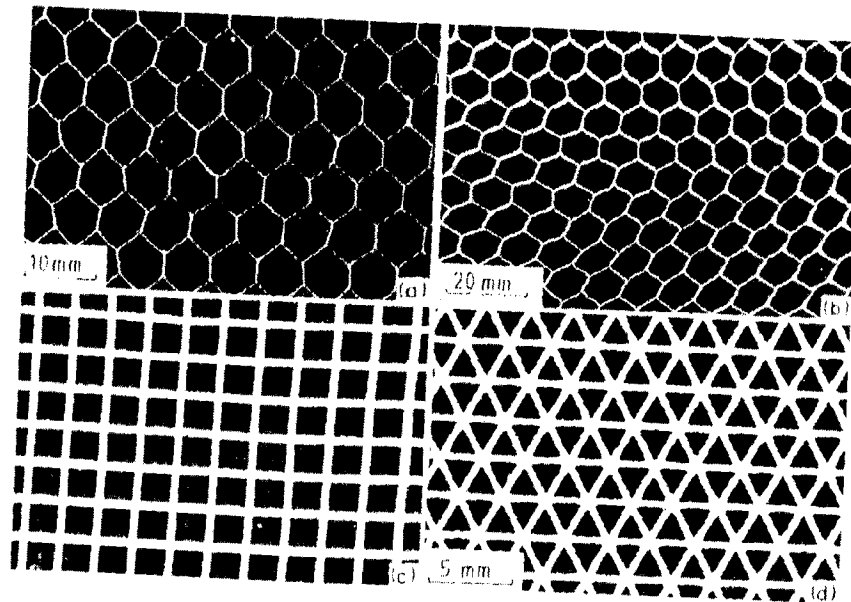


Fig. 2.1. Two-dimensional cellular materials: (a) aluminum honeycomb, (b) paper-phenolic resin honeycomb, (c) ceramic honeycomb with square cells, (d) ceramic honeycomb with triangular cells (Gibson and Ashby, 1997).

important area with renewed interest in the design of metallic foams for specific applications. The Gibson and Ashby model is an elegant analytical approach but falls short as it does not accurately represent the intricacies of the foam structure. Finally, the chapter concludes with an outline of the research problem taken up in the present work.

2.2. Metallic Foam Structure

Metallic foams may be defined as a rather uniform dispersion of pores within a metal. Casting defects such as porosity or cavities which are detrimental to mechanical properties occur randomly and in the worst case are less than 5 % by volume. On the other hand, a structure cannot be classified as foam unless it has more than 70 vol. % porosity. The ideal foam has pores of a fairly uniform size distributed evenly throughout the structure.

Structurally, metallic foams are made up of an interconnected network of struts or plates which form the edges and faces of cells. If the gaseous phase in the cell structure is completely enclosed and is not interconnected with other cells, then by that morphology it is called as closed-cell foam. However, if there is interconnection between the cells, then

it is called open-cell foam. Generally, in cellular solids the two major topological distinctions are: (a) Two dimensional cells in which the cell walls have a common generator as in the case of honey comb and (b) Three dimensional cells in which walls have random orientations in space as in the case of foams. Mathematical modelling of properties of two dimensional structures is easier compared to three dimensional complex geometry of foam. Two dimensional cellular structures are used as sandwich panels, and also for heat exchangers to increase the surface area. Some of the shapes are shown in Fig. 2.1. It can be noted that the edge connectivity is three for hexagonal cellular structure, four for square structure, and six for triangular cellular structure. For certain applications such as buoyant materials and some structural materials closed-cell architectures are preferred, whereas in other cases, such as fluid filtration, catalysis, heat exchangers, biomaterials open-cell architectures are needed. Finding the number of edges meeting at the vertex and to note the edge-connectivity is a challenging task in three dimensional cellular structures.

Analytical modelling approaches have assumed a variety of three dimensional cell structural units to fill space. Some of the possible polyhedral unit cells are shown in Fig. 2.2. However, the structures of real metallic foams are highly irregular, and an exact mathematical description would be untenable. Fortunately, it is generally adequate to

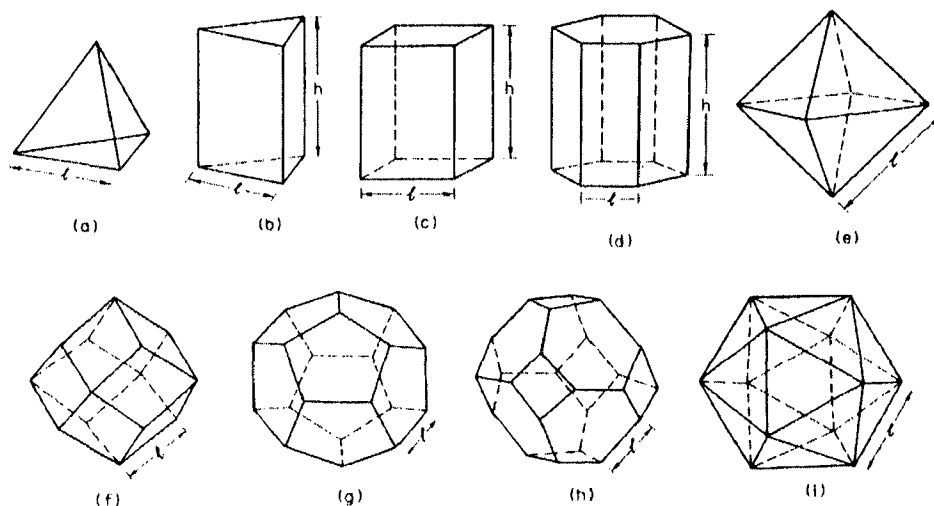


Fig. 2.2. Three-dimensional polyhedral cells: (a) tetrahedron, (b) triangular prism, (c) rectangular prism, (d) hexagonal prism, (e) octahedron, (f) rhombic dodecahedron, (g) pentagonal dodecahedron, (h) tetrakaidecahedron, (i) icosahedrons (Gibson and Ashby, 1997).

represent metallic foam using only a few simple parameters, most importantly relative density, pore size and aspect ratio (Weaire and Hutzler, 1999; Gibson and Ashby, 1997; Ashby et al., 2000). Relative density is the most significant foam property which is related to nearly all important mechanical properties of foam by way of simple scaling relationships (Ashby et al., 2000). The relative density, ρ^*/ρ_s , is the ratio of the density of the foam, ρ^* , to that of the solid material of which it is made, ρ_s . The fraction of pore space or porosity in the foam is given as, $(1 - \rho^*/\rho_s)$. Generally, materials having relative densities less than 0.3 or more than 70% porosity are classified as cellular solids (Gibson and Ashby, 1997).

2.3. Processing of Metallic Foams

The beginning of metallic foam research dates back to when B. Sosnik in 1948 added mercury to molten aluminum to create pores (Sosnik, 1948). In 1956, J.C. Elliot replaced the toxic mercury by foaming agents generating gas by thermal decomposition (Elliot, 1956). Subsequently in 1963 B.C. Allen invented the powder compact foaming technique where the metal powder and foaming agent are blended together, compacted and heated to the melting point which is in the neighbourhood of the degassing temperature (Allen, 1963). Over the years, several new processing approaches to make foams of a variety of metals and alloys have been developed (Banhart, 2001; Ashby et al., 2000; Hayden, 2002). Due to high specific strength, low processing temperatures, chemical and oxidation resistance, aluminum and its alloys find widest commercial and research interest among all metallic foams (Ashby et al., 2000). Literature reports are available for foaming of very low melting metals such as magnesium, zinc, tin and lead (Sugishita et al., 1982; Yamada et al., 1999; Yu et al., 1998; Wubben et al., 2003) as well as on high melting metals such as nickel, iron and titanium and ceramics (Kovacik, 1998; Li et al., 2000; Queheillalt et al., 2000; Bram et al., 2000; Queheillalt et al., 2001).

Metallic foams can be processed from the vapour, solid and liquid state of their base alloy. Generally, vapour and solid state methods are adapted for high-melting alloys whose melting point renders liquid-state methods impractical. However, powder compact method for foaming aluminum is an exception to the rule. Liquid-state methods are

largely used due to its simplicity and commercial viability. Liquid-state foaming, in the most general form, involves entrapment of gas bubbles during solidification. This gas is commonly introduced externally through pressurized nozzles, rotating impellers, or porous crucible surfaces (Thomas et al., 1997), but can also be generated within the melt itself through decomposition of suspended chemical additives such as metal hydrides (Kennedy and Lopez, 2003) or hydrated ceramic powders (Schroers et al., 2003). Certain alloys, such as nickel, copper, aluminum and magnesium are melted in hydrogen atmosphere under high pressure to obtain a homogeneous melt charged with hydrogen. Then the gas-filled pores along with the melt can be precipitated eutectically during solidification. Although several new foam processing methods are becoming known, the processing techniques based on (1) powder metallurgical route and (2) liquid melt route are most popular. These two processes are detailed below as the simplicity and feasibility of the process lends itself to large-scale manufacturing.

2.3.1. Powder Metallurgy Route

The powder compact method for fabricating net-shaped complex parts,

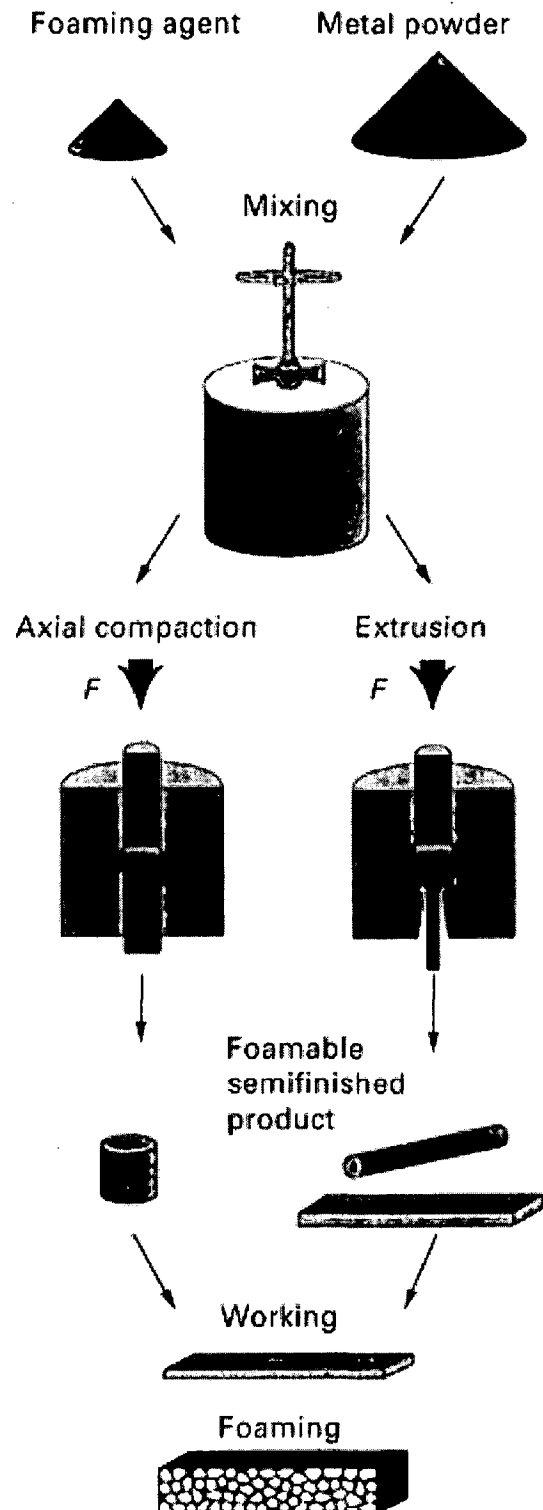


Fig. 2.3. Powder metallurgy route for foaming closed-cell foam (Banhart and Baumeister, 1998).

metal foam sandwich panels and foam filled hollow profiles are the major attraction in this method. It was invented at the Fraunhofer Institute for Applied Materials Research in Bremen, Germany and described schematically in Fig. 2.3 (Banhart and Baumeister, 1998). Aluminum or zinc alloys can be foamed by mixing the metals and the alloying elements in appropriate composition. The foaming agent TiH_2 or ZrH_2 are mixed in proper range according to the density requirement of the finished foam. Usually it is mixed in range from 0.4 to 1.0 wt.% of the base metal alloy. Both the powder are mixed well and compacted by extrusion for aluminum and by axial compaction for zinc. Homogenously mixed semi-finished part is obtained, which can be further processed to desired size and shape by rolling and cutting.

Foaming is done by heating the semi-finished parts to temperatures above the melting point of the matrix metal. The metal melts and the foaming agents decompose inside simple closed moulds to obtain the net-shape structures. The oxide layer present on the particle surface form a network structure which enhance the liquid foam stability (Kennedy and Asavavisithchai, 2004a; Korner et al., 2005). The addition of ceramic particles like Al_2O_3 , TiB_2 and SiC particles enhances the foam expansion through the reduction in cell wall thickness. But, non-wetting behaviour of the added particle occurs in the manner that the ceramic particles protrude from the cell walls and does not contribute to the prevention of drainage of liquid through the cell structure (Kennedy and Asavavisithchai, 2004 a&b). Therefore, wetting of the added particle is essential to retain the particles within the cell wall so as to reduce the drainage along the cell edges. To enhance the wetting behaviour, magnesium particles are mixed along with Al_2O_3 . They react and form MgAl_2O_4 , which ruptures the oxide film on the surface of the molten aluminum thereby increasing the wetting behaviour and improves the stability of the foam (Asavavisithchai and Kennedy, 2006).

The foaming behaviour of SiC -particulate (8 vol.%) aluminum composite powder compacted with TiH_2 is investigated by Elbir et al., (2003) who reported that the addition of SiC -particulate increases the linear expansion and reduces the extent of the liquid melt drainage and cell coarsening of aluminum compacts. The advantage of this technique is that complex-shaped metal foam parts can be manufactured by expanding the foam inside a mould, thus confining spatial expansion. Foam-filled aluminum sections and sandwich panels with aluminum foam core and metallically bonded steel, aluminum, or even

titanium face sheets are feasible. For making such composites the foamable precursor material is first bonded to the solid section or sheet by co-extrusion or roll-cladding, after which the foamable core layer is expanded by heat treatment (Seeliger, 2004). Powder-compact route have the advantage of foaming net-shape structures and foam-filling of the core of a solid part for achieving higher specific stiffness. The disadvantage of the process is the cost of metal powders and the size of parts, which is limited by the size of the baking furnace.

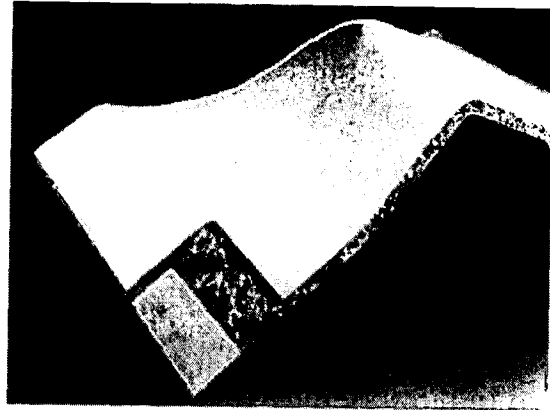


Fig. 2.4. Aluminum foam sandwich (AFS) sheet (Seelinger, 2004).

Aluminum foam sandwich (AFS) is sheet shaped structures comprising two layers of aluminum sheets and a core of aluminum foam in between (Fig. 2.4). They are made from pre-manufactured sandwich precursors and offer the structure a high degree of stiffness. The specialty of AFS is in unifying various functions such as light weight, thermal resistance, formability, energy absorption, sound insulation, etc., needed for automotive industries.

2.3.2. Liquid Melt Route

Liquid foams are usually in the metastable state such that the foaming occurs in the liquid until solidification. For the foam structure to be retained in the solid the life-time of the cell wall should be comparable to the time for solidification. For this reason, foam stability is an important parameter which is explained as the delayed rupture of cell walls and subsequent retardation in melt drainage (Babcsan et al., 2005). Stabilization mechanism of metallic foam is a rather complex phenomenon due to the simultaneous occurrence of solid, liquid and gaseous phases and their stochastic behaviour within the system. It is common practice to introduce a solid second phase either in-situ or ex-situ to enhance stability by increasing the melt viscosity (Haibel et al., 2006; Asavavisithchai and Kennedy, 2006; Banhart, 2006; Wubben and Odenbach, 2005). Moreover, the mechanical stability of the liquid foams produced with oxygen rich gas is higher than those using nitrogen as blowing agent (Leitlmeier et al., 2002).

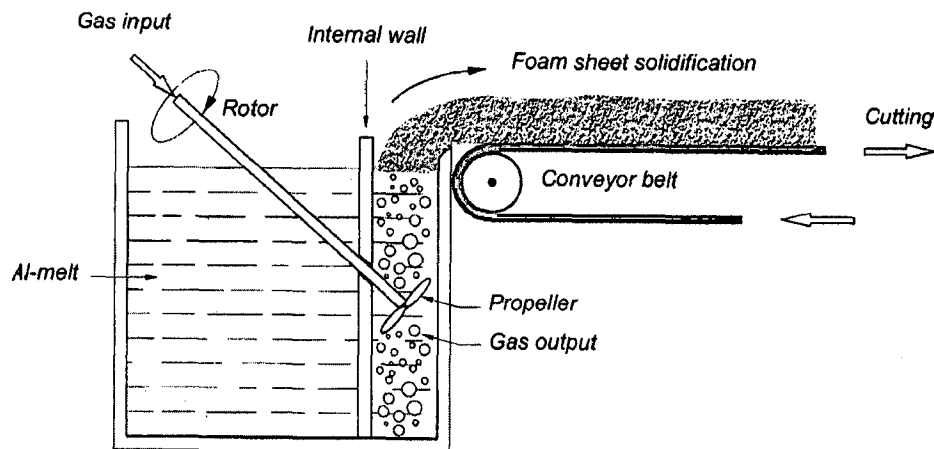


Fig. 2.5. Direct foaming of melts by gas injection in the manufacture of closed-cell foam (Asholt, 1999).

There are two ways the gas can be incorporated into the melt. The first method involves direct gas injection using a specially designed rotating impeller or vibrating nozzle. The second method employs addition of blowing agents in the liquid melt and the release of gas by decomposition (Banhart, 2001). These methods are explained below.

2.3.2.1. Direct Gas Injection

The schematic diagram of the direct gas injection foaming procedure is shown in Fig. 2.5 (Asholt, 1999). In the first step, 5 to 20 μm size silicon carbide, aluminum oxide or magnesium oxide is added in the range from 10 to 20 vol % to increase the melt viscosity (Woods, 1998). The problem of wetting has to be overcome to achieve uniform distribution of reinforcing particles in the melt. The liquid metal matrix composite is then foamed in the second stage by injecting gases (air, nitrogen or argon) into it using specially designed rotating impellers or vibrating nozzles. The function of the impellers or nozzles is to create very fine gas bubbles in the melt and distribute them uniformly. This is an important requirement because only if sufficiently fine bubbles are created, foam of satisfactory quality can be obtained. The resultant viscous mixture of bubbles and melt floats up to the surface of the liquid where it turns into fairly dry liquid foam as the liquid drains out. The foam is relatively stable owing to the presence of ceramic particle in the melt. It can also be pulled off the liquid surface, with a conveyor belt, and is then allowed to cool down and solidify. Care has to be taken not to damage the pore structure by shearing the foam too much while it is still semi-solid. Before solidification, the semi-solid foam can be flattened by means of one or more top-mounted rolls or belts to yield a

foam slab with closed and fairly even upper and lower skins. This method of foaming is currently being exploited by Hydro Aluminum in Norway and by Cymat Aluminum in Canada.

Aluminum foam are produced with density ranging from 0.069 to 0.54 g/cm³ having porosity between 80 and 98 %. The average pore size varies from 3 to 25 mm and wall thickness from 50 to 85 μm (Woods, 1998; Kenny, 1996). Deqing et al. (2005) have produced closed-cell aluminum foam using SiC particle as foam stabilizer and used compressed air for injection. It is reported that the cell size and distribution are uniform for high and low density foam without apparent defects.

Deqing et al. (2006) have studied the effect of process parameter on the cell structure. Aluminum foam of densities ranging from 0.1 to 0.22 g/cm³ are prepared with SiC as stabilizer with air injection. The air injection rate is varied from 0.5 to 2.0 l/min at a constant pressure with a rotation speed of impeller at 400, 600 and 800 rpm. It is reported that the cell size of aluminum foam increased with increase of air injection rate, whereas the impeller speed reduces the size of the cell with smaller cell size achieved at 800 rpm with thicker cell wall. The influences of process parameters such as particle material, matrix composition, foaming gas and temperature on cell morphology are studied. The foam stability is increased by using Al₂O₃ instead of SiC, which increases the cell wall thickness and lowers the surface tension effectively (Babcsan et al., 2003).

2.3.2.2. Foaming with Blowing Agents

Another method to foam liquid melt directly is by adding a blowing agent into the melt instead of injecting gas. The blowing agents decompose and releases gas, which is then trapped within the liquid melt to produce foam (Fiedler, 1965; Hardy and Peisker, 1967; Berry, 1972; Bjorksten and Rock, 1972). The aluminum foam produced in this method goes by the trade name "Alporas". Generally titanium hydride (TiH₂) is used as the blowing agent; alternatively, zirconium hydride (ZrH₂) may also be preferred (Niebylski et al., 1974).

After heating the master alloy to the molten state, calcium metal is added and stirred for several minutes, during which the melt viscosity continuously increases by a factor of up to five (Ma and Song, 1998). Fig. 2.6 shows the apparent viscosity increases with stirring time and the amount of calcium addition. It is to be noted that the melt

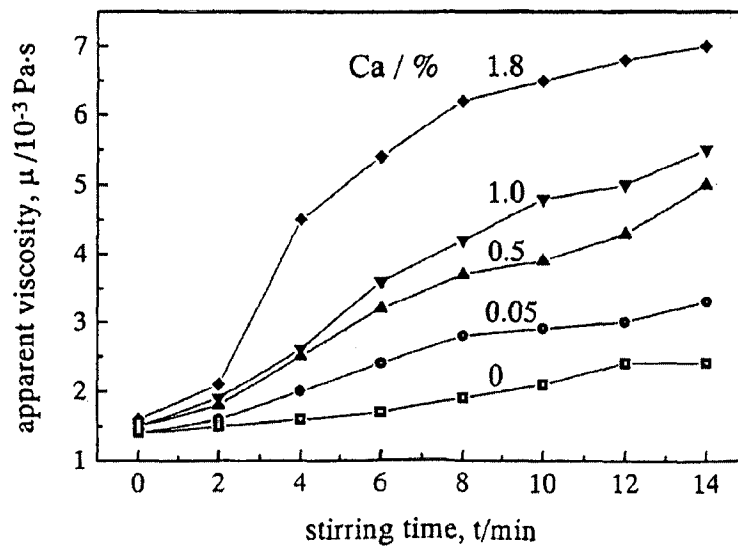


Fig. 2.6. Effect of the amount of calcium addition and stirring time on aluminum melt viscosity at 720°C (Ma and Song, 1998).

viscosity increases even when stirring the melt in atmosphere without calcium addition. This is because the vortex created by stirring destroys the oxide film of the melt and introduces the oxygen from air into the melt causing the oxidation of aluminum. The addition of calcium enhances this process as it reacts with oxygen removing the oxide film on the melt surface and promoting further oxidation of aluminum (Sreeja Kumari et al., 2005). It is to be noted that an enhanced apparent viscosity of melt is needed prior to the addition of blowing agent in order to achieve uniform cell structure during foaming. Too low a melt viscosity leads to the escape of gas bubbles and agglomeration of them in the upper part of the melt and too high a melt viscosity results in the difficulty of distributing TiH_2 uniformly and quickly throughout the melt before decomposition begins. Effective control of viscosity of melt and the rate of foaming is done by a two-stage foaming technique using natural minerals such as dolomite, calcite and magnesite, which are also inexpensive (Tzeng and Ma, 2006).

The viscosity of aluminum melt can also be enhanced by adding aluminum powders ($\sim 60 \mu m$ size) and stirred for 12-20 minutes at 600 rpm. The addition of aluminum powder and subsequent agitation in atmosphere facilitate oxidation of aluminum melt and generate fine oxide particles. Longer the stirring time, the greater the amount of Al_2O_3 formation (Yang and Nakae, 2003). Yang and Nakae, (2003) have also reported that the alumina particles not only increases the viscosity but also serves as the

nucleating agents for the bubbles to form higher porosity and a uniform pore structure. It may be noted that in the present work we have confined to increasing the melt viscosity by calcium addition alone before TiH_2 degassing.

2.4. The Physics of Foaming

Foam is defined as a dispersion of gas bubbles in a liquid or solid. Metallic foams are produced by dispersing a large number of gas bubbles into a metallic melt while in the liquid state and freezing the structure by solidification. Owing to the large surface energy necessary to create the metal-gas interface, foam is never in equilibrium and hence perpetually striving to lower the internal energy by reducing the internal surface. That is, the cellular structural state of foam evolves with time and its actual structure is a function of its history including all thermal and mechanical influences (Korner et al., 2002). In metallic foams the term stability is a misnomer as cellular structure is constantly evolving in the time scale of the foaming process. Cell wall rupture is a sporadic and spontaneous process due to the drainage of liquid melt induced by local pressure differences within the cell wall and by gravity. So, metal foam stability can be understood as a slowing down of the cell wall rupture and/or drainage process (Daniel and Edwin, 2007).

The foaming by liquid melt route using blowing agent is explained in section 2.3.2.2 and schematically shown in Fig. 2.7. This process is investigated in the present research work, where titanium hydride powder is used as a blowing agent and calcium

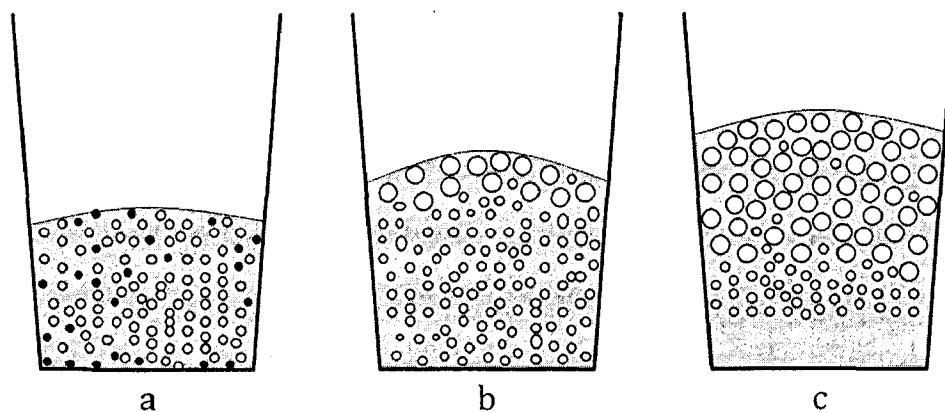


Fig. 2.7. The schematic showing the (a) nucleation, (b) growth and (c) migration of the gas bubbles to the surface of the melt.

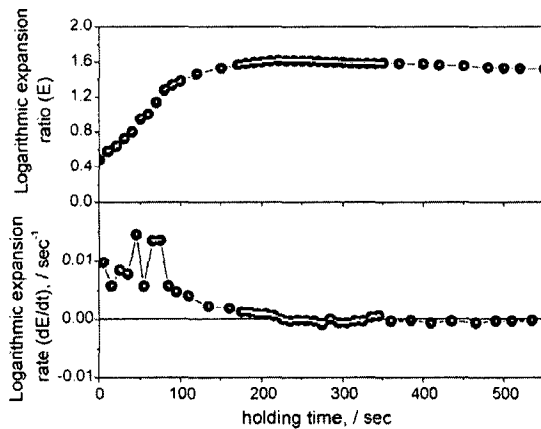


Fig. 2.8. Expansion ratio and rate of foam versus holding time in foam making process (Song and Nutt, 2007).

metal granules is used as a melt thickening agent. The evolution of foam structure is stochastic in nature. Furthermore, direct observations of the metal foaming process are difficult because foam expansion occurs at high temperatures. After the uniform dispersion of the degassing agent, the process of foaming begins with the formation of a tiny gas-liquid heterogeneous mixture by the decomposition of gas, which then grows

gradually. The liquid metal foam evolution occurs according to the following stages: (1) Creation of gas entrapped bubbles which rise to the surface to agglomerate together forming the foam. Each liquid foam cell consists of cell faces, edges and corners. The edge form the periphery of the cell face and edges meet at corners. (2) The second step involves the drainage of the liquid metal from the cell face to the thicker cell edge driven by the pressure difference. Additionally, drainage along the cell edge is driven by gravity which progressively makes the foam drier. (3) Finally, the collapse of the cell wall occurs which is spontaneous and random in nature. The stability of the foam is enhanced by controlling stages (2) and (3), i.e. hindering drainage and delaying cell wall collapse.

Song and Nutt (2007) have noted that the expansion ratio increases rapidly at the onset of the foaming process, but after sufficient time, the expansion and collapse rates reach a dynamic balance, and the foam stabilizes. The relation between expansion ratio and expansion rate of the foam with the holding time is shown in Fig. 2.8. Once sufficient expansion of bubble has occurred, then thinning down of the cell membrane and drainage from the wet foam tends to weaken the structure with time. Small perturbation, decomposition of blowing agent, pore evolution, pore rupture, pore coalescence and/or thermal fluctuation can lead to significant structural changes and even total collapse. For this reason, foaming experiments are not always reproducible and sometimes structures of aluminum foam fabricated under the 'same' conditions can be quite different. It is also reported by them that the evolution of gas from the blowing agent supports the

development of foam structure within the melt and helps prevent collapse. Therefore, it is recommended that solidification process should be completed before the blowing agent is exhausted (Weaire and Hutzler, 1999).

The final pore size of the foam is decided by the stirring process, the blowing agent powder size and coalescence and/or rupturing of pores during holding and solidification stages. Initially, titanium hydride decomposes very quickly and slows down to such a stage where the amount of hydrogen release per unit time gradually decreases in the course of time. The driving force for bubble growth comes from the hydrogen release, which increases the pressure inside the cell. The resistance to this growth is the sum of the hydrostatic pressure of the melt along with the pressure due to curved surface caused by surface tension and the atmospheric pressure (Yang et al., 2007).

If the driving force and the opposing force are in equilibrium, then the force balance is given as

$$P_{in} = \frac{2\sigma}{r} + P_{st} + P_o \quad (2.1)$$

where P_{in} is the inner pressure of a bubble, σ the surface tension of the melt, r the radius of a bubble, P_{st} the static pressure of the melt onto the bubble and P_o is the atmospheric pressure. At the same time, the gas in a bubble during its expansion follows the ideal gas law given as

$$P_{in}V_b = nRT \quad (2.2)$$

where n is the number of moles of gas in the bubble, R the gas constant, T the absolute temperature, and V_b is the volume of the bubble. Substituting equation (2.2) in equation (2.1) and letting $V_b = 4/3\pi r^3$, and differentiating both sides with respect to time t , the following equation is obtained

$$4\pi r \left[\frac{4}{3}\sigma + r(P_{st} + P_o) \right] \frac{dr}{dt} = RT \frac{dn}{dt} \quad (2.3)$$

where dn/dt is the decomposition rate of titanium hydride. The value of decomposition rate of TiH_2 mainly depends on the temperature, activation energy and pre-exponential

factor, while dr/dt which is the bubble growth rate depends mainly on the pressure inside the bubble. Under certain condition, if σ , P_{st} and P_o can be regarded as constant, and then the rate of bubble growth is directly related to the decomposition rate of TiH_2 . So the decomposition rate of TiH_2 directly determines the porosity increase (or density decrease) rate of the aluminum alloy foam.

The foaming behaviour in the melt system and the decomposition characteristics of the blowing agent have to be coordinated. The decomposition of TiH_2 starts at 400 °C for untreated hydride and can be delayed by preheat treatment (Matijasevic and Banhart, 2006; Kennedy, 2002; Yang and Nakae, 2000). Yang et al. (2007) have reported that the porosity of the aluminum alloy remains fairly constant during the stirring period of 30-80 s after TiH_2 addition. It is observed that during stirring, the pore number increases and pore diameter decreases due to the creation of additional cell walls with time. The excess hydrogen gas released during this period is lost to the atmosphere. However, Song and Nutt (2007) have reported that the original size of the pore is determined by the stirring process and the expansion rate is determined by the size of the blowing agent powder.

Spherical foams are much more stable in comparison to polyhedral foams. It is important to understand the actual processes that lead to bubble rupture and the factors which contribute to the stability of foams. The stability and structure of foam are determined primarily by the rate of coalescence of the dispersed gas bubbles. The process of coalescence in foam is controlled by the liquid drainage (a process of thinning) and rupture of the films which separate the gas bubbles. Experimental observations suggest that the lifetime (stability) of films is determined primarily by the thinning time rather than by the rupture time. Wang (1995) has noted that if the approaching bubbles have equal size, the process of coalescence can be split into three stages: (a) formation of a thick film, (b) thinning of the film and (c) rupture.

The viscosity of the melt and the intermetallic particles present in the cell walls will oppose the drainage of liquid along the cell edge, whereas the force of gravity and capillary pressure induce the same. Shortly after foaming agent powder is dispersed into the melt, the nucleus of bubble forms around the TiH_2 particle. Since, the melt is vigorously stirred in this stage, which keeps the bubble size fairly uniform and small. Once the stirring is stopped, the bubble continues to grow with the decomposition of

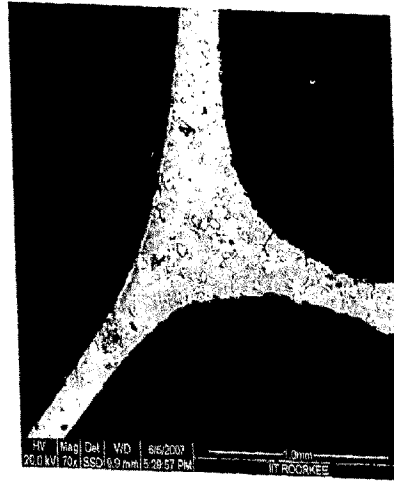


Fig. 2.9. SEM image of the closed-cell aluminum foam cell wall showing large convex curvature from the cell wall to the cell edge.

TiH₂. Then, simultaneously, the drainage of liquid will start and bubbles shape will change from spherical to planar film with separate polyhedral shaped bubbles. The polyhedral bubble is called cell and two adjoining cells share a wall or cell face and three adjoining cells share a curved triangular prismatic rod called plateau border or cell edge.

The gas-liquid interface has a large convex curvature as shown by the microstructure of the cell wall (see Fig. 2.9). This curvature generates a large negative pressure in the plateau border area and can be estimated by the Young-Laplace equation,

$$\Delta P = \sigma \left[\frac{1}{R_1} + \frac{1}{R_2} \right] \quad (2.4)$$

where ΔP is the capillary pressure, which is the pressure difference across a curved surface, σ is the surface tension, R_1 and R_2 are the two principle radii of the curvature at the edge and the cell face, respectively. Since the interface is only slightly convex along the thin-film region, a lower negative pressure resides there. This pressure difference forces the flow toward the plateau borders and accelerates the thinning of films. This thinning process will lead to film rupture and coalescence. From the equation 2.4, the ΔP can be reduced either by decreasing the surface tension σ , or by modifying the curvature of the plateau border.

Viscosity is a measure of resistance of a fluid to flow. It is a common practice to introduce a solid second phase either in-situ or ex-situ to enhance stability by increasing the apparent melt viscosity (Haibel et al., 2006; Asavavisithchai and Kennedy, 2006; Banhart, 2006; Wuben and Odenbach, 2005). Control of melt viscosity is very important in obtaining uniform cell structure. A low viscosity will lead to rapid rise of the bubbles and faster bubble growth making the cell wall thin leading to coalescence of cells. If the viscosity is too high, it would be difficult to disperse uniformly the foaming agent in the melt, which is a necessary pre-condition for obtaining uniform cell structure (Ma and Song, 1998; Song et al., 2000; Yang and Nakae, 2003).

Leitlmeier (2002) and his co-workers have studied the influence of particle on the stability aspect by gas injection melt route and concluded that foam stability depends on the interaction between the blowing gas, the ceramic particle and the melt. The effect of the particle can be characterized by their reaction with the melt, their wetting behaviour and their size, shape and distribution in the melt. In ex-situ addition, Al_2O_3 particles are not readily wetted by liquid aluminum and the addition of highly reactive elements, such as magnesium improves the wettability (Asavavisithchai and Kennedy, 2006). The addition of magnesium changes the way in which the Al_2O_3 particles reside on the cell wall surface by completely spreading the aluminum melt over the particle. They are more effective at trapping liquid, thereby decreasing the extent of drainage of liquid through the structure and improve the stability of the foam (Babcsan et al., 2004).

2.5. Properties of Foam

The properties of foam are closely associated with the material property of which the cellular structure is made. However, for a particular material, the relative density or the porosity of the foam is the major parameter which characterizes the foam properties. The two types of foam: open-cell and closed-cell foam exhibit contrasting thermal properties. The increased surface area and flow properties of open-cell foams enhance heat transfer. The cell size, shape, aspect ratio, size distribution and cell defects are the other major parameters which influence the properties of the foam (Yu et al., 2007; Bin et al., 2007; Cao et al., 2006; Edwin and Daniel, 2007b). Table 2.1 contains the important properties of closed-cell foam processed by different methods (Ashby et al., 2000). The

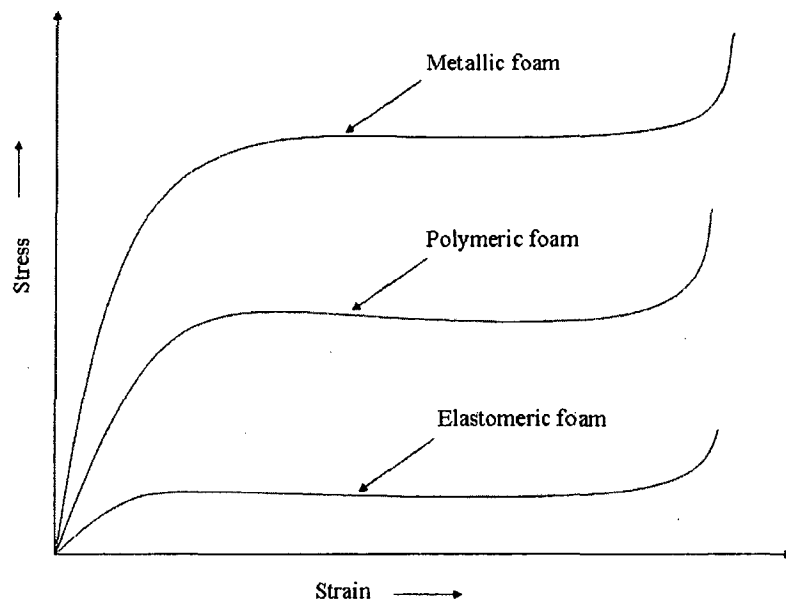


Fig. 2.10. Schematic sketch of the compression stress-strain diagram of Elastomeric, Polymeric and Metallic foams.

processing technique used in the present work goes by the commercial name – Alporas. From the data given by Ashby et al. in 2000, the properties of Alporas foam is updated with the results obtained in the present work. Significantly, a wider range of relative density of foam was obtained which corresponded to a wider range of mechanical properties as well.

Polymeric foams are quite common in usage, but the major disadvantage is its limited strength and the lower range of operating temperature. Polymers can be classified as thermoplastic, thermosets and elastomers. Thermoplastics solidify into an amorphous structure having density near to 1 g/cm^3 . Thermoplastic polymers with heavier atoms, like oxygen or fluorine can be denser, close to 2.2 g/cm^3 . However, the cross-linked thermoset polymers are having strong C-C primary bond. Their densities are usually higher than most common thermoplastic polymers with densities in the range of 1.2 to 1.5 g/cm^3 . Elastomers or rubber are structurally linear-chain polymers with a few widely spaced cross-links. The glass transition temperatures of this class of polymers are usually below room temperature; so the molecules can slide relative to each other easily.

The glass transition temperature of the material decides the temperature at which the solid or rigid material transforms to rubber or viscous liquid. Most commercial

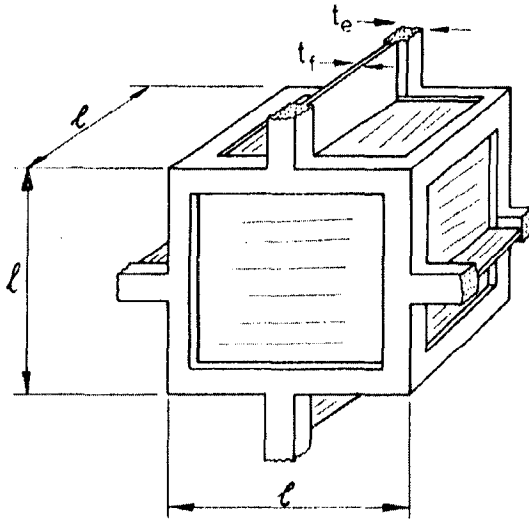


Fig. 2.11. Gibson and Ashby model for closed-cell foam (Gibson and Ashby, 1997).

polymers have a glass transition temperature in the range of 0 – 100 °C. If the molecular weight and cross-linking of the polymers are high then its glass transition temperature will be higher. This temperature dictates the operating temperature of the polymeric foam. Moreover, polymers are poor resistant to fire due to the presence of hydrocarbons. On the other hand, metals have strong metallic bond giving high melting points and the Young's modulus is much higher than the polymers. The schematic sketch of the stress-strain curve during

compression of elastomers, polymers and metals foams are compared in Fig. 2.10.

The elastomeric foams, like cushion are used to protect small things from very small force and for comfort in seating. Polymeric foams can take more force than elastomeric foam and also can absorb more energy in compression, but due to the low transition temperature they cannot be operated at much higher temperature. Whereas, the metallic foams offer higher energy absorption capacity and higher stress intensity can be accommodated. They can also be operated at much higher temperature without any difficulties. The high compression strength along with large compressive strain of metallic foams finds application for energy absorption in automobiles, railways, packing industries, and for blast/impact protection. Their low specific weight and higher specific strength and modulus attract application for light weight structures.

The properties of foam are related to the structural features like density, pore diameter, pore size distribution, cell aspect ratio, etc and to the properties of the cell wall material properties such as density, ρ_s , the Young's modulus, E_s , and the yield strength, σ_{ys} . Metallic foams also demonstrate certain unique non-structural properties that are not easily obtained in other materials such as acoustic and vibration damping, controllable thermal and electric conductivity (Ashby et al., 2000, Simancik and Kovacik., 2002).

Table 2.1. Some properties of different types of closed-cell foam.

Property	Cymat foam	Alulight foam	Alporas foam
Material	Al-SiC	Al	Al
Relative density	0.02-0.2	0.1-0.35	0.06-0.4
Young's modulus (GPa)	0.02-2.0	1.7-12	0.4-4.14
Shear modulus (GPa)	0.0001-1.0	0.6-5.2	0.3-0.35
Bulk modulus (GPa)	0.02-3.2	1.8-13.0	0.9-1.2
Flexural modulus (GPa)	0.03-3.3	1.7-12.0	0.9-1.2
Poisson's ratio	0.31-0.34	0.31-0.34	0.31-0.34
Compression Strength (MPa)	0.04-7.0	1.9-14.0	0.8-38.5
Tensile elastic limit (MPa)	0.04-7.0	2.0-20.0	1.6-1.8
Tensile strength (MPa)	0.05-8.5	2.2-30.0	1.6-1.9
Densification strain	0.6-0.9	0.4-0.8	0.7-0.82
Energy absorption capacity (MJm ⁻³)			2.4-6.4
Fracture toughness (MPa.m ^{1/2})	0.03-0.5	0.3-1.6	0.1-0.9
Thermal conductivity(W/mK)	0.3-10.0	3.0-35.0	3.5-4.5

These properties are not considered here in depth though it is important to the broader field of application of metallic foams.

The relationships between the properties and relative densities of foams are always empirically determined; however many relationships are predictable using simple model representations of foam structure. The most common, and most simple, of these structure is called the Gibson-Ashby model which is derived on the basis of regular cell structure (Fig. 2.11). A special constant, ϕ , the 'distribution constant', is introduced in the analytical relationship which is the fraction of solid in the foam contained in the cell edges. Also the determination of cell wall mechanical properties is quite complex owing to the presence of stabilizing particles in the cell wall. The accuracy of Gibson and Ashby

model prediction mainly depends on these values and relative density of foam (Gibson and Ashby, 1997). However, the influence of pore size on the mechanical properties is reported recently, which are not considered in Gibson and Ashby model (Yu et al., 2007; Bin et al., 2007; Cao et al., 2006; Edwin and Daniel, 2007b).

2.5.1. Mechanical Property

The comparison of stress-strain curve of metallic foam and solid metal in tension and compression is shown in Fig. 2.12. The compression behaviour of metallic foam is quite different in comparison with solid metal. Moreover, the collapse behaviour under compressive load is different for the open-cell and closed-cell foam. The open-cell foam deforms initially by bending followed by the formation of plastic hinges within the cell walls at higher strains. On the other hand, the deformation mechanism of the closed-cell foam is by the bending of the cell edges accompanied by stretching of the cell faces (Gibson and Ashby, 1997). Compression behaviour of metal foam is of singular interest and there are several recent publications in the literature (Han et al., 2004; Kim et al., 2005; Yu et al., 2007; Doyoyo and Mohr, 2006; Bin et al., 2007). Fig. 2.13 shows the compression properties that can be determined from the stress-strain curve. Three regions can be identified in the compression stress-strain curve, namely, the initial linear elastic region followed by an extended plateau region and the final densification region. In the

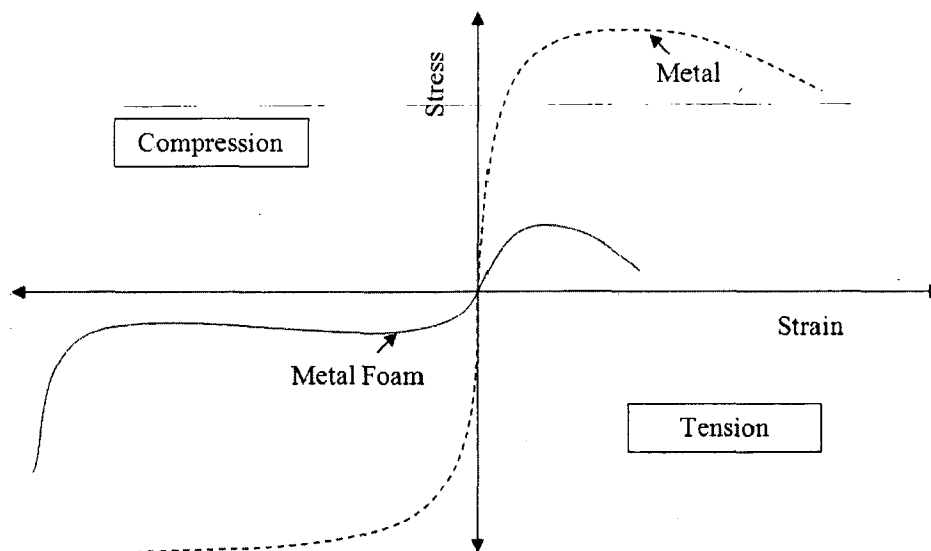


Fig. 2.12. Schematic stress-strain diagram of metal and its foam in compression and tension.

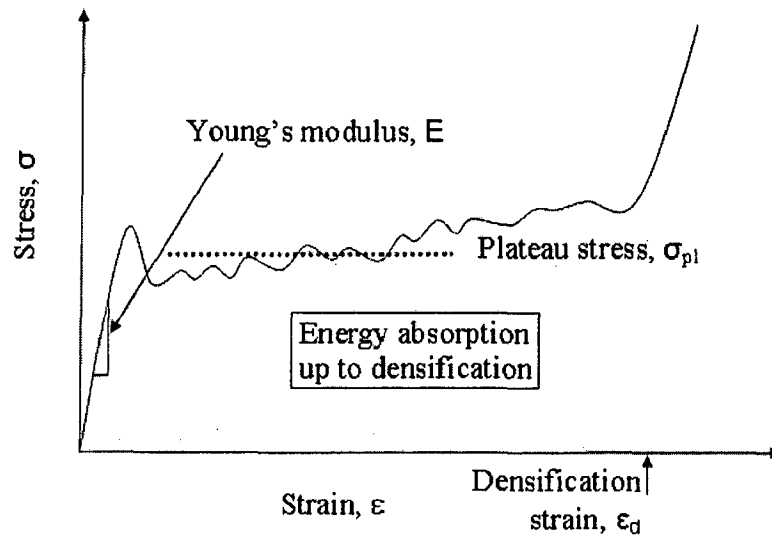


Fig. 2.13. Schematic representation of compressive property determination of foam from the stress-strain curve plot of compression test.

initial recoverable linear region Hooke's law is valid. The extended plateau stress in compression is unique to foam applications where the stress remains constant and the foam collapse layer by layer. The Young's modulus and plateau stress of foam are lower than that of the fully dense material, but the specific properties are significantly higher. The densification region is characterised by the dramatic build-up of stress for incremental strain signifying complete collapse of the foam into a dense material.

2.5.1.1. Compression Modulus

The initial linear elastic region in compression is characterized by the cell wall bending in open-cell foam, whereas in closed-cell foam this is also accompanied by cell face stretching along with influence of gas pressure of the cell. In this region, the relation between stress and strain being proportional, the Young's modulus of the foam is calculated. The simplified versions of Gibson and Ashby model proposed for predicting the elastic modulus E^* of cellular materials is given by their relation to the relative density as:

$$\frac{E^*}{E_s} = \alpha_1 \left(\frac{\rho^*}{\rho_s} \right)^n \quad (2.5)$$

where E_s is the Young's modulus of the solid cell wall material. The predicted values for most metal foam: the materials constant n lies between 1.5 and 2.0, α_1 between 0.1 and 4 depending on the structure of the foam (Lu and Ong, 2001). The more elaborate analytical treatment of the Young's modulus of the closed-cell foam modelled with regular cell structure by Gibson and Ashby is given by the relation,

$$\frac{E^*}{E_s} = \phi^2 \left(\frac{\rho^*}{\rho_s} \right)^2 + (1-\phi) \left(\frac{\rho^*}{\rho_s} \right) + p_o(1-2\nu^*) \left(E_s \left(1 - \frac{\rho^*}{\rho_s} \right) \right) \quad (2.6)$$

where, ϕ is the fraction of solid contained in the cell edges and ν^* is the Poisson ratio and the term $p_o(1-2\nu^*)/E_s \left(1 - \frac{\rho^*}{\rho_s} \right)$ is considered to be negligible, which represents the resistance of the air trapped in the closed-cell.

Increase in modulus values is observed when the height of the specimen was increased and also the loading modulus is $\sim 50\%$ smaller than that extracted from the unloading data (Sugimura, 1997; Ramamurty and Paul, 2004). The reduction in stiffness is also observed when the ratio of the specimen size to the cell size is small (Tekoglu and Onck, 2005). Ramamurty and Paul (2004) have tested Alporas aluminum foam with relative density of ~ 0.1 and reported that the unloading modulus value is in the range of 0.382 to 1.17 GPa for various height specimens. This is comparable to the values of modulus reported in other literature (Simone and Gibson, 1998; Andrews et al., 1999). Olurin et al. (2000) have tested Alporas foam with relative density in range 0.08-1.15 and reported to have modulus in the range 0.22-0.78 GPa. Kim et al. (2005) have measured the compressive mechanical properties of foam by non-destructive testing through electrical conductivity measurements. They have tested foams having relative density in the range 0.09 to 0.25 and found that the Young's modulus falls in the range from 0.69 to 4.14 GPa.

2.5.1.2. Compression Plateau Stress

The elastic region is followed by the plateau region in the stress-strain curve. The plateau region can be further differentiated into two regions as, the initial collapse stage and successive collapse stage. The initial collapse stage is marked by the sudden collapse after the first peak stress. In the successive collapse stage, the stress-strain curve is

characterized by serration, but the stress level remains fairly constant. The average stress at this region is called plateau stress, σ_{pl}^* . Olurin et al. (2000) have taken the average compressive stress for compressive nominal strains within the range 5-30% as plateau stress. They have tested Alporas foam in relative density range 0.08-0.15 and found the plateau stress to fall in the range 1.39-2.46 MPa. Due to structural variation with the given foam, the cell buckling, yielding, fracture and the compaction of cell layer occurs from the weakest region and proceeds to the next weaker layer. This successive layer by layer collapse of the cells is the reason for the serration in the stress-strain curve. The actual stress-strain behaviour varies from foam to foam depending on the fabrication methods, presence of the amount and type of particles in the cell wall material, etc. They may also differ from specimen to specimen taken from the same foam due to the non-reproducible nature of the foam structure (Song and Nutt, 2007).

When all the cell walls have completely collapsed, the cell walls touch each other and subsequently a little increment in strain can raise the stress level appreciably. This region at the end of the plateau region is also known as the densification region. The strain associated with the commencement of this region is called densification strain, ϵ_d (Gibson and Ashby, 1997; Ashby et al., 2000).

2.5.1.3. Tensile Property

The mechanical properties of foams in tension are rarely of interest in comparison with compression. This is because the pores within foam materials tend to act like cracks in tension and even ductile material foams show poor ductility in tension (Fusheng and Zhengang, 1999). Andrews et al. (1999) have tested aluminum foam under tension and found the ductility as 0.17%, and also reported that the tensile strength is half its compressive strength. For this reason, tensile loading of foams is almost entirely avoided (Ashby et al., 2000). Nonetheless, local tensile loading always occurs on one face of a component subjected to bending, which is an important deformation mode for many foam applications. The poor properties of foams in tension are usually mitigated by incorporating them as sandwich or filled structures, in which the foam layer is bonded between solid metals. These face sheets play several roles, including providing substrates for bonding and joining operations, prevention of fluid flow through the foam, confinement/strengthening of the foam surfaces and provide good surface finish. Also,

foams if sandwiched between two solid face sheets still provide high specific strength (Schwingel et al., 2007; Demsetz and Gibson, 1987; Contorno et al., 2006). These added benefits often lead to substantial improvements in foam properties with only a small increase in overall material density (McCormack et al., 2001) and are therefore extremely important for the future development of foam applications.

2.5.1.4. Energy Absorption Capacity

Metallic foams attract engineering application as energy absorber due to the large compressive strains at nominally constant stress levels up to densification. This phenomenon is the ability of the material to absorb large energy at force levels commensurate with crash and blast protection systems (Nasser et al., 2007; Ramachandra et al., 2003; Sriram, 2006; Miyoshi et al., 1999; Greene et al., 2002). The material selection for energy absorption is based on the energy absorption capacity per unit volume or mass and the plateau stress at which the energy is to be absorbed (Evans et al., 1999). Light weight and safety requirements have set demands for light-weight materials and structures with high specific energy absorption capacity for the transport industry

(Song et al., 2005). The advantage of metal foam over its polymer counterpart is the comparatively higher specific energy absorption capacity, high temperature resistance and non-flammability.

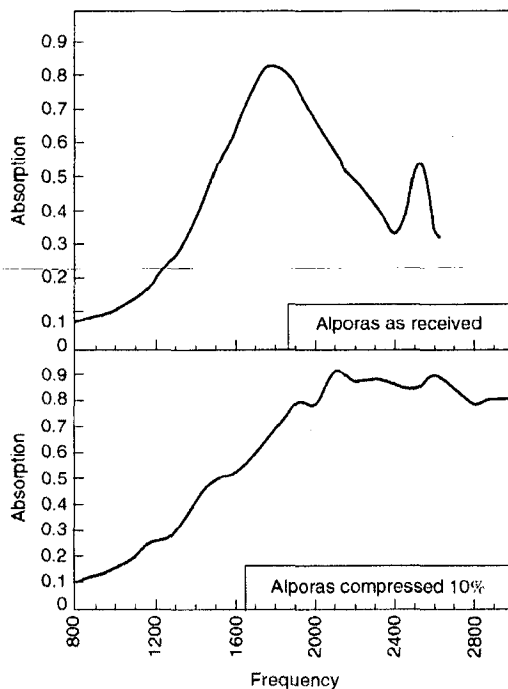


Fig. 2.14. Sound absorption measured in a plane-wave impedance tube for Alporas foam (Ashby et al., 2000).

Good energy absorbers are the ones exhibiting large strains at a relatively low constant stress levels. The need for protective packing is to keep the peak force on the packaged object below the threshold which will cause damage or injury. The occurrence of damage to the structure involved is governed by the allowable stress levels the structure can withstand during impact. To avoid

damage to those structures, the impact stress levels should not exceed the plateau stress of foam. By choosing the right cell wall material and relative density, the foam can be tailored to give the best combination of properties for the given application (Gibson and Ashby, 1997).

When foam is compressed or loaded, work is done on the foam. The work done per unit volume, W in deforming the foam to a strain of ε is calculated as the area under the stress-strain curve up to the strain, ε (see Fig. 2.14).

$$W = \int_0^{\varepsilon} \sigma(\varepsilon) d\varepsilon \quad (2.5)$$

Markaki and Clyne (2001) have estimated the energy absorption capacity of the aluminum foam up to densification for the relative density range of 0.14-0.23 as 2.4-6.4 MJ/m³. The level of plateau stress depends on the cell wall material, relative density and the strain rate. Several mechanisms are involved in absorbing energy, such as elastic, plastic or brittle deformation of the cell walls and faces, the compression and flow of fluid within the cells, etc. The operating mechanisms vastly differ for open-cell and closed-cell foam. In open-cell foam the energy is absorbed by the elastic buckling, plastic yielding or brittle crushing of the cell edges. However, in closed-cell foams, along with the above, bending, buckling and stretching of cell walls along with compression and flow of fluid within the cells will contribute in energy absorption. Sometimes, a higher plateau stress is reported at higher strain rate, which is useful when foam is intended for energy absorption at higher velocity impact. Higher energy absorption capacity at high strain rate is a very desirable property while using foam for light weight impact energy absorption applications.

2.5.1.5. Strain Rate Dependency

Metallic foams have the potential for absorbing impact energy during the crushing of a vehicle during accident, or for absorbing impact energy by serving as blast protection shield. To evaluate the impact energy absorbing capacity of aluminum foam, the relationship between the compressive stress and strain at a dynamic strain rate has to be established. The stress-strain behaviour at dynamic strain rate is often characterized by using split Hopkinson pressure bar (SHPB) method. Kolshy (1949) developed the split

Hopkinson's pressure bar way back in 1949 to determine the dynamic properties and later on, modification are made on the device to test metals, concrete and ceramics (Follansbee, 1985; Ross, 1996; Chen and Ravichandran, 1997). Conflicting results are reported in literature on the strain rate sensitivity of aluminum foam. Insensitivity of the compressive properties to strain rate variation is reported by many for both closed-cell and open-cell foams. Deshpande and Fleck (2000b) has studied Alulight-closed-cell foam and Duocel-open-cell foam and reported to be insensitive to strain rates up to 5000 s^{-1} . Similar result is also reported by Ruan et al. (2002) on CYMAT-closed-cell foam tested in the range from 10^{-3} to 10^1 s^{-1} . But on the other hand strain rate sensitivity on CYMAT-closed-cell foam is reported by Montanini (2005) when tested up to a strain rate of 10^2 s^{-1} . Kanahashi et al. (2000) have investigated on open-cell aluminum and magnesium foam fabricated by casting technique and Alporas-closed-cell foam at a dynamic strain rate and reported approximately 60% increase in compressive properties at strain rates of $1.4 \times 10^3 \text{ s}^{-1}$. Yi (2001) and his co-workers have reported that open-cell aluminum foam fabricated by powder metallurgy route has shown strain rate sensitivity for relative densities over a range from 0.15 to 0.29. In general, most of the studies on closed-cell aluminum foam made by using blowing agents through liquid melt route (Alporas) have shown strain rate sensitivity (Mukai et al., 2006; Mukai et al., 1999; Dannemann and Lankford, 2000; Ramachandra et al., 2003; Paul and Ramamurty, 2000).

2.5.2. Sound Absorption and Vibration Damping Property

Sound is caused by vibration in an elastic medium. The speed of longitudinal vibrations v in a given medium is given by:

$$v = \sqrt{E/\rho}$$

where E is the modulus of elasticity and ρ is the density of the medium. For example, the velocity of sound in air is only 343m/s, whereas in solid steel or aluminum is $\sim 5000\text{m/s}$. When a plane sound wave impinges normally on an acoustic absorber, some energy is absorbed and some is reflected back. If absorption is measured using a plane-wave impedance tube, the pressure p_i in the incident wave is described by

$$p_i = A \cos(2\pi ft) \tag{2.6}$$

and that in the reflected wave p_r is given by

$$p_r = B \cos\left(2\pi f\left(t - \frac{2x}{v}\right)\right) \quad (2.7)$$

Then the total sound pressure in the tube is the sum of incident and reflected pressure, where f is the frequency in Hz, t is the time in s, x is the distance from the sample surface in m, and A and B are the amplitudes.

The absorption coefficient α is defined as

$$\alpha = 1 - \left(\frac{B}{A}\right)^2 \quad (2.8)$$

Sound absorption capacity is smaller at low frequency compared to high frequency in Alporas foam (Ashy et al., 2000) (see Fig. 2.14) as well as in sandwich panels (Yu et al., 2006). The sound reduction increases with increase in thickness and porosity. As seen in Fig. 2.14, induced porosity by rupturing the cell faces increases the sound absorption capacity of aluminum foam.

Vibration damping capacity of a material is nothing but the ability to absorb or convert the vibrational energy into internal friction as heat and subsequently dissipating it to the surroundings. The rate of vibration damping is characterized by the loss factor, η . The cellular materials exhibit at least one order of magnitude higher values than typical structural materials like steel, aluminum, etc. The dissipation of energy takes place in foam by means of the vibration in thin cell walls and due to the occurrence of cracks in the structure. Damping is strongest in foams with the lowest densities than the one with higher density (Jiejun et al., 2003).

2.5.3. Electrical and Thermal Property

The electrical conductivity of the metal foam is less than the parent metal in which it is made owing to the porosity in its structure. The reduced conductivity of metal foams is enough to provide good electrical grounding and shielding of electromagnetic radiation (Simancik and Kovacik, 2002). Open-cell nickel foams are used as electrodes successfully for batteries in hybrid electric vehicle due to the large surface area (Paserin, 2004). The relationship of electrical conductivity with relative density is non-linear and

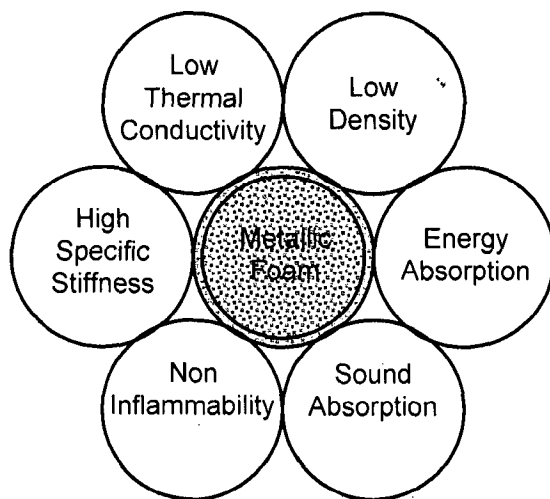


Fig. 2.15. Multifunctionality of Metallic Foams.

increases rapidly once the relative density is above 0.5. Due to the oxide surface skin on the cell walls, closed-cell metal foams can be successfully used for the protection of electronic devices and humans from the effect of electromagnetic noise. They also exhibit better magnetic field shielding.

The melting point of metal foams is a little higher compared with the parent metals, due to the presence of oxide layer on the cell wall surfaces. Most of the

other thermal properties such as specific heat, coefficient of thermal expansion, thermal conductivity, etc. remains the same as that of the alloy from which it is made. The thermal conductivity of closed-cell metal foam is lower than the base metal due to the presence of gas inside the cell, but that reduction is not sufficient to be considered as an insulating medium. However, due to the combination of fire protection capacity, they can be used as thermal insulator in certain applications.

Another important use of open-cell foams is its ability to serve as heat exchangers. They provide more surface area for heat exchange and also create turbulent flow through them with low-pressure drop, which allows more residual time of the fluid within the foam, improving the efficiency of heat transfer. The compatibility of the material for this purpose attracts application in power electronics and compact heat sinks (Ashby et al., 2000).

2.6. Applications

The combination of physical and mechanical properties, such as high stiffness in conjunction with very low specific weight and high compression strengths (that is, higher than polymer or rubber foam) combined with good energy absorption characteristics make these materials useful for several engineering applications (Edwin and Daniel, 2007a). The combination of special properties which are not brought together in

conventional material finds specialized applications for foams as shown in Fig. 2.15. Additionally, these materials are fully recyclable without any waste management issues. The ability of foams to plastically absorb extreme amount of energy while minimizing transfer of stress makes them one of the efficient material for packing and impact / blast protection applications. Open-cell foam finds additional application as efficient heat exchanger and as an electrode material for batteries. Large internal surface area enhances heat transfer through the flowing fluid in heat exchangers and provides large substrate areas for catalysis or electrode applications.

In general, the usage of foam can be classified into structural and functional applications (Banhart, 2001). The main advantage as a structural material is its low weight and high specific stiffness. Moreover, the crash / impact energy absorption ability is a unique property, which is finding many important engineering applications. The properties of aluminum foams are very attractive for automotive industry (Fig. 2.15). Automotive industry requires components which are light in weight, ability to absorb energy in crash situation and damping capability (Baumeister et al., 1997).

Aluminum foam sandwiches (AFS) are finding potential application in car industry (Banhart, 2005) and space application (Schwingel, 2007) due to high stiffness, low weight and good surface finish (see Fig. 2.4). The foam filled solid structures are increasingly used for crash energy absorption and also to improve the stiffness of hollow parts as shown in Fig. 2.16. A remarkable reduction in weight by one-tenth of their mass density can be achieved by foaming.

Beams and sheets made of foamed metals have high specific stiffness values due to favourable thickness to weight ratio (Degischer, 1997). Aerospace, ship buildings, railway, sporting equipment are other areas in which foams are increasingly used. Biomedical industry is another area where the porous layer of foam can ensure the in-growth of tissue for titanium or cobalt-chromium alloys.

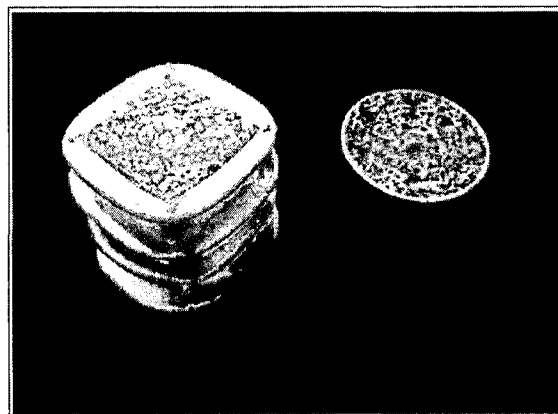


Fig. 2.16. Foam filled aluminum structure for crash energy absorption (Banhart, 2005).

Regarding functional applications of foam, the major breakthrough is in the area of open-cell foam for heat exchanger design, filtration devices and electrodes for batteries. Applications of compact heat sinks for cooling of microelectronic devices are gaining importance owing to the open porosity with less pressure drop. Details about heat exchanger design using metal foam are given in Evans et al. (1999). Fire arresting capability, silencer design, acoustic control, decoration and arts are other areas where foams have the potential as a functional material.

2.7. Modelling

The modelling and simulation of metallic foam is necessary to predict the property of the material, in order to assist in the design of metallic foam components. On the processing aspect, the design of process variable to control the structural parameter of the solid foam is a great challenge (Matijasevic and Banhart, 2006). However, considerable number of modelling studies is aimed at correlating the structural parameter to the mechanical properties of metallic foam. The continuum-based approach employs continuum mechanics to characterize the foam. On the other hand, most of the modelling effort is by unit-cell based approach, which relies on discretizing the foam structure into periodic self-repeating cells. Microscale geometrical imperfections, which are common in metallic foams, can also be introduced in a controlled way to assess the material response in these models.

Continuum-based models provide means for simplified treatment of foam materials through evaluating average field variables over the domain (Gibson and Ashby, 1997; Miller, 2000; Deshpande and Fleck, 2000a; Chen and Lu, 2000). They are characterized by their dependence on the hydrostatic component of the stress tensor due to the existence of plastic compressibility of the gas filled pores. Hansen et al. (2000) and Onck (2001) have investigated the accuracy of different continuum-based foam material models using LS-DYNA and ABAQUS explicit finite element solvers. The models were validated against the experimental results and they concluded that these models are not completely capable of representing the behaviour of metallic foam.

The foam collapse mechanism under compressive load is different for the open-cell and closed-cell foam. The open-cell foam deforms initially by bending followed by

the formation of plastic hinges within the cell walls at higher strains. The deformation mechanism of the closed-cell foam is by the bending of the cell edges accompanied by stretching of the cell faces (Gibson and Ashby, 1997). However, the presence of intermetallic particles in the cell wall matrix influences the deformation behaviour. The simplified version of Gibson and Ashby model proposed for predicting the plastic collapse or plateau strength σ_{pl}^* and the elastic modulus E^* of cellular materials is given in terms of the relative density as (Gibson et al., 1989):

$$\frac{\sigma_{pl}^*}{\sigma_{ys}} = \alpha_1 \left(\frac{\rho^*}{\rho_s} \right)^m \quad (2.9)$$

$$\frac{E^*}{E_s} = \alpha_2 \left(\frac{\rho^*}{\rho_s} \right)^n \quad (2.10)$$

where σ_{ys} and E_s denote the yield strength and Young's modulus of the solid cell wall material. The predicted values for most metal foams: the materials constant m varies between 1.8 and 2.2, and n between 1.5 and 2.0, α_1 between 0.25 and 0.35, and α_2 between 0.1 and 4, depending on the structure of the foam (Lu and Ong, 2001). The more specific relation for repetitive hexagonal closed-cell metal foam by incorporating membrane stretching is given as (Triantafillou et al., 1989):

$$\frac{\sigma_{pl}^*}{\sigma_{ys}} = 0.3\phi^{3/2} \left(\frac{\rho^*}{\rho_s} \right)^{3/2} + (1-\phi) \left(\frac{\rho^*}{\rho_s} \right) + \frac{(p_o - p_{at})}{\sigma_{ys}} \quad (2.11)$$

where, ϕ is the fraction of solid contained in the cell edges; p_o is the gas pressure inside the cell and p_{at} is the atmospheric pressure. For all practical purposes the term $\frac{(p_o - p_{at})}{\sigma_{ys}}$

which represents the resistance of the air trapped in the closed-cell is considered to be negligible. A similar relationship for modulus is given as:

$$\frac{E^*}{E_s} = \phi \left(\frac{\rho^*}{\rho_s} \right)^2 + (1-\phi) \left(\frac{\rho^*}{\rho_s} \right) + p_o(1-2\nu^*) \left(E_s \left(1 - \frac{\rho^*}{\rho_s} \right) \right) \quad (2.12)$$

where, ν^* is the Poisson ratio and the term $\rho_o(1-2\nu^*)/E_s\left(1-\rho^*/\rho_s\right)$ is considered to be negligible for similar reasons given above. The Gibson Ashby model has its own limitation owing to the difficulty in the determination of ϕ in irregular foam structures. Nevertheless, the simplicity of the relationship makes it popular even today.

The influence of relative density and matrix alloy composition on mechanical property and energy absorption capacity is well established (Papadopoulos et al., 2004; Koza et al., 2003; Lu and Ong, 2001). But in recent years, experimental results have pointed out that along with the relative density, the cell size also has influence on the compression behaviour of foam (Andrews et al., 2001; Onck et al., 2001; Yu et al., 2007; Bin et al., 2007; Cao et al., 2006). Therefore, it is important to exercise control over the average pore diameter of the foam during foaming process and also it is necessary to consider pore diameter while modelling the mechanical property of foam.

2.8. Formulation of Problem

The invention of metallic foam dates long back in 1943 and after a dull period the potential of this material was realized later and research interest became more intense after 1990's. Metallic foams have always been trumped as light weight and stiff, ideal for structural applications where weight saving is paramount. But even today, metallic foams are insufficiently characterized, and understanding of the process is incomplete. It has not been yet fully possible to control the physical and morphological parameters of the foam (Matijasevic and Banhart, 2006). The exact interrelationship between properties and structure is not yet sufficiently known, but the task of the experimentalist still remains to obtain defect free structures (Matijasevic et al., 2006). In order to achieve this, a proper understanding of the metallic foam stabilization mechanism is needed (Banhart, 2006). Moreover, the potential for metallic foam to absorb impact energy during a vehicle crash is excellent due to the extended stress plateau during compression (Mukai et al., 2006). All these aspects of closed-cell aluminum foam are analyzed and discussed in this present work.

It is known from history that scientific research activities move rapidly towards the development of new material since its inception. But unfortunately many engineering

take-up is held back due to lack of adequate design data, experience and confidence. The present research work is undertaken to avoid such a predicament in the case of aluminum foam, which is even today not available commercially within India. As a part of the modelling effort, empirical models are developed for correlating the processing variables with the physical and morphological properties of foam. The mechanical properties and energy absorption capacity in static and dynamic compression state are evaluated and analyzed based on the structural properties. Statistical models are developed from the observed data by correlating the structural parameters with the compressive properties using multiple linear regression and artificial neural network (ANN).

Chapter 3

EXPERIMENTAL PROCEDURE AND MODELLING TOOLS

3.1. Introduction

This chapter details the experimental setup and procedures used for the synthesis and characterization of aluminum foams. The later part describes the modelling tools used to qualify the process variables and predict the mechanical properties. When making foams one encounters several process variables which have a lesser or greater influence on the foam characteristics. Design of experiments (DOE) technique is used to develop empirical models on the basis of critically chosen set of experiments. A design engineer would like to predict the mechanical properties of foam given its physical characteristics. Unlike conventional materials, metal foams exhibit an intricate and rather complex

structure which defies any empirical analysis. This calls for statistical modelling tools to simulate the mechanical property such as multiple linear regression and artificial neural network (ANN).

3.2. Design and Fabrication of Experimental Set-up

A top opening muffle furnace with a detachable stirrer arrangement and provision for powder addition during melting is designed for melting 1 kg of aluminum alloy (Ray, 1993). The furnace along with the temperature controller, stirrer speed controller and water quench bath are shown in Fig. 3.1. The entire set-up was fabricated in-house.

The furnace constitutes a heating chamber, which is an alumina muffle of size $200 \times 200 \times 300$ mm. An electrical resistance heating element, Kanthal A-1 wire of gauge 16 SWG is wound around the outer surface of the muffle. The top end of the muffle is open, whereas all the other sides are permanently insulated to prevent heat loss. The top end of the muffle is covered with two lids made of steel frame with a sturdy handle insulated by fire-clay bricks. Provisions were made on the lid to allow passage for the stirrer rod,

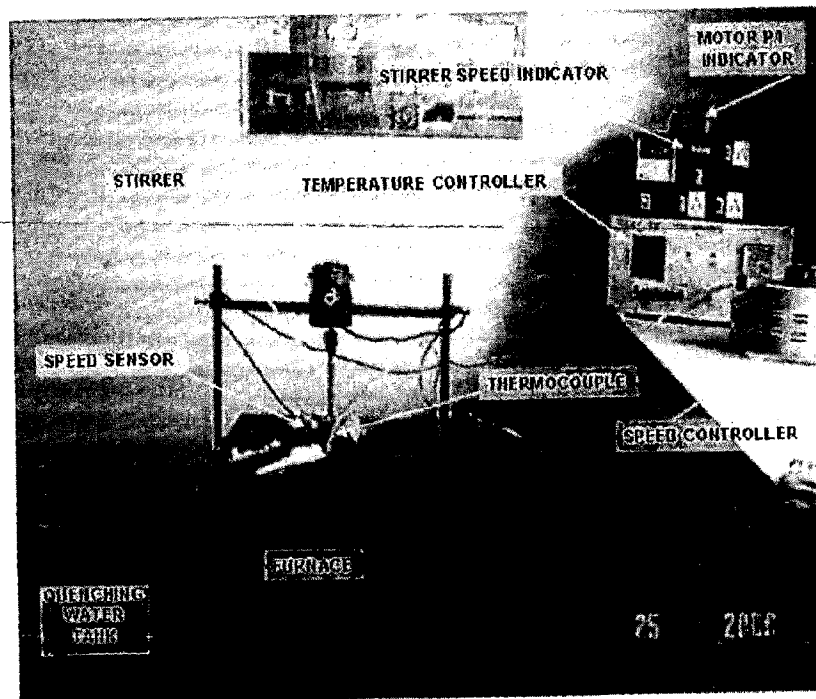


Fig. 3.1. Experimental arrangement used for making aluminum foam.

thermocouple and a long necked glass funnel to all chemicals during processing (Fig. 3.2). The muffle is insulated with fire-clay bricks, alundum powder, ceramic wool, asbestos sheets and asbestos powder and enclosed in a steel structure of dimension $500 \times 500 \times 500$ mm. The melting unit is designed to draw a maximum input power of 3.0 kW so as to reach a maximum temperature of 1100°C within the furnace (Cherepin and Mallik, 1967; Kanthal Handbook). The power supply unit consists of a PID controller with a calibrated chromel-alumel thermocouple for temperature control. The temperature is rather uniform within the furnace with variation of less than $\pm 2^{\circ}\text{C}$ within the crucible. The clay-graphite truncated cone shaped crucible of dimension: top 150 mm diameter, bottom 100 mm diameter and height 200 mm is used for melting and foaming the aluminum alloy.



Fig. 3.2. Photograph of the lid used to cover the top portion of the muffle furnace.

The stirrer is powered by a $\frac{1}{2}$ HP electric motor with a maximum speed of 1000 rpm. The stirrer speed is controlled by the variable voltage autotransformer. Two solid cylindrical columns are mounted on the sides of the furnace outer body which serve as a frame to fix the motor at various heights. The stirrer can be fixed to the shaft of the motor by screw coupling arrangement. The speed of the stirrer is continuously monitored by a digital non-contact type sensor arrangement.

The different stirrer designs used to optimize powder mixing in liquid melt is shown in Fig. 3.3. The first design had two stainless steel plates welded at 45° to the stainless steel axis (Fig. 3.3a). To avoid diffusion of iron into the melt the rod was coated with alumina. To overcome the problems associated with alumina coatings graphite stirrers were designed and fixed on to the steel axis using steel pins (Fig. 3.3 b, c and d). By taking into consideration all the constraints involved, such as the accessibility of pouring chemicals directly into the melt without spilling it over the stirrer, the short

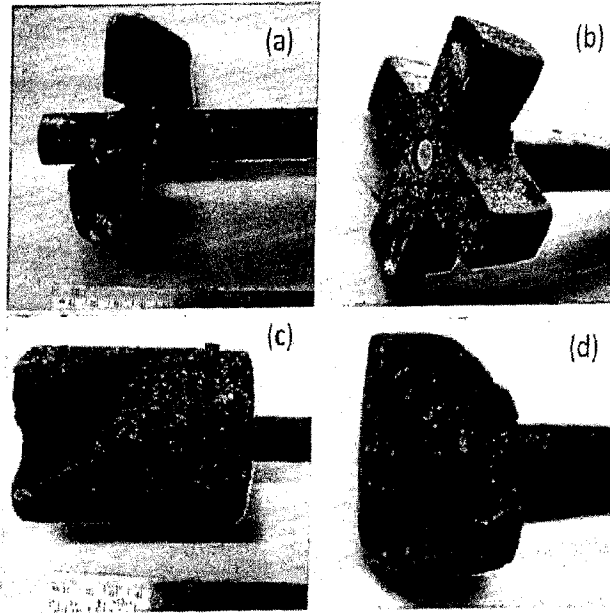


Fig. 3.3. Different types of stirrers used in the manufacture of aluminum foam.

graphite stirrer with two pitched blades at 45° pitch angle (Fig. 3.3d) is used for all the final experiments.

3.3. Experimental Procedure

Commercially available 6061 aluminum alloy was procured from Hindalco Industries Ltd, Mumbai, India. A master alloy was prepared by adding 4 wt. % of copper to the 6061 aluminum alloy and heated to 900°C for an hour and furnace cooled. The master alloy thus produced is used for all the experiments.

About 500 g of the master alloy is used in each foaming experiment. The master alloy is melted in the muffle furnace at 730°C . Subsequently the motor with stirrer arrangement is lowered on the sliding frame such that the stirrer is immersed in the liquid metal. Calcium metal powder (98.8 % metal basis and 16 mesh) is added through a glass funnel chute directly onto the metal surface while stirring at 750 rpm to increase the viscosity of the melt by oxidation. The amount of calcium (0.8 to 1.2 wt.%) and the stirring duration after addition (8 to 12 minutes) are varied to find the influence of

viscosity on the foam cell structure. Once the melt viscosity is appropriated for foaming, TiH₂ (99% metal basis and 325 mesh powder; Alfa Aesar) is added and stirred at a higher speed of 1000 rpm for 60 s. Then the stirrer is quickly removed from the melt by raising the motor on the sliding frame. The melt is held inside the furnace at 730°C (holding temperature) for different duration (60 to 140 s holding time) for allowing the degassing of TiH₂ leading to foaming. To ensure that entire

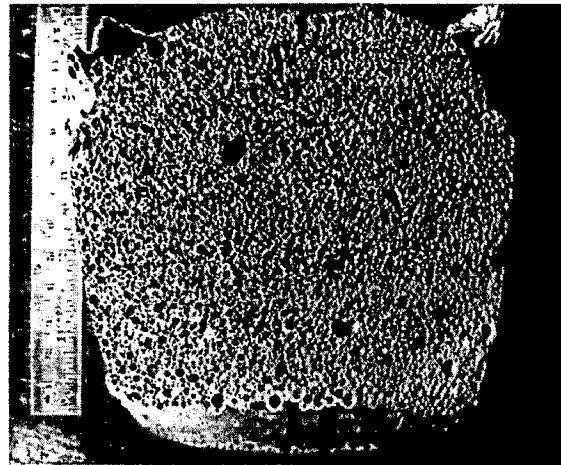


Fig. 3.4. Bisected foam structure for macrostructure characterization.

amount of TiH₂ (0.5 to 1.5 wt.%) is uniformly dispersed in the melt and not lost to the surface, the TiH₂ powder is wrapped in a thin lead foil and dropped below the melt surface. At the end of the holding time, the furnace lid is opened and the crucible containing the metal foam is taken out of the furnace with the help of the tongs and immersed in cold water kept nearby in a tank to solidify the melt and arrest the foaming process. Due to shrinkage associated with solidification the metal foam can be easily removed from the crucible.

3.4. Characterization Tools

3.4.1. Macrostructural Quantification

The foamed samples are bisected along the centre line, parallel to the foaming direction (Fig. 3.4). The 2D morphology of the foam structure is evaluated. The average pore diameter is estimated by calculating the pore diameter at different locations along the foaming direction and in the transverse direction. The formula $L=1.5/N$ is used, where N is the number of cells per unit length (Gibson and Ashby, 1997). The cell aspect ratio, K , is determined as $K=L_1/L_2$, where L_1 is the mean cell diameter transverse to the foaming direction and L_2 is the mean cell diameter in the foaming direction. The compression test specimens are cut approximately into regular square prism having height twice that of the width. The specimen dimensions are recorded and weighed accurately to

estimate relative density taking the base metal density as 2.721 g/cm^3 . The above data are carefully measured and tabulated for each experiment as they represent the structural properties of the foam.

3.4.2. X-ray Diffraction (XRD)

A photograph of the D8 Advance (Bruker AXS, Karlsruhe, Germany) X-ray diffractometer with computer control and analysis software is shown in Fig. 3.5. The XRD patterns of the calcium, TiH_2 powders are checked for purity and degradation effects. Powder samples of the cell wall material are taken to carry out phase identification. A diamond file is used to make powder samples while avoiding contamination. To suppress the aluminum peaks by increasing the relative quantity of the intermetallics the aluminum matrix is selectively leached by weak hydrochloric acid. The leached acid solution is filtered using ash-less filter paper, which is then completely burnt by heating at 600°C for 2 hours in an oven. The residual particles are weighed to estimate the weight fraction and subjected to XRD analysis. All XRD analysis were carried out in the $2\text{-}\theta$ range of $20^\circ - 90^\circ$ using $\text{Cu-K}\alpha$ radiation of $\lambda = 1.5413 \text{ \AA}$. The Goniometer speed is maintained at $1^\circ/\text{min}$. Peak identification was carried out by comparing with the relevant JCPDS X-ray diffraction data cards.

3.4.3. Optical Microscopy

Samples for microstructural examination were sectioned using slow speed isomet saw and then polished on a series of emery paper. The final polish was done with one

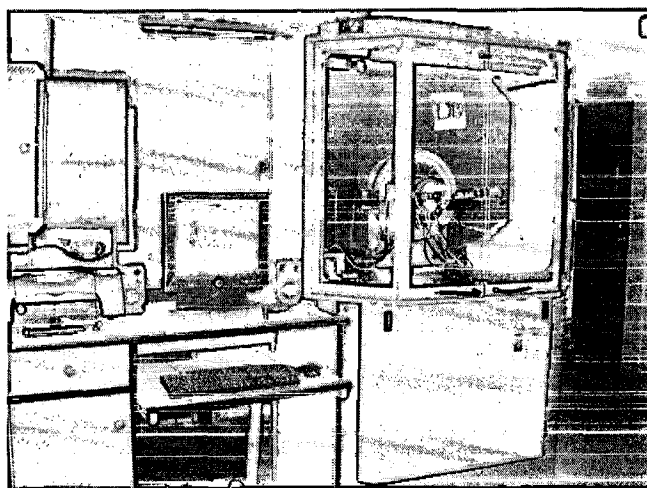


Fig. 3.5. D8 Advance, Bruker AXS, X-ray diffractometer used for X-ray powder analysis.

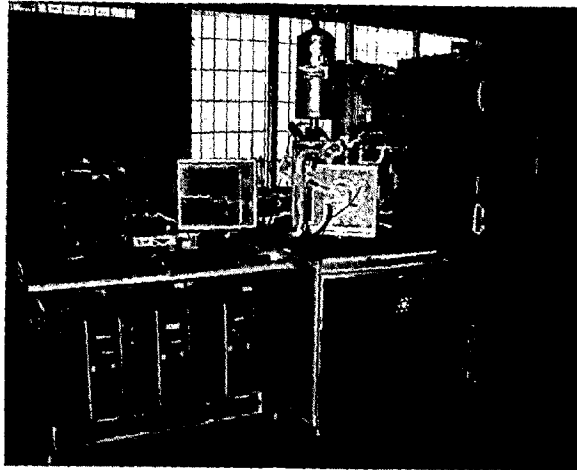


Fig. 3.6. Quanta 200 FEG, FEI Company's scanning electron microscopy fitted with EDS for elemental analysis.

micron diamond, followed by 0.05 micron alumina powder on a fine velvet cloth mounted on a rotating disc. An optical microscope, Olympus PME3, Tokyo, Japan was used for preliminary microstructural examination.

3.4.4. Scanning Electron Microscope (SEM) with Energy Dispersive X-ray Spectroscopy (EDS)

A photograph of the Quanta 200 FEG (FEI Company, Netherlands) with field emission source and EDS (Genesis 2000i) with resolution of $< 2.0 \text{ nm}$ @ 30 kV is shown in Fig. 3.6. Due to the field emission source giving high electron beam density the microscope has an optimum resolution of less than 2 nm. Microstructural analysis is carried out to investigate the morphology and distribution of the in-situ formed intermetallic and oxide particles in the aluminum cell wall matrix. Metallographic samples are prepared by standard metallographic procedure. The final polishing of the specimens is done in fine velvet polishing cloth using 3-OS-40 grade diamond paste, diluted and lubricated with Hifin fluid. The samples were coated with gold to avoid electron beam charging effects. The SEM studies are conducted with an electron beam accelerating potential of 15 or 20 kV. For microstructural observation, the back scattered mode is preferred to enhance the contrast between the elements of different atomic weight. On the other hand, the secondary mode is preferred for observing the surface morphology.

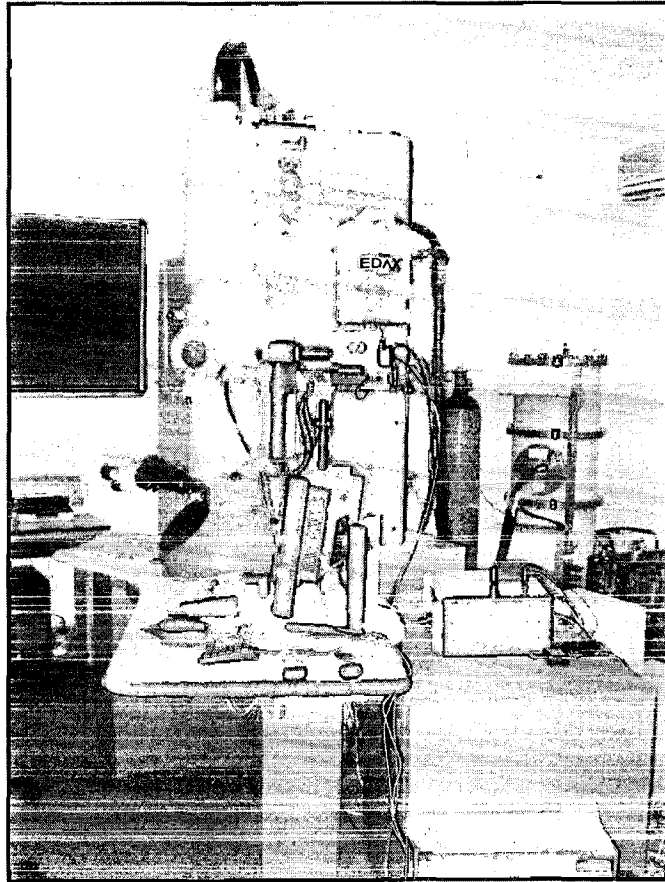


Fig. 3.7. TECHNAI 20G2-S-TWIN, FEI Company's 200kV transmission electron microscope.

The metallographically prepared samples were also subjected to EDS analysis. Particle/phase identification is done by correlating the elemental fraction with the XRD results. The elemental mappings of the cell wall surface and line analysis across particle interface were also carried out.

3.4.5. Transmission Electron Microscopy (TEM)

Special care has to be taken to prepare thin section from the dynamically deformed foam containing cell edges for TEM analysis. Initially, $\sim 500 \mu\text{m}$ thick slices are cut from the foam samples using a slow speed diamond saw. 3 mm disc specimens were punched and mechanically thinned to $\sim 100 \mu\text{m}$ thickness using emery paper down to 1000 grit. These specimens are then dimpled to $\sim 40 \mu\text{m}$ thickness on a dimpler, using one micron diamond paste as the grinding medium. The dimpled disc samples are further thinned using double ion beam thinning machine (PIPS 691, Gatan, USA) operated at 5 kV and 5-40 μA with a beam inclination $4\text{-}10^\circ$ under argon atmosphere. The prepared

samples are studied for microstructural characterization in the TEM (TECHNAI 20G2-S-TWIN) at an operating voltage of 200 kV (Fig. 3.7).

3.4.6. Thermo Gravimetric Analysis (TGA)

A photograph of the Pyrio Diamond TG/DTA (Perkin Elmer Instruments, Germany) is shown in Fig. 3.8. Thermo-gravimetric analysis is carried out on the TiH_2 powder procured for foaming the liquid melt to understand the thermal decomposition behaviour including the onset temperature of hydrogen gas evolution. To avoid oxidation effects the TGA analysis is carried out in argon atmosphere 50 to 1500°C. The heating rate is 10°C/min and the argon gas flow is maintained at 200 ml/min. The decomposition is indicated by the reduction loss due to the evolution of hydrogen gas.

3.4.7. Mechanical Testing

Foam specimens were subjected to compression test in quasi-static condition and dynamic condition at strain rates of $1 \times 10^{-3} \text{ s}^{-1}$ and $7.5 \times 10^2 \text{ s}^{-1}$ respectively in universal testing machine and split Hopkinson pressure bar (SHPB) apparatus for determining the Young's modulus, plateau stress and energy absorption capacity of foam.

3.4.7.1. Quasi-Static Compression test

The compression test specimens are cut approximately into regular square prism having height twice that of the width. The specimen dimensions are recorded and weighed accurately to estimate relative density by taking the base metal density as 2.721 g/cm^3 .

The compression tests are carried out in the universal testing machine (H25KS/05, Hounsfield, England) with computer interface for data acquisition and control (Fig. 3.9). Tests are

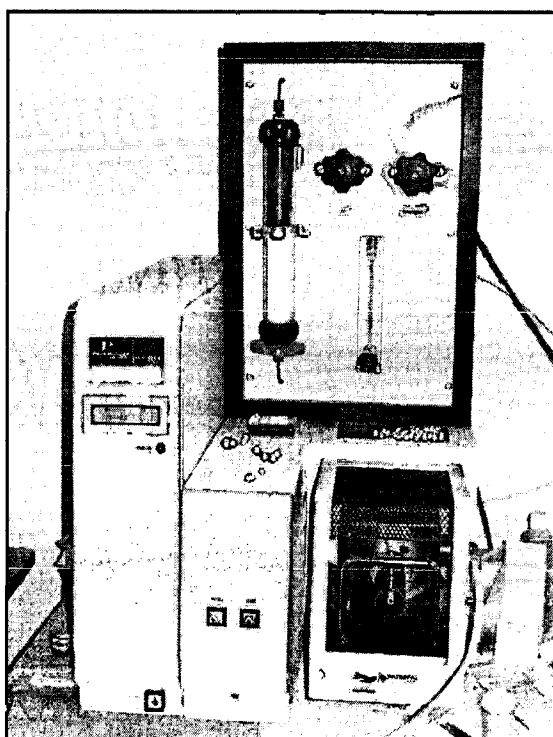


Fig. 3.8. Pyrio Diamond TG/DTA, Perkin Elmer Instruments, Germany used for thermo gravimetric analysis of TiH_2 powder.

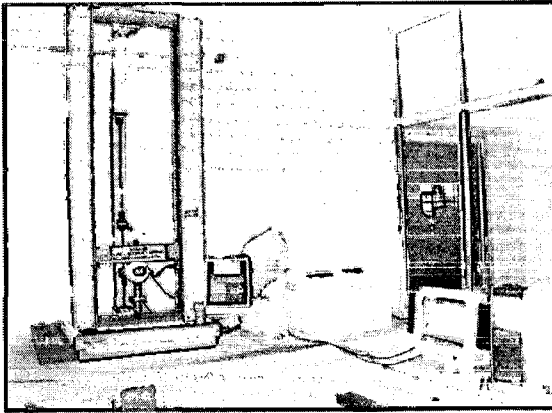
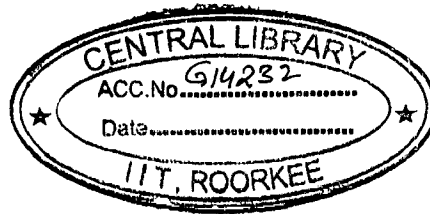


Fig. 3.9. H25KS/05, Hounsfield, England, universal testing machine used for quasi-static compression test.

conducted at a constant strain rate of $1 \times 10^{-3} \text{ s}^{-1}$ while taking care to reduce friction between the specimen and the plunger by the application of vacuum grease. The compressive stress-strain curves were obtained by dividing the applied load by the original specimen cross sectional area to obtain the applied nominal stress, and dividing the crosshead displacement by the original specimen height to obtain the nominal strain. The cross-head displacement of

the load frame is used for the displacement calculation as it is not possible to fix the extensometer on the foam specimen. Machine compliance was found to affect the actual displacements under various loading conditions. To negate the machine compliance effect, standard specimens were tested to find out the machine compliance factor and corrections were done accordingly.

The Young's modulus is calculated from the initial linear region of the stress-strain curve during loading and the unloading Young's modulus can be taken as twice as that of the loading modulus (Ramamurty and Paul, 2004; Sugimura, 1997). The unloading modulus is taken as the Young's modulus of aluminum foam, E^* . The plateau stress, σ_{pl} , is taken as the average stress value from 5 to 30 % strain during compression. The energy absorption per unit volume, W , is the area under the stress-strain curve up to densification as given by equation (3.1).

$$W = \int_0^{\epsilon_d} \sigma(\epsilon) d\epsilon \quad (3.1)$$

The densification strain, ϵ_d , is determined where the slope of the stress-strain curve increases steeply, accommodating more stress for small increment in strain. The determination of mechanical properties and energy absorption capacity of foam from the compression stress-strain curve was earlier schematically shown in Fig. 2.13.

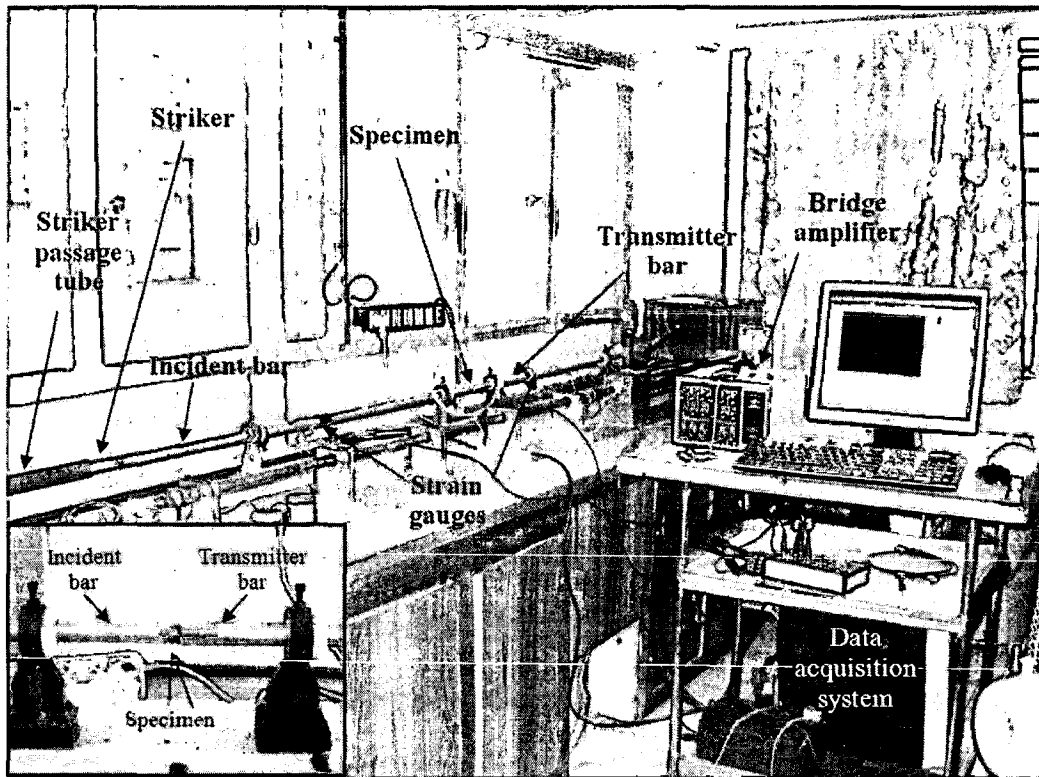


Fig. 3.10. Experimental setup of SHPB apparatus for dynamic testing of aluminum foam (Mechanical Engineering Department, IIT Kanpur).

3.4.7.2. Dynamic compression test

The apparatus consists of an air gun along with a passage tube, striker, an incident bar and a transmitter bar as shown in Fig. 3.10. Each bar is instrumented with a pair of electrical resistance strain gauges placed diametrically opposite and connected to the data acquisition system through a signal amplifier.

When the striker is fired by the air gun, it passes through the passage tube and impact at the incident bar. An elastic compressive stress pulse (incident pulse) is created in the incident bar and propagates towards the specimen, which is kept in between the incident and transmission bar (inside picture in Fig. 3.10). Due to the impedance mismatch at the incident bar-specimen interface, part of the incident pulse is reflected backwards (reflected pulse) into the incident bar and the rest is transmitted into the specimen. There will be further reflections and transmissions within the specimen and eventually a compressive pulse gets transmitted into the transmitter bar (transmitted pulse).

In conventional apparatus, solid steel bar are used and the cross-sectional area of the incident bar (A_i) and that of the transmitter bar (A_t) are same. When the applied axial loads on each face of the specimen are approximately constant, then the average compressive stress in the specimen (σ_{sp}) is given by:

$$\sigma_{sp} = E_t \left(\frac{A_t}{A_{sp}} \right) \varepsilon_t \quad (3.2)$$

where A_{sp} is the cross-sectional area of the specimen and E_t is the Young's modulus of the transmitter bar (Deshpande and Fleck, 2000b). Soft low impedance materials, like aluminum foam, allow the incident bar-specimen interface to move freely under stress wave loading causing most of the incident pulse to be reflected back. This phenomenon leads to very low amplitude in the transmitted signal (ε_t) through the specimen. Also the rise time of pulse is very less in conventional solid bar apparatus (Chen et al., 1994; Ravichandran and Subash, 1994). The plateau stress for the dynamic loading is evaluated as the average stress in the region where the stress remains constant (plateau) with respect to strain. The velocity of the striker impacting the incident bar is calculated from the expression given below.

$$V_{st} = \frac{2\sigma_i}{\rho_i C} \quad (3.3)$$

where $\sigma_i = E_b \varepsilon_i$, is the stress in the incident bar and ρ_i is the density of incident bar. The schematic diagram of the SPHB apparatus is given in Fig. 3.11. The average compressive stress in the specimen, σ_{sp} , measured by the conventional SHPB apparatus is given in equation (3.2). It is obvious from equation (3.2) that in order to increase the amplitude of the transmitted pulse, for the given stress level in the specimen, σ_{sp} , either

$\left(\frac{A_t}{A_{sp}} \right)$ or E_t has to be reduced and therefore a hollow aluminum tube having lesser cross-sectional area, A_t , is used as the transmitter bar (Chen et al., 1999). An aluminum alloy end cap is press fitted on the specimen-transmitter bar interface to support the specimen and to transmit the pulse without much disturbance. To filter the high-frequency components and to increase the rise time of the loading pulse, a cardboard disc (pulse

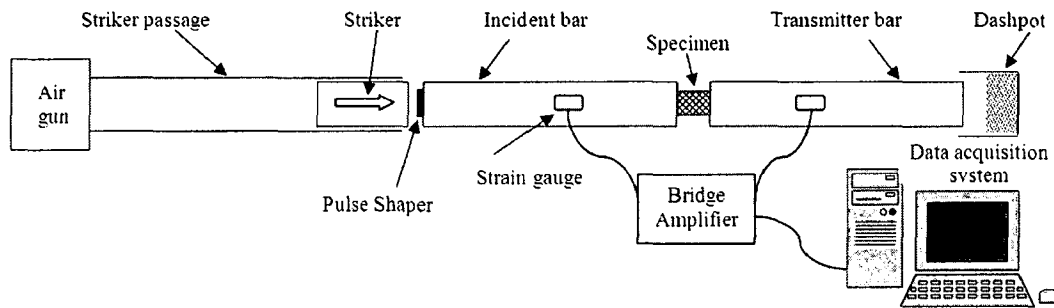


Fig. 3.11. Schematic sketch of the SHPB apparatus used for dynamic testing of aluminum alloy foams.

shaper) is placed at the impact end of the incident bar for shaping the pulse. A detailed analysis on pulse shaping technique is provided by Frew et al. (2001, 2002). Further it is assumed that the specimen reaches a state of equilibrium before failure. The detail about force equilibrium requirement is reported elsewhere (Mangapatnam and Venkitanarayanan, 2007).

In this study, the incident bar is 19.5 mm diameter and 1200 mm long instrumented with two strain gauges in the middle of the bar. The transmitter bar is 910 mm long and another two strain gauges of 120 ohms resistance are fixed at 300 mm from the specimen end. The outer diameter of the transmitter bar is 22.56 mm and the thickness of the tube is 1.55 mm. The striker passage tube is 1700 mm long having an inner diameter of 20 mm. The striker is 350 mm in length with the diameter of 19.5 mm, made from the same aluminum alloy.

3.5. Modelling Tools

The modelling and simulation of cellular metals is a field of research that has attracted considerable interest from researchers, foam manufacturers and industrial end-users. Generally, the real world of metallurgical processes, phenomena are too complex to be characterized solely by fundamental equations. As defined earlier, metallic foams consist of solid skeleton in the form of struts and/or cell walls. The volume fraction of voids in the material is very high and its structure is mostly inhomogeneous. In spite of various attempts by researchers for analytical solutions to predict the mechanical properties of foam, expected accuracy is not achieved. For the first time, in this work statistical approach is employed for process characterization with the use of design of

Table 3.1. The principle 2^{4-1} fractional factorial design.

Tests	A	B	C	D=ABC
	Coded Test Conditions			
(1)	-1	-1	-1	-1
a	1	-1	-1	1
b	-1	1	-1	1
ab	1	1	-1	-1
c	-1	-1	1	1
ac	1	-1	1	-1
bc	-1	1	1	-1
abc	1	1	1	1

experiments (DOE) technique. Also, the structure mechanical property correlation were modelled using multiple linear regression and with artificial neural network. Those modelling approaches used in the present work are briefed below.

3.5.1. Design of Experiments (DOE)

In the present work, experiments were conducted in two phases. In the first phase fractional factorial design is used to identify the major influencing parameter and in the second phase the identified significant parameters were studied for nonlinear conditions using central composite design. Both the experiments phases were designed and the results analysed by using the commercially available software program, Design Expert, version 7.1.3, Stat-Ease Inc., Minneapolis, MN.

3.5.1.1. Fractional Factorial Design

A designed experiment involves a series of tests in which useful and structured changes are made to the process variables so as to comprehend their measured responses. To begin with the experiments are confined to two levels (2^k) design, that is, each process parameter is tested at two values and k is the number of parameters or factors. Such an approach enables us to test several parameters with a minimum number of experiments, but at the same time assumes a linear relationship. The objective is then to identify the parameters which significantly influence the response. In our work we have executed a four factor design. The 2^4 design require 16 experiments, but implementing half-

Table 3.2. Central composite design conditions for 3² design.

Experiment No.	1	2	3	4	5	6	7	8	9	10	11	12	13
Process Factors	A	-1	0	1	-1	0	1	-1	0	-1	0	0	0
	B	-1	-1	-1	0	0	0	1	1	1	0	0	0

fractional factorial design will reduce the number of experiment by half, that is, $2^{4-1} = 8$ designed experiments.

The half-fractional factorial experiment, often referred to as the 2^{k-1} fractional factorial design is constructed for any 2^k experiment by following two sequential steps. Table 3.1 illustrates how the principle half-fractional factorial design is constructed for $k=4$. If the four factors are named as A, B, C and D, and the high and low values for each factor are coded as -1 and 1. Then the test level for factor D are found by multiplying together the numbers in the columns of the base design, $D=ABC$. D is called the design generator for this fractional factorial design.

Once the significant process parameters are identified with the two level design, those parameter are studied for non-linear relationships at a higher-level design.

3.5.1.2. Central Composite Design (CCD)

The most popular design having factors at three levels is the central composite design (CCD), which is capable of handling non-linear relationship between process parameters and the response. A face centered central composite design is a special case of the central composite design. It is not rotatable like usual CCD, because the axial points, is always set equal to one, no matter how many factors are included in the experiment. Because of this the axial points will trace out a cuboidal region on the response surface. They are sometimes called as cuboidal designs.

The CCD design experiments are conducted in a randomized run order to protect against the effects of time-related variables and also to satisfy the statistical requirements

of independence of observations. If two factors are considered at its 3 levels (coded) such as low (-1), medium (0) and high (+1), then the values of the variables in coded terms for each experiment by CCD experimental design is shown in Table 3.2.

3.5.1.3. Response Surface Methodology (RSM)

In many experimental situations, it is possible to represent independent factors in quantitative form. Then these factors can be thought of as having a functional relationship or response as follows,

$$Y = \varphi (x_1, x_2, \dots, x_k) \pm e_r \quad (3.4)$$

This response is between Y and x_1, x_2, \dots, x_k of k quantitative factors. The function φ is called response surface or response function. The residual e_r measures the experimental errors (Cochran and Cox, 1962). For a given set of independent variables, a characteristic surface is responded. When the mathematical form of φ is not known, it can be approximated satisfactorily within the experimental region by a polynomial. Higher the degree of polynomial better is the correlation but at the same time costs of experimentation becomes higher.

3.5.1.4. The Analysis of Variance (ANOVA)

The analysis of variance is a collection of statistical models, and their associated procedures, in which the observed variance is partitioned into components due to different explanatory variables. The fundamental technique is, partitioning of the total sum of squares into components related to the effects used in the model.

The total corrected sum of squares (SS_T) which is a measure of overall variability in the data and is given by:

$$SS_T = \sum_{i=1}^a \sum_{j=1}^n (y_{ij} - \bar{y}_{..})^2 \quad (3.5)$$

where $\bar{y}_{..}$ represent the grand average of all the observations.

The number of degrees of freedom (df) describes the associated sums of squares. Dividing SS_T by the appropriate number of degrees of freedom gives the sample variance

of the y 's. The sample variance is a standard measure of variability. The corrected sum of squares SS_T can be finally written as,

$$\sum_{i=1}^a \sum_{j=1}^n (y_{ij} - \bar{y}_{..})^2 = n \sum_{i=1}^a (\bar{y}_{i.} - \bar{y}_{..})^2 + \sum_{i=1}^a \sum_{j=1}^n (y_{ij} - \bar{y}_{i.})^2 \quad (3.6)$$

Equation (3.6) states that the total variability in the data, as measured by the total corrected sum of squares, can be partitioned into a sum of squares of the differences between the treatment averages and the grand average, plus a sum of squares of the differences of observations within treatments from the treatment average. Now, the difference between the observed treatment averages and the grand average is a measure of the differences of observations within a treatment from the treatment average is due to random error. Thus, the equation (3.6) can be symbolically written as,

$$SS_T = SS_{\text{Treatments}} + SS_E \quad (3.7)$$

where $SS_{\text{Treatments}}$ is called the sum of squares due to treatments and SS_E is called the sum of squares due to error. If there are $a \times n = N$ number of observations; SS_T has $N-1$ degrees of freedom. There are ' a ' levels of the factor (and a treatment means), so $SS_{\text{Treatments}}$ has $a-1$ degrees of freedom. Finally, within any treatment there are n replicates providing $n-1$ degrees of freedom with which to estimate the experimental error. Because there are a treatments, there is $a(n-1) = an-a = N-a$ degrees of freedom for the error.

If there are no differences between the a treatment means, the variation of treatment averages from the grand average can be used to estimate σ^2 .

$$\frac{SS_{\text{Treatments}}}{a-1} = \frac{n \sum_{i=1}^a (\bar{y}_{i.} - \bar{y}_{..})^2}{a-1} \quad (3.8)$$

is an estimate of σ^2 if the treatment means are equal. The analysis of variance (equation 3.6) provides with two estimates of σ^2 – one based on the inherent variability within the treatments and the other based on the variability between treatments. If there are no differences in the treatment means, these two estimates should be very similar, and if they are not, then the observed difference must be caused by differences in the treatment means. The quantities

$$MS_{\text{Treatments}} = \frac{SS_{\text{Treatments}}}{a-1} \quad (3.9)$$

and

$$MS_E = \frac{SS_E}{N-a} \quad (3.10)$$

are called mean squares. The test of the hypothesis of no treatment means can be performed by comparing $MS_{\text{Treatments}}$ and MS_E .

Because the degrees of freedom for $SS_{\text{Treatments}}$ and SS_E add to $N-1$, the total number of degrees of freedom, Cochran's theorem implies that $SS_{\text{Treatments}}/\sigma^2$ and SS_E/σ^2 are independently distributed chi-squared random variables. Therefore, if the null hypothesis of no difference in treatment means is true, then the ratio

$$F_o = \frac{SS_{\text{Treatments}}/(a-1)}{SS_E/(N-a)} = \frac{MS_{\text{Treatments}}}{MS_E} \quad (3.11)$$

is distributed as F with $a-1$ and $N-a$ degrees of freedom. The equation (3.11) is the test statistic for hypothesis of no difference in treatment means. An F -test is any statistical test in which the test statistic has an F -distribution if the null hypothesis is true.

In general, MS_E is an unbiased estimator of σ^2 . Also, under the null hypothesis, $MS_{\text{Treatments}}$ is an unbiased estimator of σ^2 . However, if the null hypothesis is false, the expected value of $MS_{\text{Treatments}}$ is greater than σ^2 .

$$F_o > F_{\alpha, a-1, N-a} \quad (3.12)$$

Alternatively, the P-value approach can also be used for decision making. Computing formulas for the sums of squares are obtained by rewriting and simplifying the definitions of $MS_{\text{Treatments}}$ and SS_T in equation 3.6. This yields

$$SS_T = \sum_{i=1}^a \sum_{j=1}^n y_{ij}^2 - \frac{y_{..}^2}{N} \quad (3.13)$$

and

$$SS_{\text{Treatments}} = \frac{1}{n} \sum_{i=1}^a y_i^2 - \frac{y_{..}^2}{N} \tag{3.14}$$

The error sum of squares is obtained by subtraction as

$$SS_E = SS_T - SS_{\text{Treatments}} \tag{3.15}$$

The test procedure is summarized in Table 3.3, which is called as analysis of variance table.

3.5.2. Multiple Linear Regression Model

With multiple linear regression, it is assumed that the dependent data, y_i , depends linearly on several independent variables, x_1, x_2, \dots, x_k . If it is assumed there are three independent variables, then the data points are of the form,

$$(x_{11}, x_{21}, x_{31}, y_1), (x_{12}, x_{22}, x_{32}, y_2), (x_{13}, x_{23}, x_{33}, y_3), \dots, (x_{1N}, x_{2N}, x_{3N}, y_N)$$

and the goal is to minimize the sum by the equation and to get the values of a and b .

$$R^2 = \sum_{i=1}^N (a_1 x_{1i} + a_2 x_{2i} + a_3 x_{3i} + b - y_i)^2 \tag{3.16}$$

The minimum of the sum above will occur at critical points. By solving the derivatives, the values of a 's and b 's are estimated, which will give the 'best fit' line for the given data set. This is also called as the least square estimation or maximum likelihood

Table 3.3. Simple general analysis of variance table.

Source of Variation	Sum of Squares	Degrees of Freedom	Mean Square	F_o
Between treatments	$SS_{\text{Treatments}} = n \sum_{i=1}^a (\bar{y}_i - \bar{y})^2$	$a-1$	$MS_{\text{Treatments}}$	$F_o = \frac{MS_{\text{Treatments}}}{MS_E}$
Error (within treatments)	$SS_E = SS_T - SS_{\text{Treatments}}$	$N-a$	MS_E	
Total	$SS_T = \sum_{i=1}^a \sum_{j=1}^n (y_{ij} - \bar{y})^2$	$N-1$		

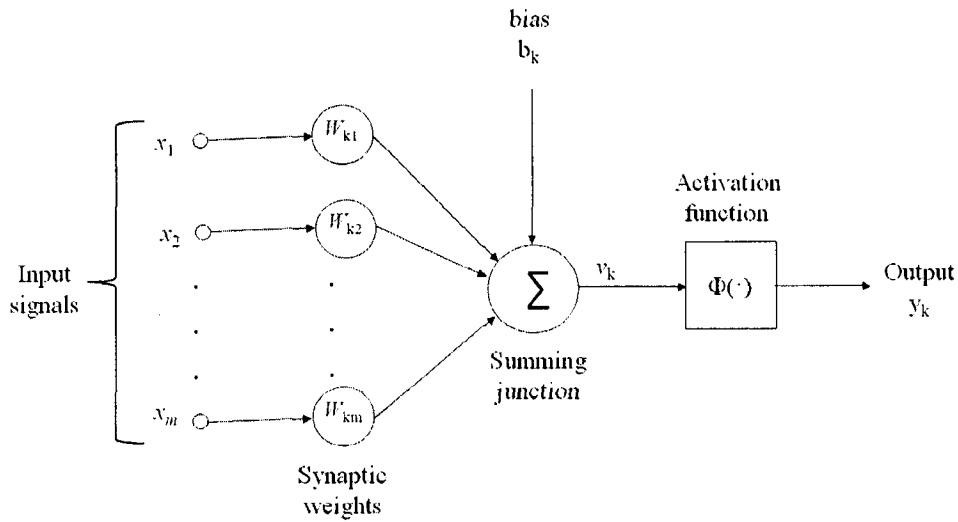


Fig. 3.12. Nonlinear model of a neuron in artificial neural network.

estimation. In particular, hand calculation is inadvisable when the number of independent variables is more than 2, because of the amount of work involved (Thomas and Ronald, 1981; Ryan, 1990; Draper and Smith, 1966). The multiple regressions are done using the Microsoft Excel, Office 2007 Software.

3.5.3. Artificial Neural Network (ANN) Model

Neural network is constructed as a model having layers of neurons with suitable weighted interconnections. The input layer consists of a string of neurons that serves for input variables to the model, while the output layer may involve one or more neurons depending on the number of output variables. The interim layers, also called as hidden layers, may vary from one to more, and serve as non-linear associations that map the input to the output data.

In mathematical terms, a neuron k is described by the following equations and schematically in Fig. 3.12.

$$u_k = \sum_{j=1}^m w_{kj} x_j \quad (3.17)$$

$$v_k = u_k + b_k \quad (3.18)$$

$$y_k = \Phi(v_k) \quad (3.19)$$

where x_1, x_2, \dots, x_m are the input signals; $w_{k1}, w_{k2}, \dots, w_{km}$ are the synaptic weights of neuron k ; u_k is the linear combiner output due to the input signals; b_k is the bias; $\Phi(\cdot)$ is the activation function; v_k is the induced local field or activation potential; and y_k is the output signal of the neuron (Haykin, 2004).

3.5.3.1. Activation Function

A particular activation function is chosen to satisfy some specification of the problem that the neuron is attempting to solve. A variety of activation functions are available. The three most commonly used functions are:

(a) Step function

This function defined as

$$\left. \begin{aligned} a &= 0, n < 0 \\ a &= 1, n \geq 0 \end{aligned} \right\} \tag{3.20}$$

(b) Linear function

This function is defined as

$$a = n \tag{3.21}$$

(a) Sigmoid function

This function is defined as

$$a = 1 / (1 + e^{-n}) \tag{3.22}$$

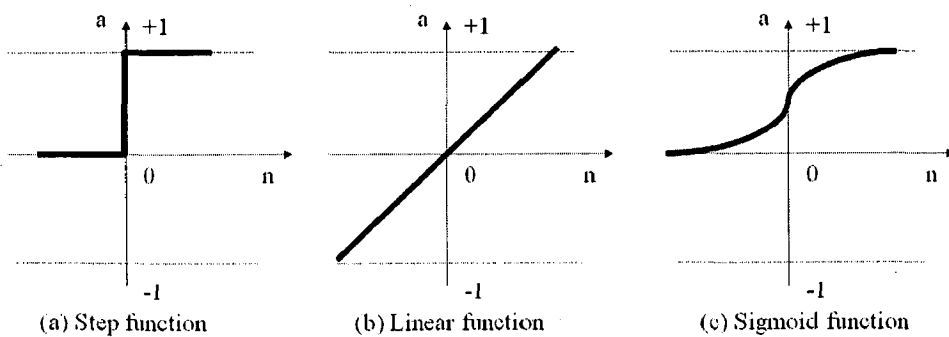


Fig. 3.13. Basic functional forms of the activation functions used in the development of ANN model.

Fig. 3.13 shows the basic functional forms of these functions. Generally, the sigmoid functions are used in the inner layers of the network and linear functions are used in the output layer of the ANN architecture.

3.5.3.2. Learning Rules

A learning rule is a condition or criteria for modifying the weights and biases of a network. There are many types of learning rules. They fall into three broad categories as, supervised learning, unsupervised learning and reinforcement learning rules (Martin et al., 1996).

In supervised learning, the learning rule is provided with a set of examples (the training set) of proper network behaviour: $\{x_1, d_1\}$, $\{x_2, d_2\}$, ... , $\{x_q, d_q\}$, where, x_q is input to the network and d_q is the corresponding target or the desired output. As the inputs are applied to the network, the network outputs are compared to the targets. The learning rule is then used to adjust the weights and biases of the network in order to move the network outputs closer to the targets.

In unsupervised learning, the weights and biases are modified in response to network inputs only. There are no target outputs available.

Reinforced learning is similar to supervised learning, except that instead of providing correct output for each network input, the algorithm is only given a grade. This type of learning is less common. The supervised learning is used for the models developed in this work.

3.5.3.3. Training Process

The training of network is done by changing the number of hidden layers and also by varying the number of neurons (processing elements) until the prescribed error tolerance is achieved. Once the training procedure is finalized, the adjusted synaptic weights of all the connecting nodes along with the bias are used for predicting the output, $y_k(n)$. The output signal of neuron k , $y_k(n)$ is compared to a desired response or output, $d_k(n)$ and an error, $e_k(n)$ is produced, where n denotes the time step of an iterative process.

$$e_k(n) = d_k(n) - y_k(n) \quad (3.23)$$

This error signal, $e_k(n)$ actuates a feed-back control mechanism to apply a sequence of corrective adjustments to the synaptic weights to neuron, k . This objective is achieved by minimizing the index of performance, $\varepsilon(n)$, defined as

$$\varepsilon(n) = \frac{1}{2} e_k^2(n) \quad (3.24)$$

The synaptic weight adjustment, $\Delta w_{kj}(n)$ applied to the synaptic weight w_{kj} at time step n is defined by

$$\Delta w_{kj}(n) = \eta e_k(n) x_j(n) \quad (3.25)$$

where η is a positive constant that determines the rate of learning. The updated value of synaptic weight w_{kj} is determined by

$$w_{kj}(n+1) = w_{kj}(n) + \Delta w_{kj}(n) \quad (3.26)$$

where $w_{kj}(n)$ and $w_{kj}(n+1)$ are the old and new values of synaptic weights, respectively.

The ANN model performance can be analyzed by the performance index called Mean Square Error, MSE, given by

$$\text{MSE} = \frac{1}{2N} \sum_{n=1}^N [d_k(n) - y_k(n)]^2 \quad (3.27)$$

where $y_k(n)$ and $d_k(n)$ are the n^{th} predicted and measured output, N is the number of training patterns and n denotes the time step of an iterative process.

Chapter 4

RESULTS AND DISCUSSION

4.1. Introduction

Closed-cell aluminum foams are processed by liquid melt method using TiH_2 as blowing agents in the present work. Different morphological and physical properties of the foam are accessed by varying the process parameters. It is understood that the properties of the foam are determined by the cell structure and the microstructure of the cell wall material. The design of experiments (DOE) technique is used to evaluate the influence of the process parameters on the final cell structure. Based on the experimental results, empirical models are developed to qualify the influence of process parameters in achieving the desired cell structure and consequently, the mechanical properties.

Microstructural analysis was carried out in the cell wall material to identify the in-situ formed particles present and to corroborate the results with the stability and strength of the foam. The mechanical properties of foam are determined at the quasi-static

Table 4.1. Chemical composition of as received commercial 6061 aluminum alloy.

Composition	Al	Mg	Si	Ca	Cr	Fe	Mn	Cu
Weight %	98.136	0.674	0.598	0.213	0.180	0.114	0.058	0.018
Atom %	98.342	0.749	0.576	0.144	0.093	0.055	0.028	0.008

condition in the universal testing machine, and also at a higher strain rate in dynamic condition using split Hopkinson pressure bar (SPHB) apparatus. The Young's modulus, plateau stress and energy absorption capacity of foam are derived from the compression stress versus strain curve.

In the absence of good analytical relationship relating the mechanical properties to the structural properties of the foam, statistical modelling approach such as multiple linear regression and artificial neural network are carried out. These models use easily quantifiable structural parameters such as, the relative density, average cell diameter and cell aspect ratio to predict the mechanical property of the foam. The following sections contain the results and discussion of the present work in the order mentioned in this section.

4.2. Process Influence on Foam Structure

The experimental procedure followed in the present work for the processing of closed-cell aluminum foam is detailed in section 3.3. The chemical composition of 6061 aluminum alloy procured from Hindalco Industries Ltd, Mumbai, India as determined by electron probe micro-analyzer (EPMA) is shown in Table 4.1. Under different process conditions 6061 aluminum alloy did not form foam structure. The cross section of one such failed sample is shown in Fig. 4.1. On the other hand, when the alloy is modified by adding 4 wt. % of copper, foam could be

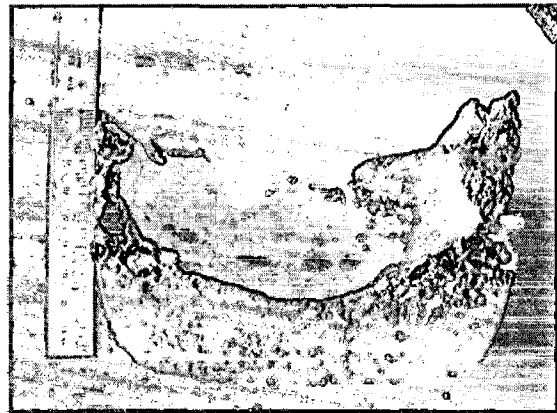


Fig. 4.1. Improper foaming of 6061 aluminum alloy without addition of copper.

synthesized. The microstructure of 6061 aluminum alloy is shown in Fig. 4.2(a), which does not show any network structure. However, the microstructure of the aluminum-copper alloy formed a continuous network of Al_2Cu intermetallic (Fig. 4.2(b)). It appears that the intermetallic structure formed due to the addition of 4 wt. % of copper is essential for foaming. This alloy is used as the master alloy for all foaming experiments in the present work.

The thermogravimetric analysis (TGA) of TiH_2 indicates that the decomposition of TiH_2 starts at around 500 °C and is completed at 570 °C (Fig. 4.3). The amount of TiH_2 addition decides not only the amount of hydrogen release, but also the viscosity of the melt by the formation of intermetallics and thereby the stability of the foam (Yang

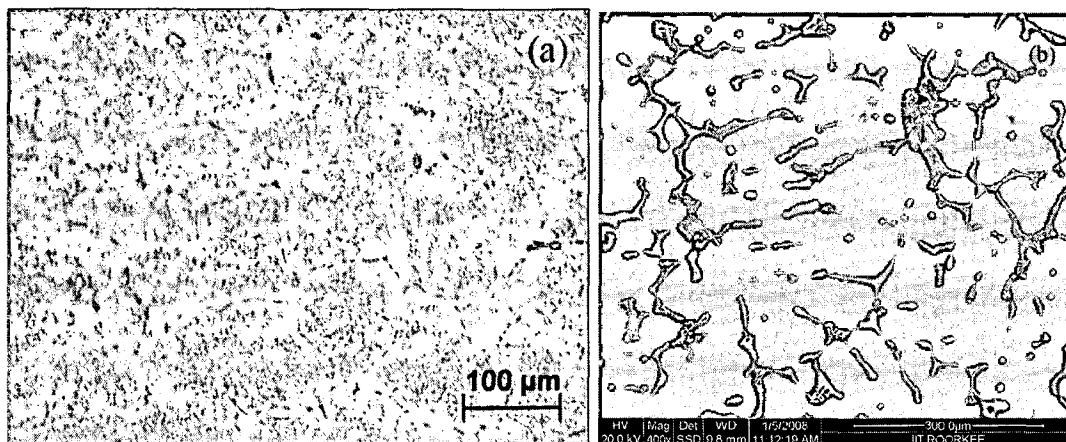


Fig. 4.2. (a) Optical micrograph of as received 6061 aluminum alloy and (b) Backscattered SEM image of 6061+4 wt.% Cu+1.0 wt.% Ca cast metal alloy showing Al_2Cu intermetallic network.

and Nakae, 2000). When foaming with 0.5 wt.% of TiH_2 , the amount of hydrogen gas release is insufficient to create enough porosity and the relative densities of the foam made are usually greater than 0.3 (Banhart, 1999). However, uniform cell structure with less drainage is obtained when the amount of TiH_2 is around 1.0 wt.%.

From the analysis of experimental procedure given in section 3.3, the following process variables have been identified which could influence the foam process.

1. Composition of base alloy.
2. Stirrer design.
3. Initial temperature of the melt.

4. Amount of calcium added.
5. Stirring speed after calcium addition.
6. Stirring time after calcium addition.
7. Amount of TiH_2 addition.
8. Stirring speed after TiH_2 addition.
9. Stirring time after TiH_2 addition.
10. Holding temperature during the foaming process.
11. Holding time for foaming.
12. Rate of solidification.

Poor choice of factors and their ranges, resulting from incomplete engineering knowledge of the manufacturing process, is likely to result in an unsatisfactory solution – no matter how good the experimental plan and ingenuity in data analysis. Based on the literature published and by conducting many pilot experiments (Fig. 4.4), the process parameters which do not significantly influence the process are identified as follows: composition of base alloy, stirrer design, initial temperature, stirrer speed after calcium and TiH_2 addition, holding temperature and solidification rate. These parameters were judiciously maintained constant at an optimum value and the influence of the other parameters were carefully analysed using design of experiments as outlined in the following subsections (Montgomery, 2001; Mark Evans, 2003).

4.2.1. Design of Experiments and Analysis: Phase-I

An experiment is a test or a series of tests conducted in which designed changes

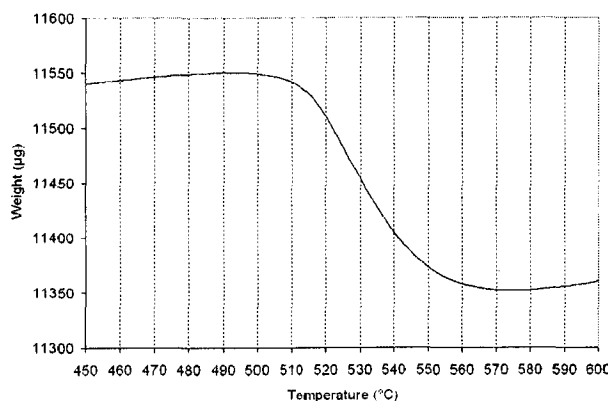


Fig. 4.3. Thermo gravimetric analysis showing the decomposition TiH_2 occurs between 510 to $570^{\circ}C$ during a $10^{\circ}C/min$ scan.

are made in the process parameters to observe and identify the reasons for the observed changes in the output (response). As briefed in section 3.5.1, DOE is a technique for planning and conducting experiments and analyzing the responses to bring out valid and objective conclusions. The initial set of process parameters selected for analysis in the first phase of the experiment: half-fractional factorial design are:

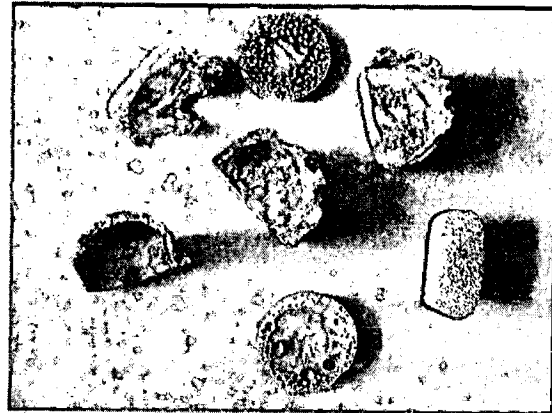


Fig.4.4. Some of the pilot experiment results conducted to identify the significant process variables and their range.

- (A) The holding time after TiH_2 addition
- (B) The amount of TiH_2 addition
- (C) The amount of calcium metal addition
- (D) The stirring time after calcium addition

The constructed half-fractional factorial design of experiments, 2^{4-1} with the selected variables and their levels is given in Table 4.2. The structural and the mechanical properties of the foam samples processed are evaluated as detailed in section 3.4.1 and 3.4.7.1, respectively, and recorded experiment wise and given in Table 4.3. An analysis of variance (ANOVA) is then carried out separately for each of the response (structural parameters) in order to test the model signification and suitability. The ANOVA result of each structural response models is evaluated to find the significance of effects and if there are interactions between the process variables.

4.2.1.1. Analysis of Relative Density Model

The analysis of variance is done for studying the influence of process parameters on the relative density of the foam during manufacturing and the ANOVA table is given in Table 4.4. The model F value is given by:

$$F_o = \frac{MS_{Model}}{MS_E} = \frac{3.27 \times 10^{-3}}{8.98 \times 10^{-3}} = 36.4276$$

The model F-value of 36.43 implies that the model is significant (Montgomery, 2001). The p-value of 0.0269 indicates that there is only 2.69% chance that a "Model F-Value"

of this large could occur due to noise. Values of "Prob > F" less than 0.0500 indicate that the model terms are significant. In this case factor B, which is the amount of TiH₂

Table 4.2. Half-fractional factorial design conditions for foaming closed-cell aluminum foam.

Exp. No.	Process Parameters			
	Holding Time	Amount of TiH ₂	Amount of Ca	Stirring time for Ca
	(A) s	(B) wt.%	(C) wt.%	(D) min
1	80	0.6	0.8	8
2	120	0.6	0.8	12
3	80	1.0	0.8	12
4	120	1.0	0.8	8
5	80	0.6	1.2	12
6	120	0.6	1.2	8
7	80	1.0	1.2	8
8	120	1.0	1.2	12

Table 4.3. The structural properties of the foam (responses) obtained from the experiment by half-fractional factorial design.

Exp. No.	Weight of Master Alloy g	Foaming Height mm	Structural Properties		
			Relative Density	Average Pore Diameter (mm)	Aspect Ratio
1	404	62.00	0.2666	2.8830	1.0190
2	521	63.50	0.2659	3.1200	1.3636
3	534	91.00	0.1757	3.0625	1.0416
4	454	86.00	0.1964	3.1365	1.0720
5	484	63.00	0.2252	3.0200	1.0544
6	491	69.00	0.3053	2.9230	1.0397
7	458	82.00	0.1574	3.2736	1.0605
8	384	87.50	0.1785	3.2995	1.1997

Table 4.4. ANOVA results for relative density model by half-fractional factorial design.

Source	Sum of Squares	df	Mean Square	F value	p-value Prob > F
Model	1.64×10^{-2}	5	3.27×10^{-3}	36.4276	0.0269
A-Holding time	1.51×10^{-3}	1	1.51×10^{-3}	16.8135	0.0546
B-Amt. of TiH ₂	1.36×10^{-2}	1	1.36×10^{-2}	151.4768	0.0065
C-Amt. of calcium	3.15×10^{-4}	1	3.15×10^{-4}	3.5111	0.2018
D-Stirring time	4.12×10^{-4}	1	4.12×10^{-4}	4.5827	0.1656
AC	5.17×10^{-4}	1	5.17×10^{-4}	5.7539	0.1386
Residual	1.80×10^{-4}	2	8.98×10^{-5}		
Total	1.65×10^{-2}	7			

addition is the most significant model term. p-values greater than 0.1000 indicate that those factors in the model are not significant. From the results of p-values, it can be concluded that the factor C-the amount of calcium addition, and the factor D-the stirring time after addition of calcium have very less influence on the relative density of the foam. Eventhough, there is an interaction effect AC, between the holding time and the amount of calcium added, they are less significant as indicated by the p-value.

In addition to the basic analysis of variance, the program displays some additional useful information indicating the precision of the model (Table 4.5). The quantity “R-Squared” is defined as

$$R^2 = \frac{SS_{\text{Model}}}{SS_{\text{Total}}} = \frac{1.64 \times 10^{-2}}{1.65 \times 10^{-2}} = 0.9891$$

and is loosely interpreted as the proportion of the variability in the data “explained” by the analysis of variance model. The “adjusted” R^2 is a variation of the ordinary R^2 statistics that reflects the number of factors in the model and will get adjusted for the “size” of the model.

Table 4.5. Model precision index values of the relative density model in half-fractional factorial design.

Std. Dev.	9.48×10^{-3}	R-Squared	0.9891
Mean	1.2788	Adj R-Squared	0.9620
C.V. %	0.7412	Pred R-Squared	0.8262
PRESS	2.87×10^{-3}	Adeq Precision	15.3565

$$R_{\text{Adj}}^2 = 1 - \frac{SS_E / df_E}{SS_{\text{Total}} / df_{\text{total}}} = 1 - \frac{1.80 \times 10^{-4} / 2}{1.65 \times 10^{-2} / 7} = 0.9620$$

“Std. Dev.” is the square root of the error mean square, $\sqrt{8.98 \times 10^{-5}} = 9.48 \times 10^{-3}$, and “C.V.” is the coefficient of variation, defined as $(\sqrt{MS_E} / \bar{y}) \times 100$. The coefficient of variation measures the unexplained or residual variability in the data as a percentage of the mean of the response variable. “PRESS” is an acronym for Prediction Error Sum of Squares, and it is computed from the prediction errors obtained by predicting the i th data point with a model that includes all observations except the i th one. A model with a small value of PRESS indicates that the model is likely to be a good predictor. The “prediction R^2 ” statistics is computed as

$$R_{\text{Pred}}^2 = 1 - \frac{\text{PRESS}}{SS_{\text{Total}}} = 1 - \frac{2.87 \times 10^{-3}}{1.65 \times 10^{-2}} = 0.8262$$

This indicates that the full model is able to explain about 82.62 percent of the variability in the new data. The “Adequate Precision” statistics is computed by dividing the difference between the maximum predicted response and the minimum predicted response by the average standard deviation of all predicted responses. Values that exceed four usually indicate that the model will give reasonable performance in prediction. “Adeq Precision” measures the signal to noise ratio. In this model, the value of 15.3565 indicates that the model prediction is adequate.

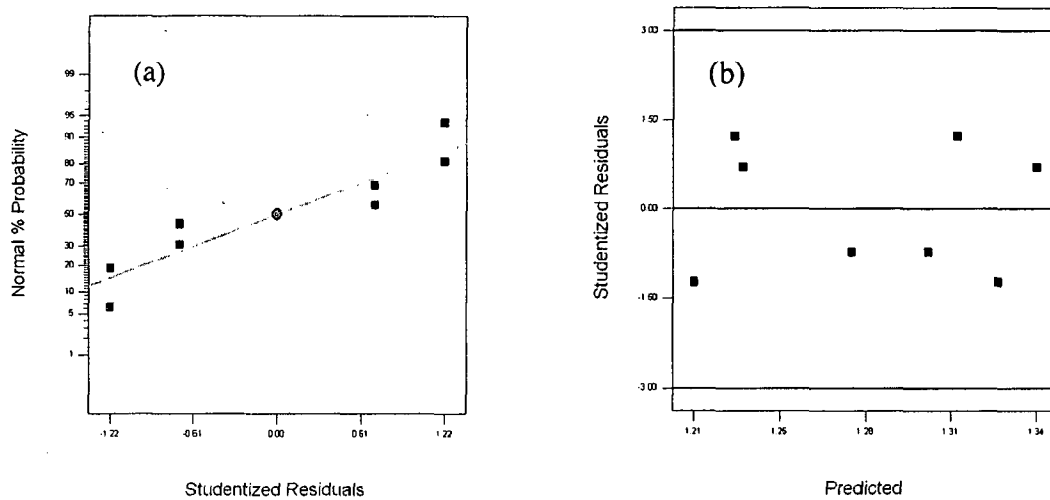


Fig. 4.5. Diagnostic plots for the relative density model (a) normal probability Vs studentized residual and (b) Studentized residual Vs Predicted values.

The decomposition of the variability in the observations through an analysis of variance identity is a purely algebraic relationship. However, the use of the partitioning to test formally for no differences in treatment means requires that certain assumptions be satisfied. It is usually unwise to rely on the analysis of variance until the validity of these assumptions has been checked. Violations of the basic assumptions and model adequacy can be easily investigated by the examination of residuals. There are different diagnostic tools available within the software to validate the model. The general one is the plot of normal probability against the studentized residuals. Studentized residual is the number of standard deviations of the actual values from their respective predicted values. The plot for the present model is shown in Fig. 4.5(a). The straight line indicates that the model is valid and there is no abnormality. Similarly, the studentized residuals with predicted values given in Fig. 4.5(b) shows that the spread of the studentized residuals are approximately the same across all levels of the predicted values confirming the model adequacy. Once the model is validated and found satisfactory, inference from the graph can be drawn.

The perturbation plot compares the effect of all the factors about a particular point in the design space. The response is plotted by changing only one factor over its range while holding the other factors constant. Fig. 4.6 is the perturbation chart for the relative

density of the foam. A steep slope or curvature in a factor shows that the response is more sensitive to that factor. This plot could be used to identify those factors that most affect the response (relative density). From Fig. 4.6 it can be observed that the slope of curve B is steep, indicating that the amount of TiH_2 addition is the most influential process parameter to vary the relative density of the foam during processing.

The slope is nearly constant over the design space for the amount of TiH_2 from 0.6 wt.% to 1.0 wt.%, while keeping the other process parameter at the middle of their range, called reference points (see inset of Fig. 4.6.). The negative slope of curve B, points that higher the amounts of TiH_2 lower the relative density. After the amount of TiH_2 addition, the holding time has next the significant influence on the relative density. However, the other two process

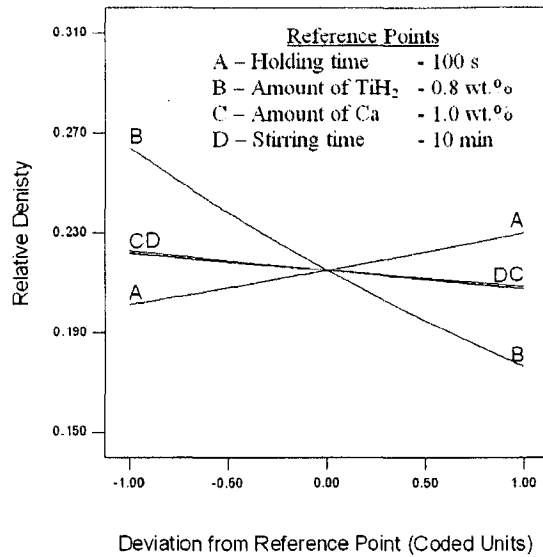


Fig. 4.6. Perturbation plot for relative density model showing the sensitivity of the individual process parameters in the half-fractional factorial design.

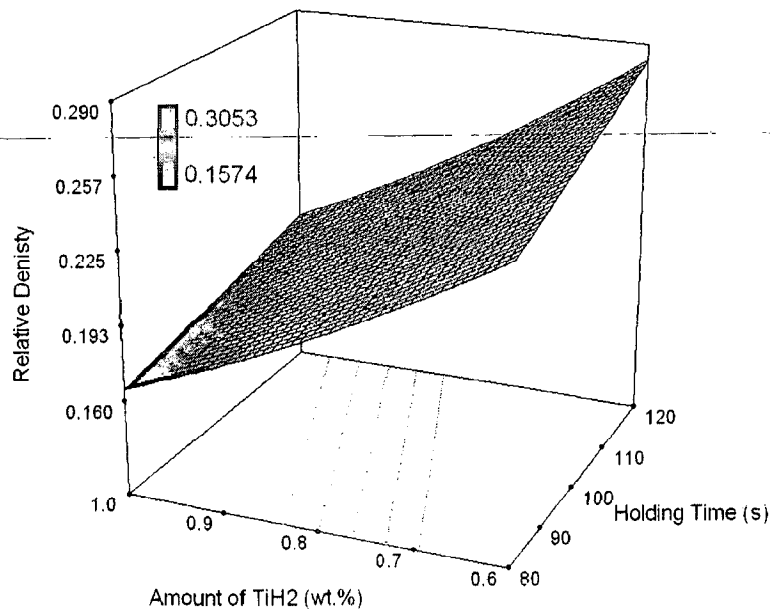


Fig. 4.7. Response surface plot of relative density in relation with the amount of TiH_2 and holding time (half-fractional factorial design).

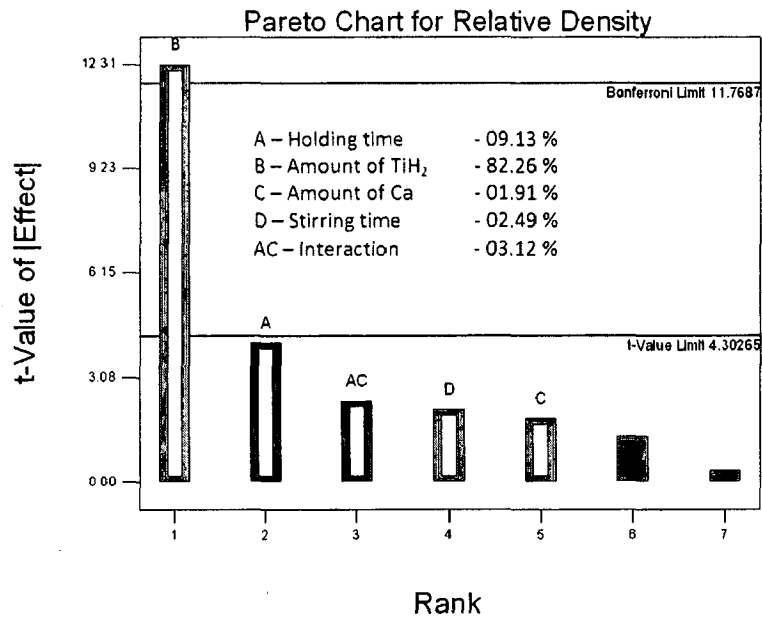


Fig. 4.8. Pareto chart of standardized effects signifying the effects of process variables in the design for relative density.

parameters, the amount of calcium addition and stirring time after calcium addition have little influence on the relative density of foam. The three-dimensional response plot of relative density in relation to the amount of TiH₂ and holding time is shown in Fig. 4.7. The constant response contour lines indicate that lower relative density foams are achieved by increasing the amount of TiH₂ and decreasing the holding time. The Pareto chart of standardized effects was carried out in order to show the significant effects of the process variables in the design. The percentage contribution of the factors involved in the model is also given along with the Pareto chart. From Fig. 4.8, it can be seen that for relative density, the amount of TiH₂ is the major influencing parameter followed by the holding time in the process variable range considered.

4.2.1.2. Analysis of Average Pore Diameter Model

The analysis of variance is done on the results obtained from the half-fractional experiments for the average pore diameter is listed in Table 4.3. The ANOVA table for the same is given in Table 4.6. The model F-value is very high at 119.25, signifying the model as significant. The corresponding p-value of 0.0083 of the model suggests that there is only 0.83% chance that this large F-value could have occurred due to noise. The average pore diameter model precision index values are given in Table 4.7. The "Pred R-Squared" of 0.9465 is in reasonable agreement with the "Adj R-Squared" of 0.9883.

"Adeq Precision" measures the signal to noise ratio; the ratio of 34.883 indicates that the signal is adequate. These precision index confirms that the model can be used to navigate the design space. Similarly, the violations of the basic assumptions and model adequacy are investigated by the examination of residuals using the diagnostic tools with the software and the model is validated.

Table 4.6. ANOVA results for average pore diameter model by half-fractional factorial design.

Source	Sum of Squares	df	Mean Square	F value	p-value Prob > F
Model	0.46	5	0.092	119.25	0.0083
A-Holding time	0.29	1	0.29	376.11	0.0026
B-Amt. of TiH ₂	0.026	1	0.026	34.16	0.0281
C-Amt. of calcium	0.12	1	0.12	157.64	0.0063
D-Stirring time	0.019	1	0.019	24.30	0.0388
AC	3.152×10^{-3}	1	3.152×10^{-3}	4.07	0.1810
Residual	1.547×10^{-3}	2	7.737×10^{-4}		
Total	0.46	7			

Table 4.7. Model precision index values of the average pore diameter model in half-fractional factorial design.

Std. Dev.	0.028	R-Squared	0.9967
Mean	3.08	Adj R-Squared	0.9883
C.V. %	0.90	Pred R-Squared	0.9465
PRESS	0.025	Adeq Precision	34.883

The Pareto chart is shown in Fig. 4.9 for the average pore diameter. The chart indicates that the amount of holding time is the major influencing parameter for average pore diameter in the design space considered.

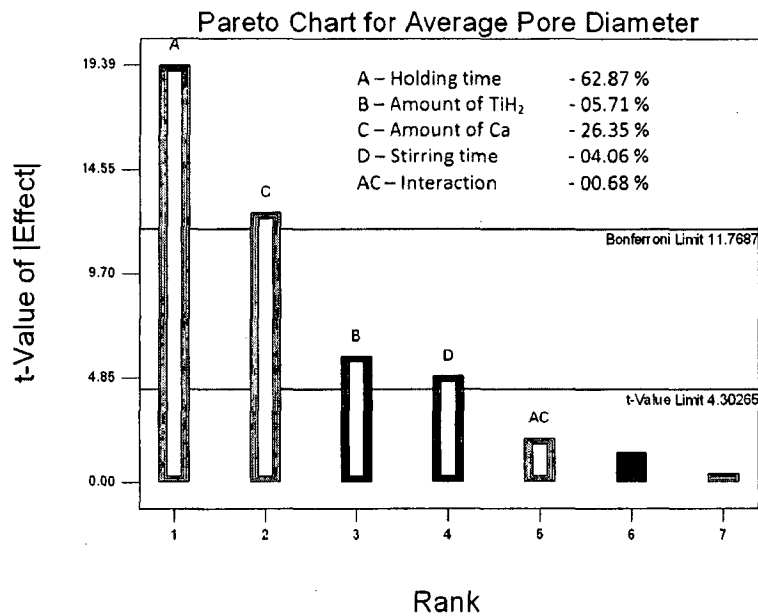


Fig. 4.9. Pareto chart of standardized effects signifying the effects of process variables in the design for the pore diameter.

Table 4.8. ANOVA results for cell aspect ratio model by half-fractional factorial design.

Source	Sum of Squares	df	Mean Square	F value	p-value Prob > F
Model	0.10	5	0.021	11.38	0.0827
A-Holding time	0.041	1	0.041	22.50	0.0417
B-Amt. of TiH ₂	3.846×10^{-3}	1	3.846×10^{-3}	2.12	0.2830
C-Amt. of calcium	7.577×10^{-3}	1	7.577×10^{-3}	4.17	0.1780
D-Stirring time	0.023	1	0.023	12.76	0.0702
AD	0.028	1	0.028	15.35	0.0594
Residual	3.635×10^{-3}	2	1.818×10^{-3}		
Total	0.11	7			

Table 4.9. Model precision index values of the cell aspect ratio model in half-fractional factorial design.

Std. Dev.	0.043	R-Squared	0.9660
Mean	1.10	Adj R-Squared	0.8811
C.V. %	3.89	Pred R-Squared	0.4566
PRESS	0.058	Adeq Precision	9.644

4.2.1.3. Analysis of Cell Aspect Ratio Model

The analysis of variance from the results of the half-fractional factorial designed experiment is done to identify the major process parameters that affect the cell aspect ratio. The ANOVA result for the cell aspect ratio is given in Table 4.8. The aspect ratio model value for F is 11.38, which corresponds to p-value of 0.0827. The "Pred R-Squared" of 0.4566 is not as close to the "Adj R-Squared" of 0.8811 as one might normally expect. Other precision index values of the model are given in Table 4.9. These values indicate a large block effect or a possible problem with the model and/or data. However, still the model gives the general inference about the major influencing process parameter which increases the cell aspect ratio. The p-value of holding time is 0.0417 indicating that the holding time is the major parameter to influence the aspect ratio. The detailed analysis on the aspect ratio is done in the second phase of experiments.

4.2.1.4. Inference from Phase-I Experiments

The empirical models for (1) relative density, (2) average pore diameter and (3) cell aspect ratio of the half-fractional factorial design of experiment are detailed in the above sections. The perturbation chart shown for relative density in Fig. 4.6 helps to compare the effect of all the factors at a particular point in the design space. A steep slope or curvature in a factor shows that the response is sensitive to that factor. So, it can be understood from Fig. 4.6, that the amount of TiH_2 addition and the holding time are the major influencing factors for the relative density variation, which is the most important physical property of foam governing the mechanical property of the material. The Pareto chart is used to graphically summarize and display the relative importance of the parameters used in the group. The Pareto charts also indicates the major influencing factor as the amount of TiH_2 for relative density and the holding time for average pore

Table 4.10. CCD experimental conditions of the two significant process variables.

Exp. No.	Process Parameters	
	Holding time (A) s	Amount of TiH ₂ (B) wt.%
1	60	0.5
2	100	0.5
3	140	0.5
4	60	1
5	100	1
6	140	1
7	60	1.5
8	100	1.5
9	140	1.5
10	100	1
11	100	1
12	100	1
13	100	1

diameter (Fig. 4.8 and Fig. 4.9). Similarly the holding time is identified as the most important parameter to control the cell aspect ratio. Based on these observations of the phase-I experiments, it is understood that (1) the holding time and (2) the amount of TiH₂ addition are the two major influencing process parameters which controls the physical and morphological properties of the foam.

4.2.2. Phase-II: Central Composite Design Experiments and Results

Once the major influencing process variables are identified by half-fractional factorial design; the response surface methodology (RSM) is employed to evaluate the relevance of these process parameters on the final cell structure in a wider range by central composite design (CCD). In the first phase, only two levels for each process parameters were considered for analysis assuming that the variation within that range as linear. In the second phase, by conducting experiments at three levels for each of the process parameters, non-linear dependence is also analyzed. Holding time is varied from 60 to 140 s and, the amount of TiH₂ addition, selected for analysis is varied from 0.5 wt.% to 1.5 wt.%. The central composite design consisting of a factorial (2³) with 4 extra central

Table 4.11. The structural properties of the foam (responses) obtained for the CCD experimental conditions.

Exp. No.	Weight of Master Alloy g	Foaming Height mm	Structural Properties		
			Relative Density	Average Pore Diameter (mm)	Aspect Ratio
1	486	55.0	0.3506	2.1862	1.0084
2	483	55.0	0.3368	2.2399	1.0906
3	489	63.0	0.2859	3.3248	1.1800
4	479	90.0	0.1587	2.5593	1.0099
5	459	98.0	0.1479	3.2003	1.0866
6	491	104.0	0.1230	3.4067	1.1197
7	480	135.0	0.1024	3.2044	1.1012
8	480	130.0	0.0949	3.6440	1.0250
9	481	115.0	0.0801	4.4859	1.2589
10	478	100.0	0.1070	3.1390	1.0626
11	485	100.0	0.1084	2.9314	1.0846
12	480	105.0	0.1163	3.2316	1.1070
13	482	101.0	0.0999	3.2507	1.0844

point of the experimental design is applied. The CCD design consists of 13 experiments conducted in a randomized run order to protect against the effects of time-related variables and also to satisfy the statistical requirements of independence of observations. The two variables are taken at its 3 levels (coded) as low (-1), medium (0) and high (+1) and the values of the variables for each experiment are shown in Table 4.10. The structural properties obtained for the corresponding experiments as in Table 4.10 are given in Table 4.11 respectively. An analysis of variance (ANOVA) is then carried out separately for each structural property response in order to test the model signification and suitability and derive inferences from the process.

4.2.2.1. Influence of major Process Parameters on Relative Density

The relative density is the major influencing structural parameter of foam which dictates the mechanical property of the foam. Therefore, it is of interest to determine the influence of the process parameters on relative density. The results of the thirteen

Table 4.12. ANOVA results tabulated for response surface quadratic model for relative density using CCD.

Source	Sum of Squares	df	Mean Square	F value	p-value Prob > F
Model	0.11	5	0.021	62.49	0.0001
A-Holding time	2.509×10^{-3}	1	2.509×10^{-3}	7.30	0.0306
B-Amt. of TiH_2	0.081	1	0.081	234.81	0.0001
AB	4.494×10^{-4}	1	4.494×10^{-4}	1.31	0.2904
A ²	1.573×10^{-4}	1	1.573×10^{-4}	0.46	0.5205
B ²	0.019	1	0.019	54.75	0.0001
Residual	2.406×10^{-3}	7	3.437×10^{-4}		
Total	0.11	12			

experiments are fed to the Design Expert software and the analysis of the variance is done to validate the obtained quadratic model to analyze the influence of the process variables on the relative density of foam. The ANOVA table for this model is given in Table 4.12. The response surface quadratic model for relative density has F-value of 62.49 and the corresponding p-value of 0.0001 indicates that the model is significant with only 0.01% chance that a “Model F-value” could have occurred due to noise. The ‘Lack of Fit’ value of 0.93 implies that the Lack of Fit is not significant relative to the pure error. Non-significant lack of fit is good. In this model, the factor B, which is the amount of TiH_2

Table 4.13. Precision index values of the surface response model for the relative density using CCD.

Std. Dev.	0.019	R-Squared	0.9781
Mean	0.16	Adj R-Squared	0.9624
C.V. %	11.41	Pred R-Squared	0.9168
PRESS	9.136×10^{-2}	Adeq Precision	21.664

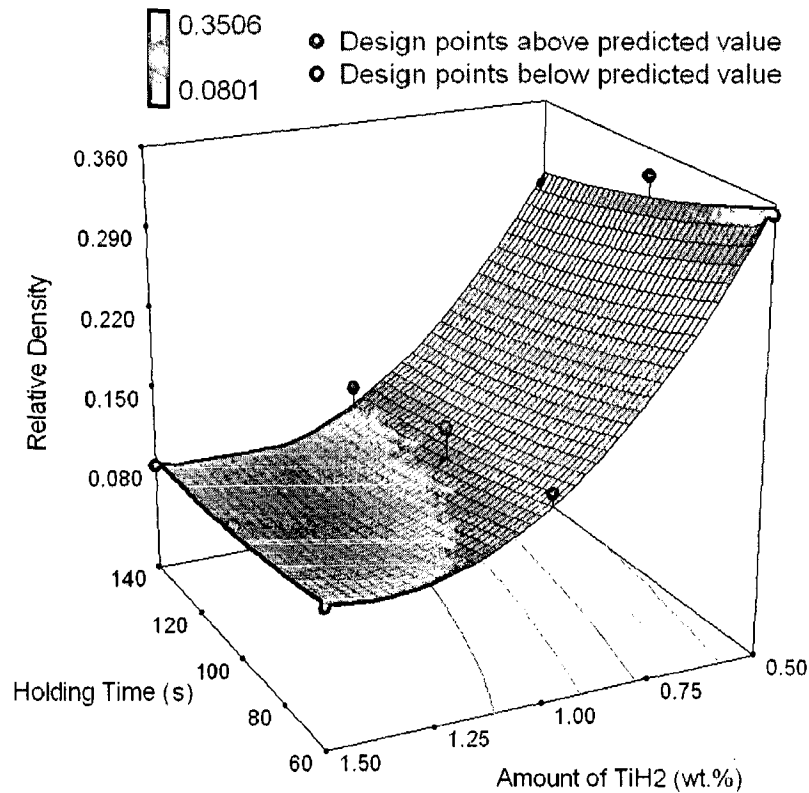


Fig. 4.10. Response surfaces estimated using the CCD derived empirical model for relative density.

addition, is the major deciding factor for the variation in relative density of the foam evolved in the process. This is confirmed by the very high F-value (234.81) for that factor. There is very little interactive effect between the two process variables (i.e. AB) as seen by the p-value of 0.2904, which is higher (>0.05).

The Design Experts software gives more information to validate the model and to derive inference from the results obtained. Table 4.13 gives the precision index values of the surface response model for relative density. The “Pred R-Squared” of 0.9168 is in reasonable agreement with the ‘Adj R-Squared’ of 0.9624. “Adeq Precision” measures the signal to noise ratio and the value of 21.664 indicates an adequate signal. Similarly, the diagnostic tools are used to check the violations of assumptions and the model adequacy. The relative density model by the surface response methodology is shown in Fig. 4.10 and the corresponding perturbation chart in Fig. 4.11. It can be seen that the amount of TiH₂ addition in the melt alters the density of the foam much more in comparison to the holding time variation. Increasing the amount of TiH₂ addition and extended holding time leads to foams of lower density.

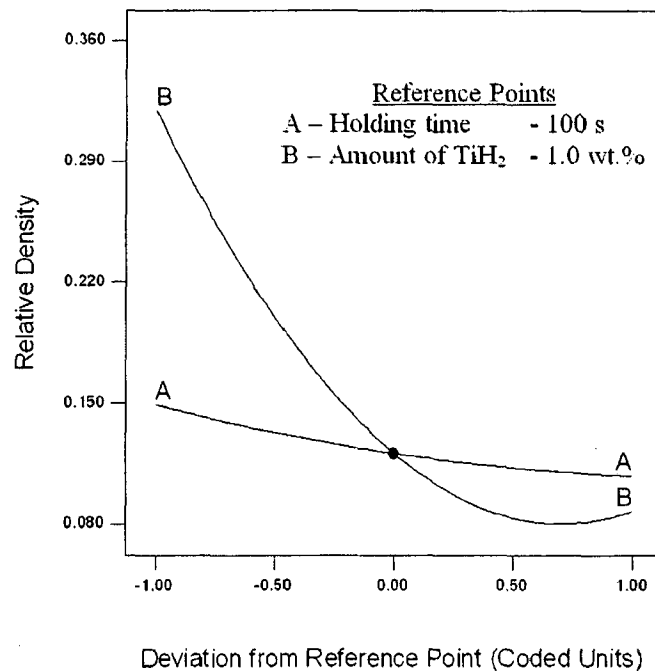


Fig. 4.11. Perturbation plot of response surface quadratic model using CCD for relative density prediction.

From Fig. 4.11 it is understood that the dependence of the relative density with amount of TiH₂ addition is non-linear. The rate of decrease in relative density is high during the TiH₂ addition, from 0.5 to 1.0 wt.%, which is also reported by Yang and Nakae (2000), whereas with further increase in the amount of TiH₂ addition the relative density reaches a saturation value of about 0.08. This points to that, around 1.0 wt.% TiH₂ addition to the melt is sufficient enough to produce stable foam with uniform cell structure. However, increasing the amount TiH₂ further does not increase the foaming efficiency. Similarly, decrease in relative density with longer holding time occurs due to the expansion of pores with the release of hydrogen gas. The variation is uniform throughout the selected experimentation range. Similar trends were also reported in literature (Song and Nutt, 2007; Song et al., 2000; Song et al., 2001; Yang and Nakae, 2003; Yang and Nakae, 2000). However, the influence of holding time to tailor the relative density of foam is less in comparison with the amount of TiH₂. The second-order polynomial equations of the response surface model obtained for relative density with coded factors (equation 4.1) and with actual factors (equation 4.2) are given below:

$$\text{Relative density} = 0.12 - 0.020 A - 0.12 B + 0.011 AB$$

$$+ 7.547 \times 10^{-3} A^2 + 0.083 B^2 \quad (4.1)$$

$$\begin{aligned} \text{Relative density} = & 0.8343 - 1.9846 \times 10^{-3} A - 0.9453 B \\ & + 5.3 \times 10^{-4} AB + 4.7166 \times 10^{-6} A^2 + 0.3302 B^2 \pm e_r \end{aligned} \quad (4.2)$$

where A is the holding time (s), B is the amount of TiH₂ added (wt.%) and e_r is the experimental error. The experimental error can be taken as three times the standard deviation. This empirical model can be used to predict the relative density of the closed-cell aluminum foam on the basis of the present experimental work.

4.2.2.2. Influence of major Process Parameters on Average Pore Diameter

The control of pore size is important for achieving uniform cell structure, since next to relative density the average pore diameter significantly influences the mechanical property of the foam. Following a pattern similar to earlier models, it is important to test the signification of the model and to validate it before drawing any conclusion from the ANOVA results. The ANOVA table for the average pore diameter model by surface response is given in Table 4.14. The model F-value of 52.07 and the corresponding p-value of 0.0001 of the model suggests that there is only 0.01% chance that this large F-value could have occurred due to noise. Similarly, the high F-value and the corresponding low p-value of the two factors involved, namely, the holding time and the amount of TiH₂, suggest that the two factors are equally important parameters in determining the

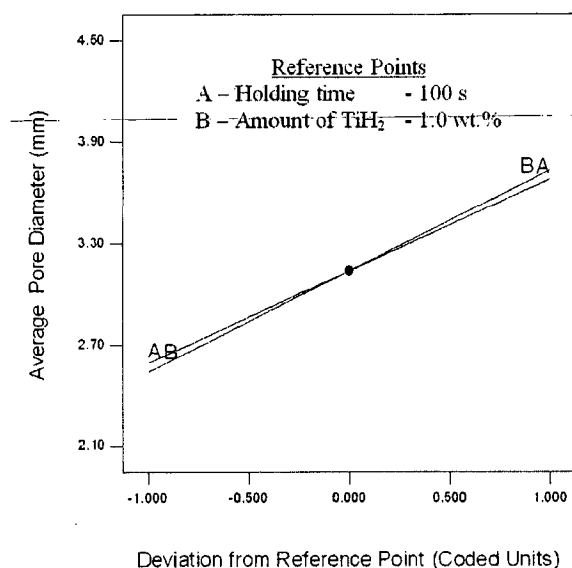


Fig. 4.12. Perturbation plot of response surface linear model using CCD for the average pore diameter prediction.

Table 4.14. ANOVA results tabulated for response surface linear model for average pore diameter using CCD.

Source	Sum of Squares	df	Mean Square	F value	p-value Prob > F
Model	3.92	2	1.96	52.07	0.0001
A-Holding time	1.78	1	1.78	47.28	0.0001
B-Amt. of TiH ₂	2.14	1	2.14	56.87	0.0001
Residual	0.38	10	0.038		
Total	4.30	12			

final pore diameter. The Lack of Fit is sufficiently low, with a value of 3.24, validating the model. The precision index value of the surface response linear model of average pore diameter is given in Table 4.15. The "Pred R-Squared" of 0.9124 is in reasonable agreement with the "Adj R-Squared" of 0.8949. "Adeq Precision" ratio of 24.505 indicates an adequate signal and suggest that the model can be used to navigate the design space. Similarly, the model adequacy are investigated by the use of the diagnostic tools available with the software and found to be satisfactory.

The perturbation plot for the average pore diameter showing the sensitivity of the process variable (Fig. 4.12) and the corresponding response surface linear model in graphical form is shown in Fig. 4.13. The similar slope of the two curves in the perturbation plot indicates that the influence of the amount of TiH₂ and the holding time are similar in deciding the final pore diameter. The 2D plot drawn with actual values shows the variation of average pore diameter with the holding time as well as with the

Table 4.15. Precision index values of the surface response linear model for the average pore diameter using CCD.

Std. Dev.	0.19	R-Squared	0.9124
Mean	3.13	Adj R-Squared	0.8949
C.V. %	6.19	Pred R-Squared	0.8185
PRESS	0.78	Adeq Precision	24.505

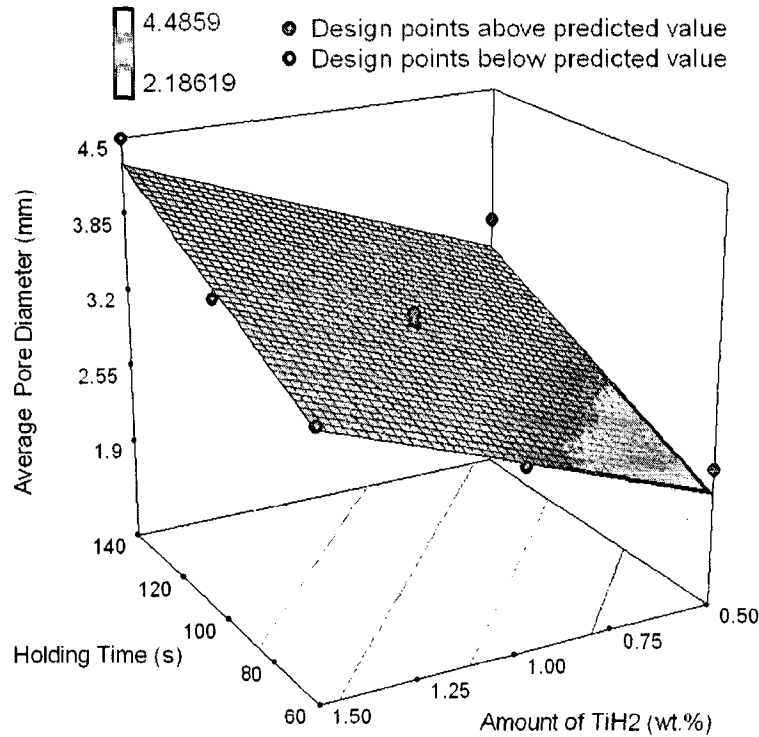


Fig. 4.13. Response surfaces linear model in graphical form for the structural parameter the average pore diameter using CCD.

amount of TiH_2 (Fig. 4.14). It can be noted; that as the holding time increases the time dependant cell growth due to decomposition of TiH_2 as well as the coalescence of cell wall due to gravity induced drainage leading to collapse of cell walls, resulting in larger pore diameter.

Similarly, as the amount of TiH_2 increases, the agglomeration of particle may also increase the pore size. The final pore diameter and the relative density are determined by the growth rate of the pore and stability of the foam (Yang and Nakae, 2000). Song and Nutt (2007) conclude that the expansion rate is determined by the size of the blowing agent powder granules. Similarly agglomeration of TiH_2 powder can also increase the pore size, as shown in Fig. 4.14. However, for the same amount of TiH_2 addition, the pore diameter increases with holding time mainly due to the collapse of the cell walls leading to larger cell structure (see Fig. 4.15). Recently, Yang et al (2007) have reported that the stirring time after TiH_2 addition decides the initial size of the pore and the final pore size depends on the holding time. In short, it can be concluded that the original size of the pore is determined by the stirring time and the expansion rate is determined by the size of

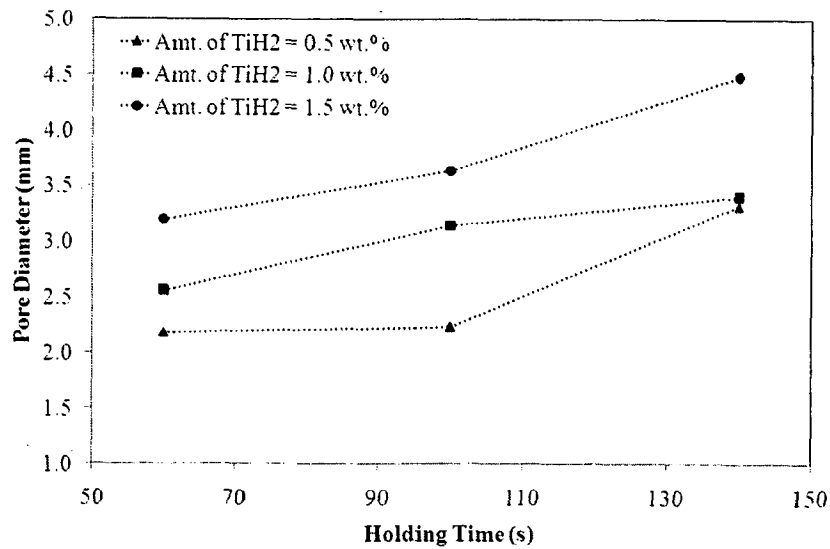


Fig. 4.14. Plot showing the variation of average pore diameter of foam structure with holding time and the amount of TiH₂ addition.

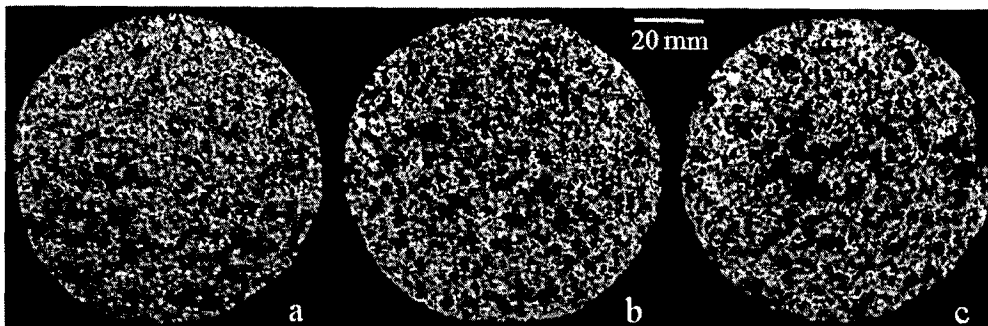


Fig 4.15. The effect of holding time (a) 60s, (b) 100s and (c) 140s on average pore diameter of the foam when other parameters are maintained constant. 1.0 wt.% TiH₂, 1.0 wt.% Ca and 10 minutes stirring time after Ca addition.

the blowing agent powder and the duration allowed for expansion. However, the stirring duration after TiH₂ addition is maintained constant in the present work. The empirical equation from the response surface linear model obtained for the average pore diameter in coded factors (equation 4.3) and actual factors (equation 4.4) are given below:

$$\text{Average pore diameter} = 3.13 + 0.54 A + 0.60 B \quad (4.3)$$

$$\text{Average pore diameter (mm)} = 0.5785 + 0.0136 A + 1.1944 B \pm e_r \quad (4.4)$$

where A is the holding time (s), B is the amount of TiH₂ added (wt.%) and e_r is the experimental error. It can be observed from the coded equation 4.3 that the holding time and the amount of TiH₂ addition had equal influence on the final pore diameter of the foam. The perturbation chart for the pore diameter (Fig. 4.12) also shows that the influence of both the process parameters is linear throughout the designed process range.

Table 4.16. ANOVA results tabulated for response surface linear model for cell aspect ratio using CCD.

Source	Sum of Squares	df	Mean Square	F value	p-value Prob > F
Model	0.046	5	9.270×10^{-3}	13.49	0.0018
A-Holding time	0.032	1	0.032	46.59	0.0002
B-Amt. of TiH ₂	6.828×10^{-3}	1	6.828×10^{-3}	9.90	0.0162
AB	4.830×10^{-5}	1	4.830×10^{-5}	0.070	0.7989
A ²	5.796×10^{-5}	1	5.796×10^{-5}	0.084	0.7803
B ²	5.776×10^{-3}	1	5.776×10^{-3}	8.37	0.0232
Residual	4.829×10^{-3}	7	6.898×10^{-4}		
Total	0.051	12			

Table 4.17. Precision index values of the surface response linear model for the cell aspect ratio using CCD.

Std. Dev.	0.026	R-Squared	0.9057
Mean	1.10	Adj R-Squared	0.8383
C.V. %	2.39	Pred R-Squared	0.3278
PRESS	0.034	Adeq Precision	12.462

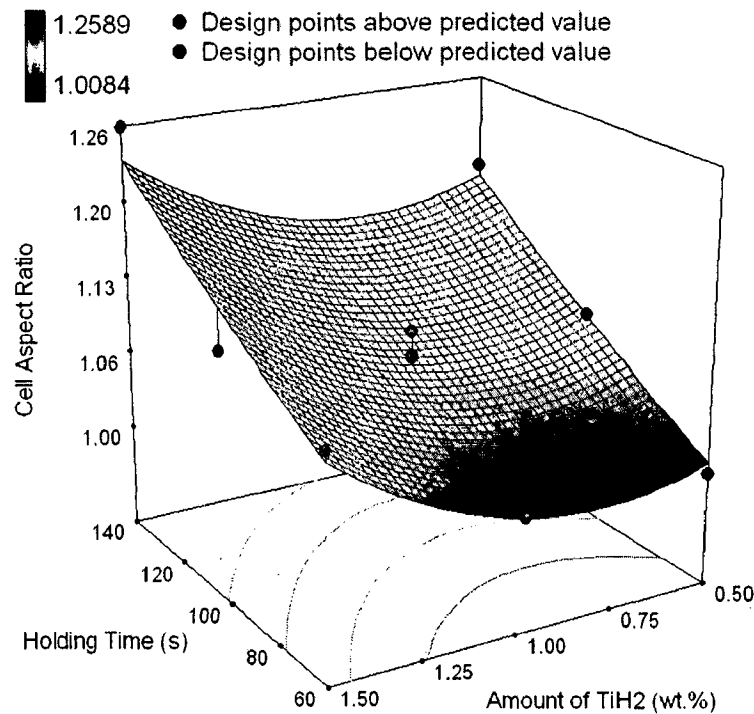


Fig. 4.16. Response surfaces quadratic model in graphical form for the structural parameter cell aspect ratio.

4.2.2.3. Influence of major Process Parameters on Cell Aspect Ratio

The ANOVA table for the cell aspect ratio model is given in Table 4.16. The ANOVA results for the cell aspect ratio model by surface response gives a model F-value of 13.44 and the corresponding p-value of 0.0018 of the model suggests that there is only 0.18% chance that this large F-value could have occurred due to noise. The precision index value the "Pred R-Squared" of 0.3278 is not as close to the "Adj R-Squared" of 0.8383 as one might normally expect. However, "Adeq Precision" ratio of 12.462 suggest that the model can be used eventhough the model adequacy is not as significant as the other two models. The precision index value of the model for cell aspect ratio is given in Table 4.17.

The cell aspect ratio model by the surface response methodology is shown in Fig. 4.16 and the corresponding perturbation plot in Fig. 4.17. It can be seen that the influence of the holding time for foaming is more on cell aspect ratio in comparison with the amount of TiH₂ addition. Additionally, it can be seen that the influence of the amount of TiH₂ addition on cell aspect ratio is insignificant below 1.0 wt.%. This is because, initially, during foaming the cells are of spherical shape and they begin to grow with time.

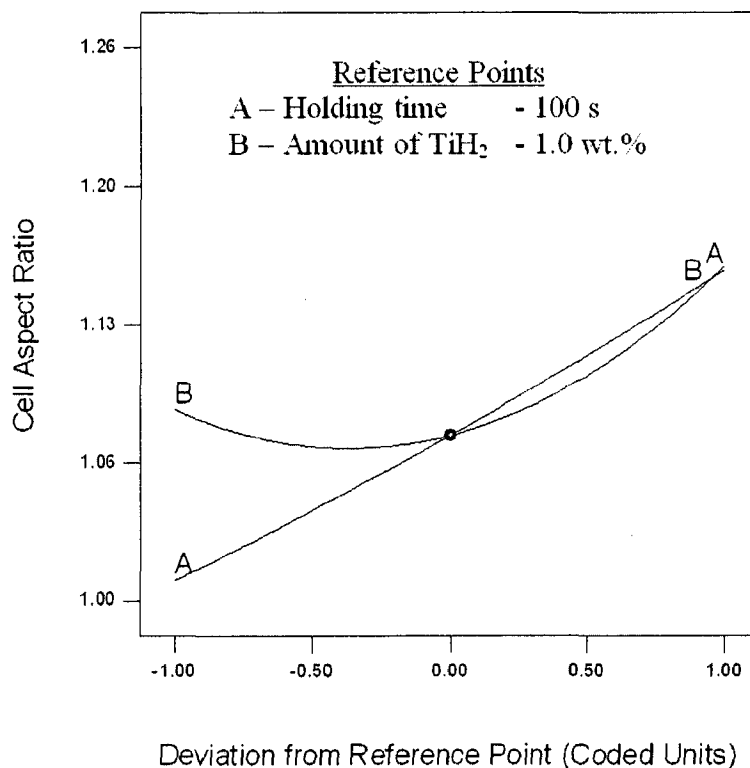


Fig. 4.17. Perturbation plot of response surface quadratic model for the cell aspect ratio model.

Only on the latter stage, due to drainage, some cell walls collapse and due to additional load on the remaining cell edges, they buckle leading to increased cell aspect ratio transverse to the foaming direction. These effects are prominent only when the amount of TiH_2 is greater than 1.0 wt.%, where the size of the pore is also larger. However, the holding time had the direct influence on the cell aspect ratio (Fig 4.16) throughout the experimental range. Also, it can be observed from the experiments that the cell aspect ratio increases when the amount of TiH_2 is more than 1.0 wt.%. By looking at the dependency of the process parameters on the cell aspect ratio and relative density, it can be concluded that for achieving uniform spherical cell structure it is desirable not to exceed 1.0 wt.% TiH_2 addition. The empirical equation from the surface response quadratic model for the cell aspect ratio in coded factors (equation 4.5) and actual factors (equation 4.6) are given below:

$$\begin{aligned} \text{Cell aspect ratio} = & 1.08 + 0.073 A - 0.034 B \\ & - 3.475 \times 10^{-3} AB + 4.581 \times 10^{-3} A^2 + 0.046 B^2 \end{aligned} \quad (4.5)$$

$$\begin{aligned} \text{Cell aspect ratio} = & 1.0217 + 1.4307 \times 10^{-3} A - 0.2810 B \\ & - 1.7375 \times 10^{-4} AB + 2.8632 \times 10^{-6} A^2 + 0.1829 B^2 \pm e_r \end{aligned} \quad (4.6)$$

The coded factor equation (4.5) indicates that the influence of holding time is more on the cell aspect ratio.

4.3. Microstructural Analysis

The properties of the closed cell metal foam depend on structural aspects such as the relative density, pore size distribution and cell wall thickness. There are some processing challenges to produce specified foam structure, because, foam evolution is a stochastic phenomena due to irreversible processes such as continuous drainage leading to cell wall collapse. Since equilibrium will not be reached it is desirable to retard the irreversible processes to achieve better control over the foam structure. It is common practice to introduce a solid second phase either in-situ or ex-situ to enhance stability by increasing the melt viscosity (Haibel et al., 2006; Asavavisithchai and Kennedy, 2006; Banhart, 2006; Wubben and Odenbach, 2005). As mentioned in section 4.2 and shown in Fig. 4.1, the 6061 aluminum alloy without the addition of copper did not produce foam by degassing TiH_2 . The microstructure of 6061 aluminum alloy (as received), shown in Fig. 4.2(a) does not contain any network structure. However, after the addition of 4 wt.% copper, stable foam structures could be produced. The secondary and backscattered SEM

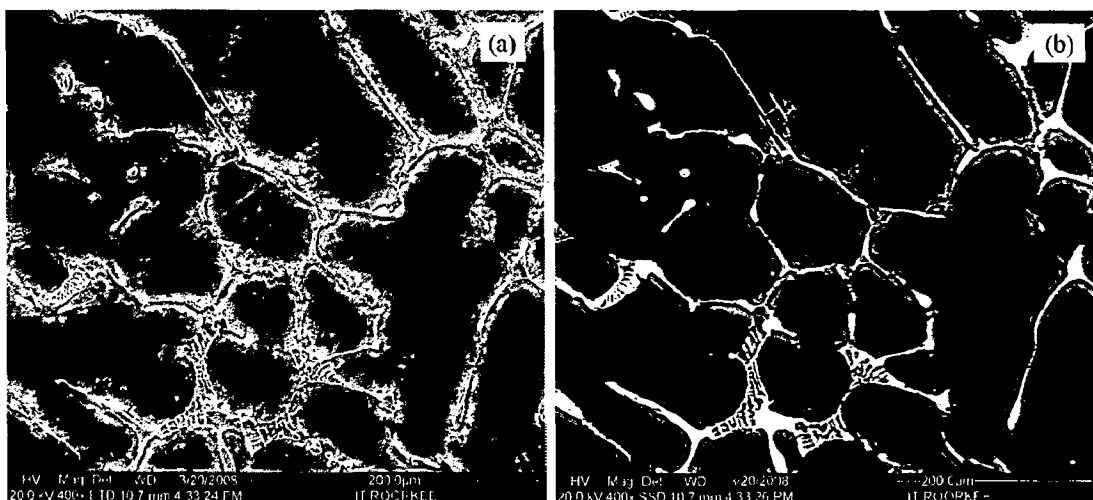


Fig. 4.18. (a) Secondary and (b) backscattered SEM image of 6061 aluminum alloy + 4 wt.% copper + 1 wt.% calcium showing Al_2Cu intermetallic network.



Fig. 4.19. Elemental line analysis of 6061 aluminum alloy + 4 wt.% Cu + 1 wt.% Ca in as cast condition.

image of the 6061 aluminum alloy after addition of 4 wt.% copper and 1.0 wt.% calcium is shown in Fig. 4.18. The aluminum formed coarse dendrite arms with fine Al_2Cu lamellae distributed throughout. The EDS analysis was used to identify the presence of Al_2Cu lamellae and Al_2Ca particles. The line analysis of the same is shown in Fig 4.19. These network structures contribute to the formation of bulky intermetallics when TiH_2 is added. The presence of Al_2Cu as lamellae is expected to help in the stabilization of the foam.

4.3.1. X-ray Diffraction Analysis

A typical X-ray powder diffraction pattern of aluminum foam synthesized in the present work is shown in Fig. 4.20. The peaks in the pattern belong to the primary solid solution of aluminum. The other peaks are of very low intensity suggesting their small volume fraction and/or fine size distribution. To identify the particles present in the alloy, the aluminum matrix is selectively leached by weak hydrochloric acid. While the intended purpose is to selectively dissolve the primary aluminum, it is not possible to

avoid partial oxidation of the residual particles. The fraction of extracted particle is about 14 % by weight. Fig. 4.21 shows the X-ray diffraction pattern analysis of the extracted particles identified as Al_2Ca , Al_2CuO_4 , TiAl_3 , and Al_2O_3 . The Al_2Cu network particles formed were probably oxidized while leaching out the aluminum metal and it appears as Al_2CuO_4 in the XRD diffraction pattern. However the $\text{Al}_{20}\text{CaTi}_2$ intermetallic which appear as bulky precipitates and identified by EDS analysis did not showed up in XRD analysis after leaching.

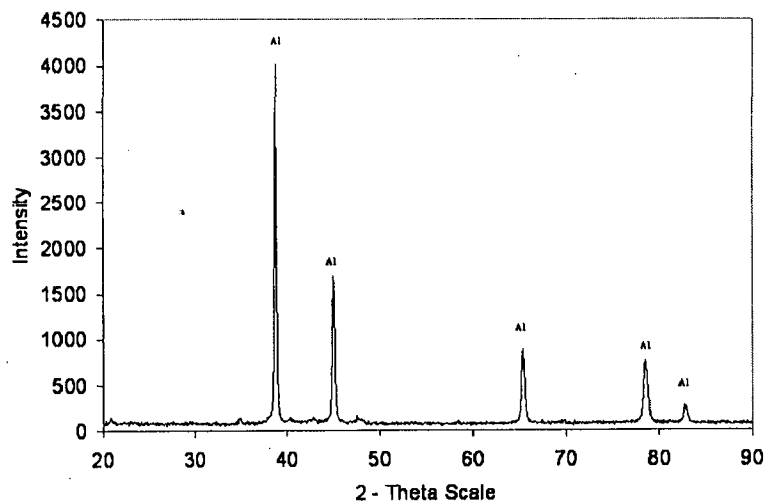


Fig. 4.20. Powder XRD pattern of the synthesized foam.

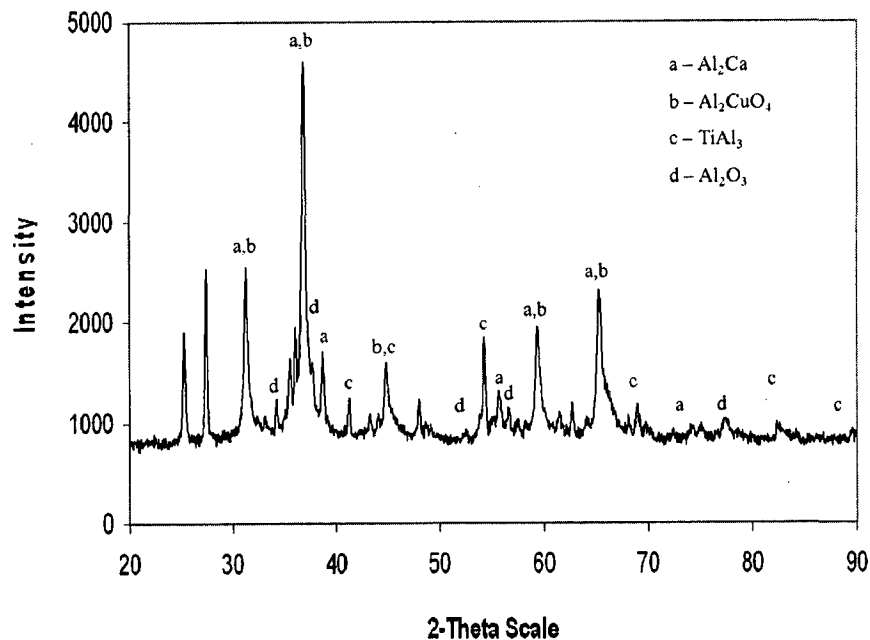


Fig. 4.21. Powder XRD pattern of the extracted particles from the foam after leaching with dilute hydrochloric acid.

The TiH_2 and calcium added to the melt have reacted and formed intermetallics, and contributed to the value addition by alloying. The fact that all these peaks show broadening points to their fine size in the sub-micron range. The presence of such fine intragranular dispersoids is expected to increase the apparent viscosity of the melt and promote strengthening of the alloy. Moreover, the coarser particles will contribute to stabilizing the liquid foam (Markaki and Clyne, 2001; Babcsan et al., 2004).

4.3.2. Electron Microscopy Analysis

The backscattered SEM micrograph of the unetched cell wall of the aluminum foam is shown in Fig. 4.22 along with EDS analysis at various locations. It is to be noted that the EDS is used as a qualitative tool to locate the phases and elements in the microstructure for identification in conjunction with X-ray analysis. The EDS cannot be used as a quantitative tool as microstructural features are often finer than the $\sim 1 \mu\text{m}^3$ from which the X-ray signals are emitted. The microstructural analysis reveals that the intermetallic particles are located within the cell wall whereas the oxides are present at the extremities. The thin lamellar structure shown as (a) in Fig. 4.22 is Al_2Cu intermetallic. Al_2Cu is important to stabilize the foam structure, since the base aluminum alloy 6061 without copper addition did not produce stable foam (See Fig. 4.2(a)). Al_2O_3 particles shown as (b) in Fig. 4.22 are only confined to the pore surface and not inside the cell wall matrix. $\text{Al}_{20}\text{CaTi}_2$ shown as (c) in Fig 4.22 is identified as coarse precipitates distributed throughout the structure.

In earlier experiments stainless steel stirrer with alumina coating was used in place of graphite stirrer. These experiments showed the presence of iron intermetallic in spite of the protective alumina paste coating on the stirrer. The iron diffused into the aluminum forming platelets of $\text{Al}_{13}\text{Fe}_4$ intermetallic with high aspect ratio (Fig. 4.23). Along with the iron intermetallic, the presence of Al_2Cu network and $\text{Al}_{20}\text{CaTi}_2$ particles are also seen in this microstructure.

The network structure of Al_2Cu is seen prominently within the cell walls even after foaming by the addition of TiH_2 (Fig. 4.22). Similar network structure is also seen even before degassing the melt by TiH_2 (Figures 4.18 and 4.19). Al_2Cu particles appear like bright thin platelets. Moreover, the other intermetallic particle $\text{Al}_{20}\text{CaTi}_2$ is seen as a blocky precipitate dispersed sparsely inside the cell walls. However, the intermetallics

$\text{Al}_{13}\text{Fe}_4$ formed while using alumina coated stainless steel stirrer is brighter and are like elongated platelets seated across the cell walls. They help in retarding the sapping of liquid melts to the plateau edge from the cell walls/faces leading to drainage and cell wall collapse.

The elemental mapping of the cell wall microstructure of the foam made by using graphite stirrer is shown in Fig. 4.24. A comparison of the calcium and titanium map clearly shows that the blocky precipitates are $\text{Al}_{20}\text{CaTi}_2$ intermetallic. The phase which is richer in Ca (with no Ti) is identified as Al_2Ca which is also recorded in the X-ray diffraction of the extracted particles (Fig 4.21). Oxygen signals are picked up primarily from the surface, but there are a few cavities within the cell which have an oxide skin.

The elemental map of the cell wall microstructure of the foam made with stainless steel stirrer is shown in Fig. 4.25. In addition to the phases identified in the foam prepared with graphite stirrer, coarse $\text{Al}_{13}\text{Fe}_4$ platelet with high aspect ratio is the significant addition to the microstructure. Similarly, the EDS line mapping of elements such as titanium, calcium, copper and oxygen is done and is shown in Fig. 4.26. Taking these lines together, the results correspond to the phases identified in the area map earlier. From these analyses, it is clear that the oxygen is present only on the cell wall surface and not inside the cell walls and intermetallics are confined to within the cell wall. The presences of micropores on the cell walls are also seen in these micrographs.

TEM specimens were prepared from the foams prepared using graphite stirrer. The bright field images in Fig 4.27 provide information at a length scale more than two orders of magnitude lower than that of the SEM images. The particular image refers to the structure of the aluminum cell wall material between the intermetallic particles seen in the SEM micrographs. The TEM micrograph clearly shows the fine aluminum grain substructure on the scale of 50 nm. The diffraction pattern of the region confirms the multicrystalline nature on a fine scale. The SEM micrograph revealed the presence of 30 μm sized particles within the cell wall material. On the other hand, the TEM micrograph showed the presence of 200 nm sized single-crystalline intermetallic particles embedded in the aluminum matrix between the coarse intermetallic particles. Such particles that are present within the aluminum grain are expected to enhance the strength of the cell wall material.

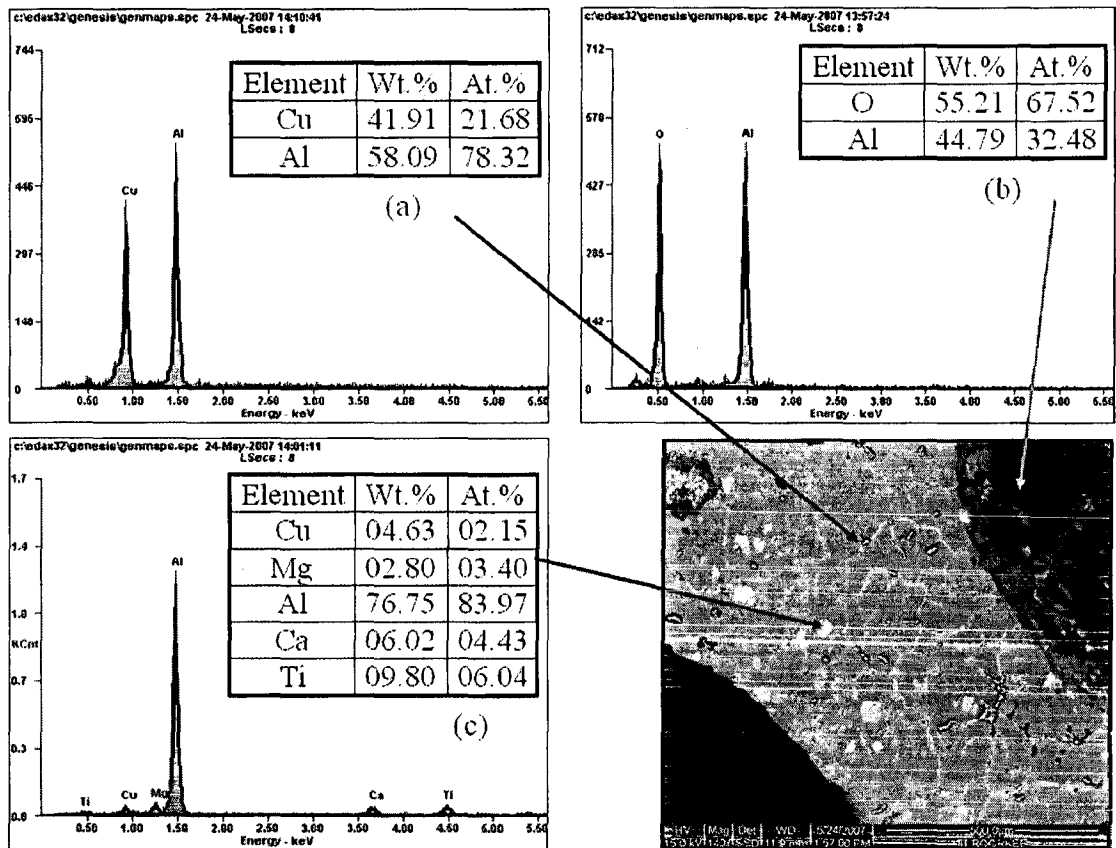


Fig. 4.22. SEM microstructure of the foam cell wall along with EDS analysis at different points indicated in the microstructure.

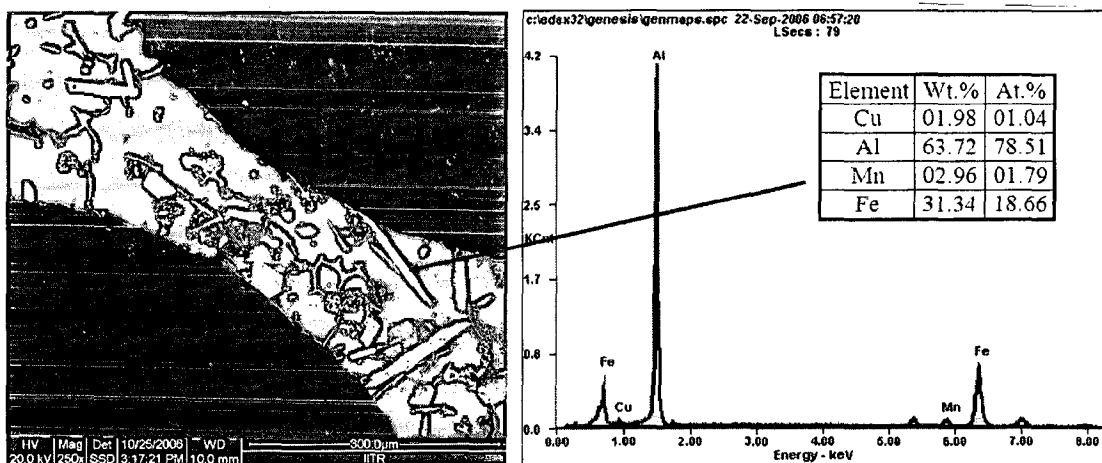


Fig. 4.23. SEM microstructure along with EDS showing the presence of iron intermetallics for some sample made by using stainless steel stirrer.

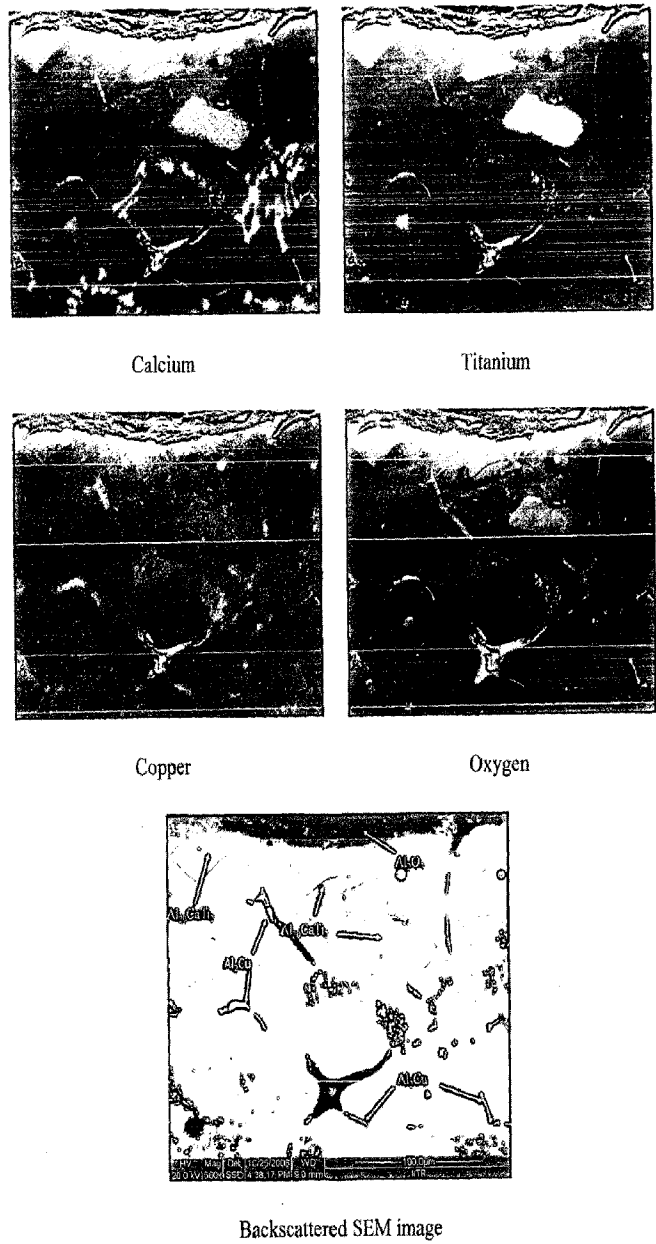


Fig. 4.24. SEM micrograph and EDS mapping for the various elements present on the cell wall of the foam made with graphite stirrer.



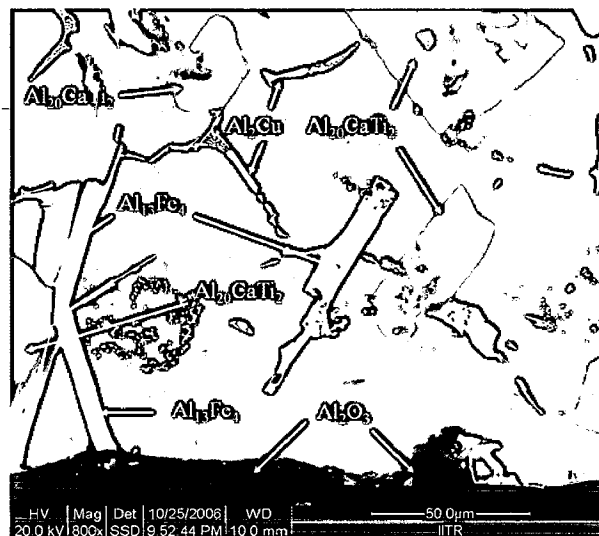
Calcium

Titanium



Copper

Iron



Backscattered SEM image

Fig. 4.25. SEM micrograph and EDS mapping for the various elements present on the cell wall of the foam made with stainless steel stirrer.

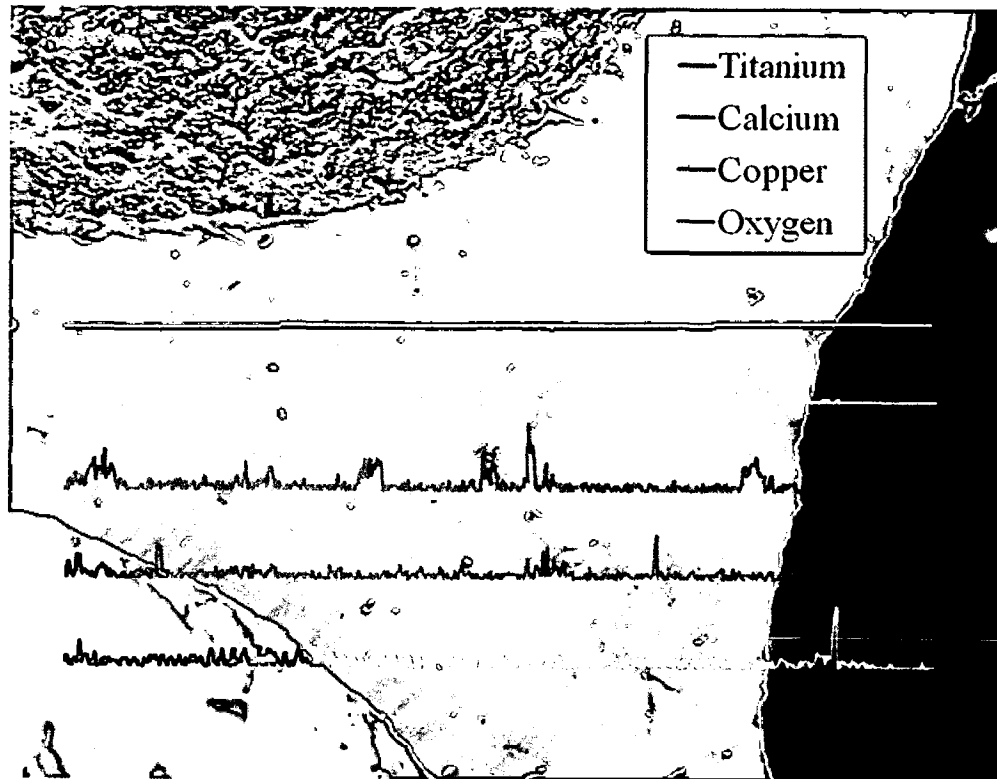


Fig. 4.26. SEM micrograph and the EDS line mapping (white line on the SEM micrograph) for the various elements present on the cell wall of the foam.

4.3.3. Inference from Microstructural Studies

Stabilization of the foam in the aluminum alloy melt is probably the single most important criteria in achieving optimum mechanical properties in metallic foam structures. Stabilization, in this case, refers to the extension of the lifetimes of the individual gas bubbles (or prevention of the cell wall collapse) in the liquid state and during solidification. The need for foam stabilization is to achieve a reasonably fine pore size with a narrow size distribution. The control of melt viscosity is known to have a bearing on the final pore size and the density of the foam (Babcsan et al., 2003). In gas injection melt route, metal matrix composite processing techniques of dispersing SiC / Al₂O₃ / MgO have been incorporated in an attempt to stabilize the gas bubbles (Ip et al., 1998; Deqing and Ziyuan, 2003). In melt foaming with blowing agents, calcium metal is dispersed vigorously in the melt, forming CaO, CaAl₂O₄ or even Al₄Ca, which increases the apparent melt viscosity (Babcsan et al., 2004). In the first case, where the ceramic

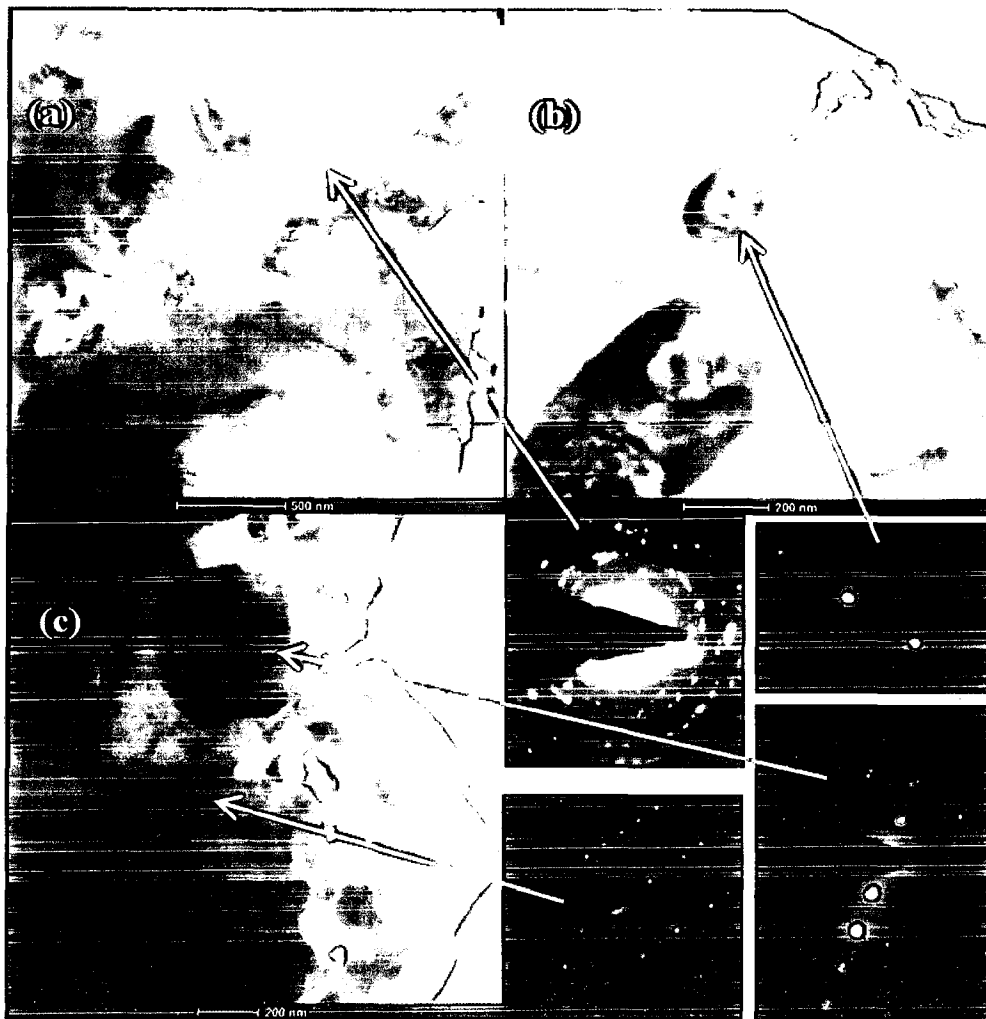


Fig 4.27. TEM bright field image: (a) cell wall material showing sub-grain structures. The diffraction pattern of the region confirms multi-crystalline nature. (b) & (c) nano sized intermetallic particle embedded in aluminum grain. SAD pattern confirms its single crystallinity.

particles are externally introduced, the problem of wetting needs to be addressed before the particles can be incorporated within the cell wall. In the second case, the morphology of the in-situ particles is such that they do not influence drainage.

The drainage of the liquid metal from the cell face to the thicker cell edge is driven by the local pressure difference caused by the difference in curvature (Fig. 4.28). Additionally, drainage along the cell edge is driven by gravity which progressively makes the foam drier (Banhart, 2006). In fact, there is a European Science Foundation initiative to carry out experiments in space to understand the drainage phenomena neglecting gravitational effects (Wubben et al., 2003). The Fig. 4.29 shows the macrograph of foam showing the changes in cell structure due to drainage and cell wall collapse. The

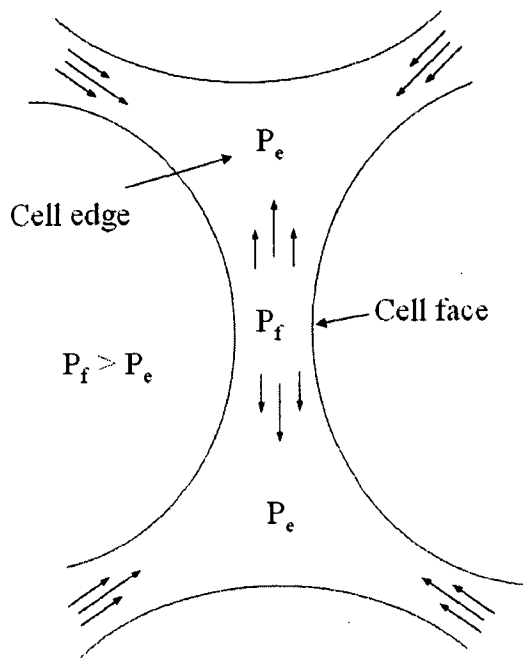


Fig. 4.28. Schematic of the pressure difference between cell face and edge causing movement of cell fluids towards the edge leading to thinning of cell faces/walls.

the foam properties. The proposed processing technique to introduce in-situ intermetallic particles such as $\text{Al}_{20}\text{CaTi}_2$ and $\text{Al}_{13}\text{Fe}_4$ of certain morphology has the scope to improve foam stability and also the mechanical properties of foams synthesized by liquid metallurgy route. The suggested solution to the problem is to retard drainage and strengthen the cell wall such that cell wall collapse is further delayed. The twin objective is met by introducing in-situ high melting point intermetallics with favourable morphology within the cell walls. The intermetallics have the added advantage of enhancing the mechanical property of the foam particularly when they are of a finer scale.

macrostructural cross-section of a mature foam in Fig. 4.29 shows the progressive thinning of the cell wall driven by local drainage. Initially a fairly thick cell wall develops a curvature which progressively drives metal away from the cell face towards the cell edge leading to progressive thinning and to eventual collapse. The collapsed cell wall co-joins the neighbouring cells into a whole. If the collapse occurs at a later stage such that there is not enough time for readjustment, the co-joined cells display a pronounced aspect ratio.

Improving the stability of the liquid foam allows better control of the foam structure which in turn influences

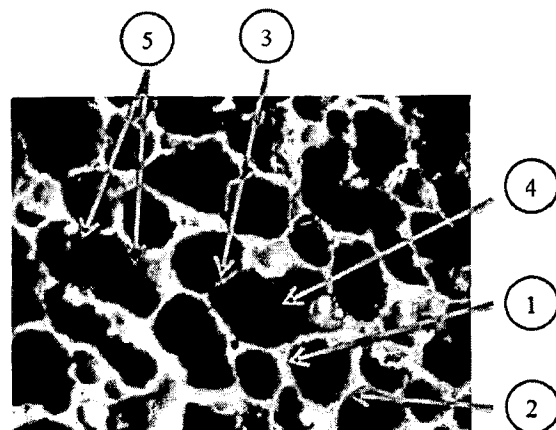


Fig. 4.29. Macrograph of foam showing cell walls in various stages (1 to 5) of thinning before collapse leading to coalescence.

4.4. Mechanical Property Analysis

The process variables for foaming dictate the macrostructure of final foam. The variation in macrostructure and tailoring them for the requirements are discussed in details with the results obtained in section 4.2. However, it should be noted that the structure of aluminum foam processed under different conditions, sometimes even under the “same” condition are highly variable due to the stochastic nature of the process (Song and Nutt, 2007). Therefore to avoid discrepancy in results, a minimum of five specimens are tested under quasi-static condition and two under dynamic condition for each set of experiment carried out under the designed process variables. The procedure for the calculation of mechanical properties is given in the previous chapter in section 3.4.7. It should be noted that the process variables decide the morphological and microstructural features of the foam, which are in turn are responsible for the mechanical properties. In the initial part, foams made with stainless steel and graphite stirrer are compared. Later, to maintain consistency, foams made by using the graphite stirrer are only considered for all the mechanical property analysis in such a manner that the microstructural variations are partially negated.

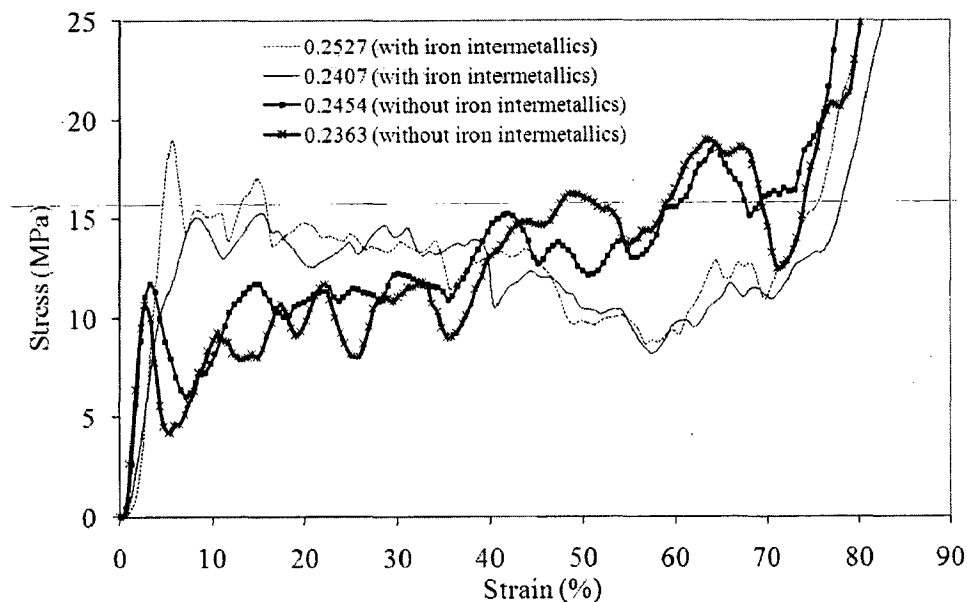


Fig. 4.30. Stress-strain plot of Al foam with and without iron intermetallic in the cell wall showing different plateau stress behaviour (The numbers in the legends indicates the relative density of the specimen).

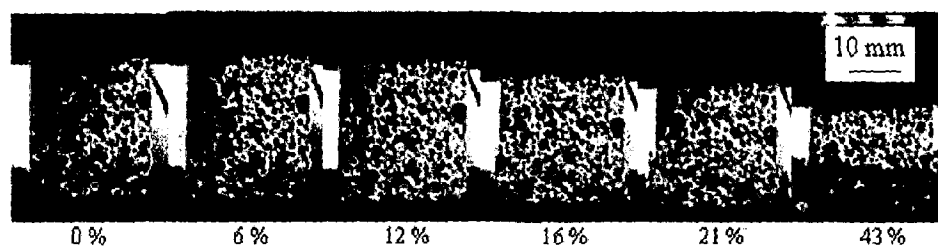


Fig.4.31. Sequence of photograph at different strains during the compression test of Al foam.

4.4.1. Quasi-Static Compression Test

Two sets of foams were produced with graphite stirrer and stainless steel stirrer, respectively. The microstructure of the cell wall material of the two sets of foams is different and lend to different compression behaviour. In fact, the samples made using the graphite stirrer had $Al_{20}CaTi_2$, Al_2Cu and Al_2Ca intermetallic particles, whereas the samples prepared with the stainless steel stirrer had $Al_{13}Fe_4$ in addition to the other intermetallic particles dispersed within the cell wall. The foams having $Al_{13}Fe_4$ showed better stability in the cell structure with less cell wall collapse and have higher plateau strength. However, the presence of $Al_{13}Fe_4$ makes the foam slightly more brittle. The quasi-static stress-strain curve is also different for the foam containing $Al_{13}Fe_4$ intermetallic particle (Fig. 4.30). One such sample during quasi-static compression test is shown in Fig. 4.31 as a series of photograph at progressive strain values. For similar density foams, the sample containing iron intermetallic particle reaches a higher stress at the beginning of the plateau region. Subsequently, there is a gradual decrease in the stress levels in the plateau region, whereas the sample without iron intermetallic particle shows a gradual increase in stress values in the plateau region. This phenomenon of decreasing stress level in the plateau region is reflective of the brittle nature of the cell wall due to the presence of iron intermetallic within the cell wall matrix (Kurauchi et al., 1984). In fact the foam was continuously disintegrating during the compression test such that it could not bear additional load. However, all compressive property data of foam samples used in the present work were made by graphite stirrer, such that there was no iron intermetallic present.

Fig. 4.32 shows the typical stress-strain diagram of the closed-cell aluminum foam of various relative densities carried out at a strain rate of $1 \times 10^{-3} \text{ s}^{-1}$. It is observed that the relative density of the foam increases the plateau stress value and at the same time the

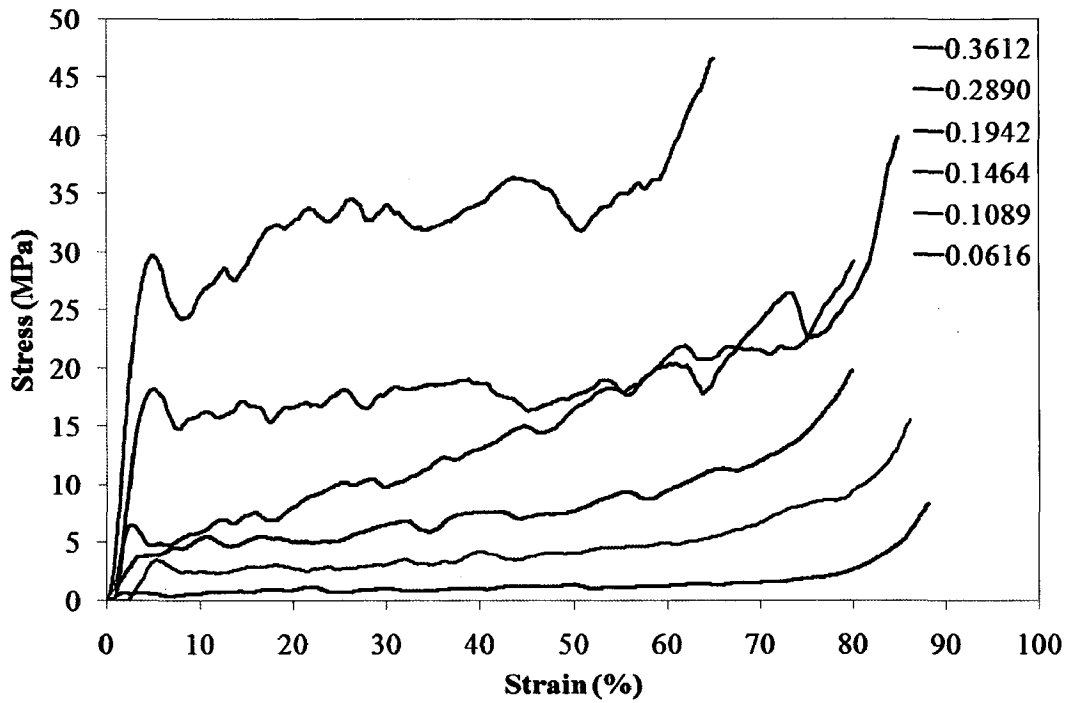


Fig. 4.32. Stress-strain plot of closed-cell aluminum foam specimens showing increases plateau stress and reduced densification strain for samples of increasing relative density (The number in the label indicates relative density).

densification strain of the foam decreases. The evaluated mechanical properties of all foam specimens tested under quasi-static condition are arranged in ascending order with respect to the relative density and are listed in Table 4.18.

4.4.1.1. Plateau Stress

The equation for the plateau stress calculation by assuming regular closed-cell foam structure suggested by Gibson and Ashby is

$$\frac{\sigma_{pl}^*}{\sigma_{ys}} = 0.3\phi^{3/2}\left(\frac{\rho^*}{\rho_s}\right)^{3/2} + (1-\phi)\left(\frac{\rho^*}{\rho_s}\right) \quad (4.7)$$

where, ϕ is the fraction of solid contained in the cell edges, ρ^* is the density of foam, ρ_s is the density of the cell wall material, σ_{pl}^* is the plateau stress of the foam and σ_{ys} is the yield stress of the cell wall material, taken as 48 MPa. The first term in the equation, $0.3\phi^{3/2}\left(\frac{\rho^*}{\rho_s}\right)^{3/2}$, describes the contribution of cell edge bending and the other term,

$(1-\varphi)\left(\frac{\rho^*}{\rho_s}\right)$, describes the effect due to cell face stretching. The value of φ for each foam specimen is evaluated according to the equation (4.7).

Gibson and Ashby model can be used to predict the plateau stress and Young's modulus of the foam structure based on the equations (4.7) and (4.8), respectively. The experimental results obtained in the present work along with the Gibson and Ashby model prediction for plateau stress, by considering the yield stress of base material (σ_{ys}) as 48 MPa is shown in Fig. 4.33. The disparity in Gibson and Ashby model prediction can be related to the difficulties and uncertainty in determining the value of φ , and the mechanical properties of the cell wall material. The determination of cell wall mechanical property is difficult due to presence of micropores and intermetallics in the cell wall. Moreover, one would expect the properties of the cell wall to be better than the base alloy due to alloying additives and intermetallic particles present in the micron and nano scale.

Gibson and Ashby analytical models have not taken into consideration the cell size effects. From Fig. 4.33, it is seen that for lower relative density the model predictions of plateau stress is fairly good, which may be due to better determination of φ values in that region. However, when the relative density of foam is high, say above 20 %, the

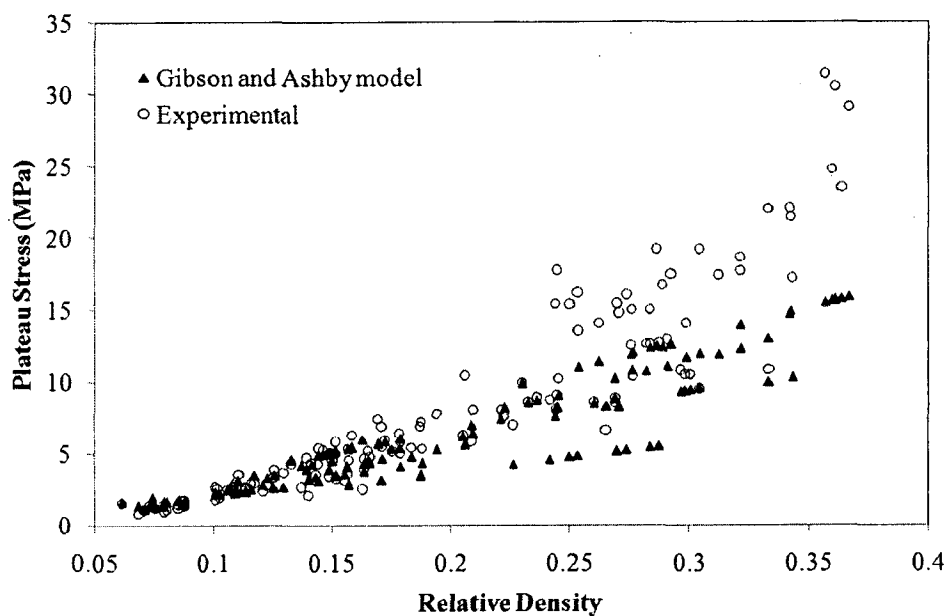


Fig. 4.33. Comparison of the experimental plateau stress values with the Gibson and Ashby model with respect to the corresponding relative densities.

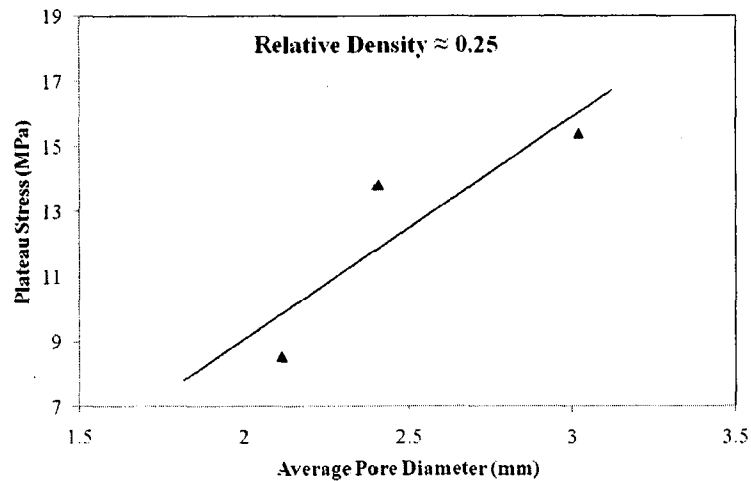


Fig. 4.34. Plateau stress increases with pore diameter for a constant relative density of 0.25 as shown by the trend line.

determination of ϕ is complicated by the fact that there is no distinction between cell edges and face. Moreover, the experimental results show that the plateau stress increases non-linearly with respect to relative density, increasing rapidly at higher relative density, whereas the Gibson and Ashby model prediction is linear in nature. Furthermore, it can be noted that the foam with similar relative density may have different plateau stress. For instance, samples with relative density of 0.25 with different pore diameter are tested and compared and shown in Fig. 4.34. The plateau stress increases with pore diameter which may be explained on the basis of increasing cell wall thickness (Edwin and Daniel, 2008a; Bin et al., 2007; Schwingel et al., 2007). The cell size effects is an important feature which is not taken into account in the Gibson and Ashby model as the model is derived on the basis of a regular cell structure.

The plateau stress determines the energy absorption capacity of the foam as it is at this stress level that energy absorption takes place. For this reason it is necessary to compare the plateau stress values of the foam with those reported in the literature. Care needs to be taken to compare similar foam, i.e. foams processed by similar route having similar relative density. Olurin et al. (2000) have reported plateau stress values of 1.39 MPa, 1.65 MPa and 2.46 MPa for relative densities of 0.08, 0.11 and 0.15, respectively. The foams processed in the present work have relative densities of 1.2 MPa, 2.8 MPa and 4.47 MPa, respectively, for same relative densities which are comparatively more attractive values. Mukai et al. (1999) have reported plateau stress values of 1.4 MPa and

1.84 MPa for relative densities of 0.074 and 0.094, respectively. For comparable relative densities we have reported plateau stress values of 1.33 and 2.01 MPa, respectively. Here again the values are comparable with the results from the present work showing a stronger dependence on density. Ramamurty and Paul (2004) have procured Alporas foam from Shinko wire company Ltd., Japan and report plateau stress values in the range 1.69 – 2.18 MPa for foams with relative density in the range 0.094 – 0.112, respectively. In the present work for comparable relative density, plateau stress values in the range 1.74 – 3.49 MPa is reported. Olurin et al. (2000) have also reported plateau stress of foams prepared by air injection procured from Alcan as 0.39 MPa, 3.58 MPa and 4.44 MPa for relative densities of 0.09, 0.27 and 0.33, respectively. The foams processed by TiH₂ decomposition in the present work have plateau stress values of 2.06 MPa, 11.81 MPa and 18.55 MPa, respectively which is several factors higher. McCullough et al. (1999) have reported plateau stress value of 12.7 MPa for Alulight foam of relative density 0.25 which is lower than the value of 14.6 MPa reported in the present work for comparable relative density. From the reported literature values it is clear that foams prepared by TiH₂ degassing in aluminum hold good prospect for energy absorption applications. Additionally, the better plateau stress values reported in the present work could be due to strengthening effects due to alloying and nano scale dispersion observed in the aluminum cell wall material.

4.4.1.2. Young's Modulus

The equation for the Young's modulus calculation for closed-cell foam structure suggested by Gibson and Ashby is

$$\frac{E^*}{E_s} = \phi^2 \left(\frac{\rho^*}{\rho_s} \right)^2 + (1 - \phi) \left(\frac{\rho^*}{\rho_s} \right) \quad (4.8)$$

where E^* is the Young's modulus of the foam and E_s is the Young's modulus of cell wall material, taken as 69 GPa. The two terms of equation describes the combined effect of cell edge bending and cell face stretching respectively.

The cross-head displacement of the load frame is used for the displacement calculation as it is not possible to fix the extensometer on the foam specimen. Machine compliance was found to affect the actual displacements under various loading

conditions, resulting in differences of several magnitudes between dynamic modulus values measured by the actuator and by surface-mounted deformation transducers (Daniel et al., 2004). As initially observed by Sugimura et al. (1997) and later reported by Ramamurty and Paul (2004), the loading modulus is 50% smaller than the one extracted from the unloading data. This discrepancy is due to the localized nonlinear deformation in the foam sample while loading because of the stress concentrations at the nodes of the cells. Therefore the unloading modulus is taken as twice that of the loading modulus and is considered as the Young's modulus of foam.

The experimental results of the Young's modulus of the foam and the Gibson and Ashby model prediction with respect to the relative density are shown in the Fig. 4.35 and Fig. 4.36 respectively. The Young's modulus increases with relative density and the scatter in the experimental values is more pronounced at the higher relative density.

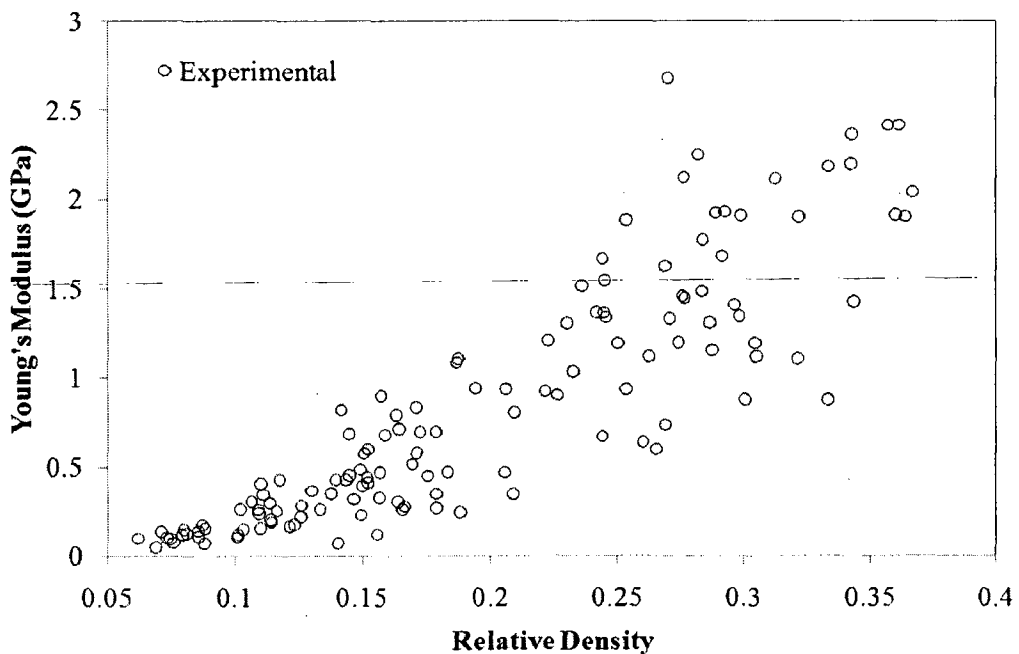


Fig. 4.35. The experimental results of the Young's modulus for the closed-cell foam with respect to the corresponding relative densities.

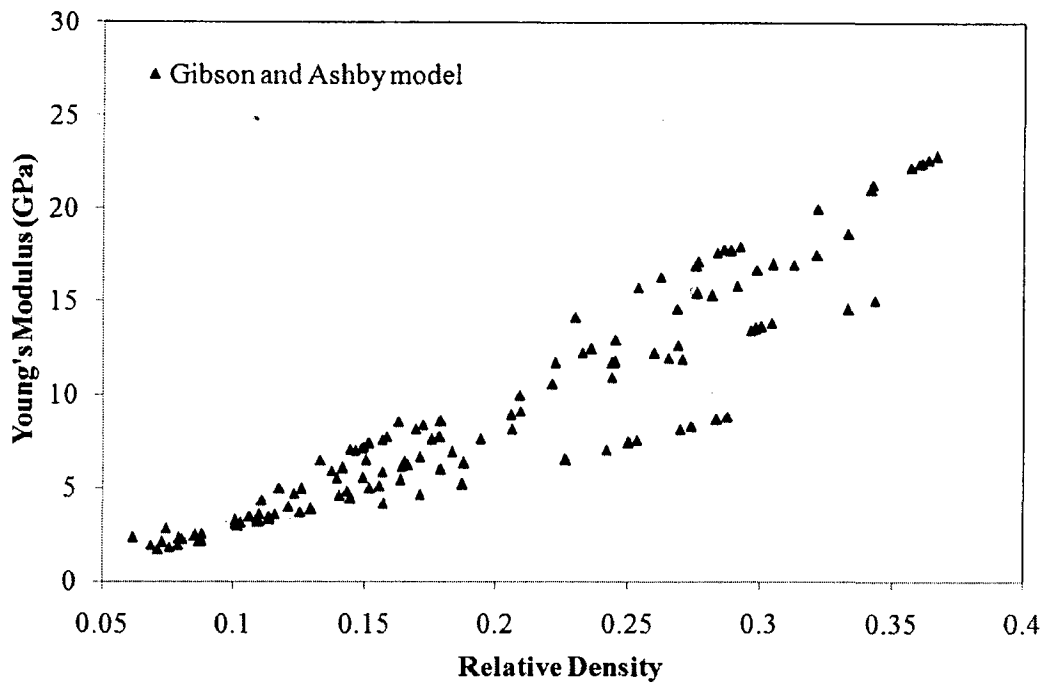


Fig. 4.36. The Gibson and Ashby model prediction for the closed-cell foam with respect to the corresponding relative densities.

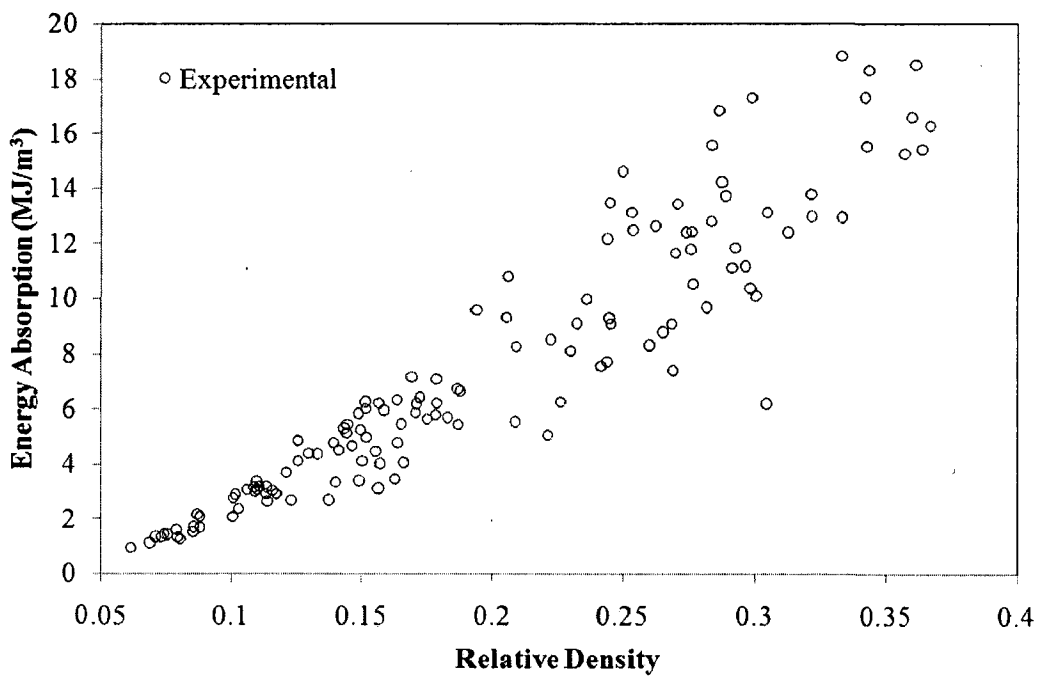


Fig. 4.37. Experimental results of energy absorption capacity up to densification strain plotted corresponding to the relative densities.

The Gibson and Ashby model estimation is higher by an order of magnitude in comparison with the experimental values. This disparity may be due to the earlier said reason such as the unsureness and inaccuracy in the estimation of cell wall material's Young's modulus for model prediction. Mondal et al. (2007) have extensively studied the analytical and experimental evaluation of modulus of porous material. They have reported that the Gibson and Ashby model equation for the estimation of modulus for closed-cell foam is significantly an overestimate. The experimental values reported in the present work are similar to those reported for Alporas foam earlier studies as well (Sugimura et al., 1997; Simone and Gibson, 1998; Andrew et al., 1999; Ramamurty and Paul, 2004; Ramamurty and Kumaran, 2004). Additionally, it should be noted that the cell size effect and to a lesser extent the cell aspect ratio effect on mechanical properties are not incorporated in the Gibson and Ashby model.

4.4.1.3. Energy Absorption

The energy absorption per unit volume determined by equation (3.1) for the corresponding relative densities is shown in Fig. 4.37. The densification strain, ϵ_d , is determined where the slope of the stress-strain curve increases steeply, accommodating more stress for small increment in strain. The densification strain of foam is inversely

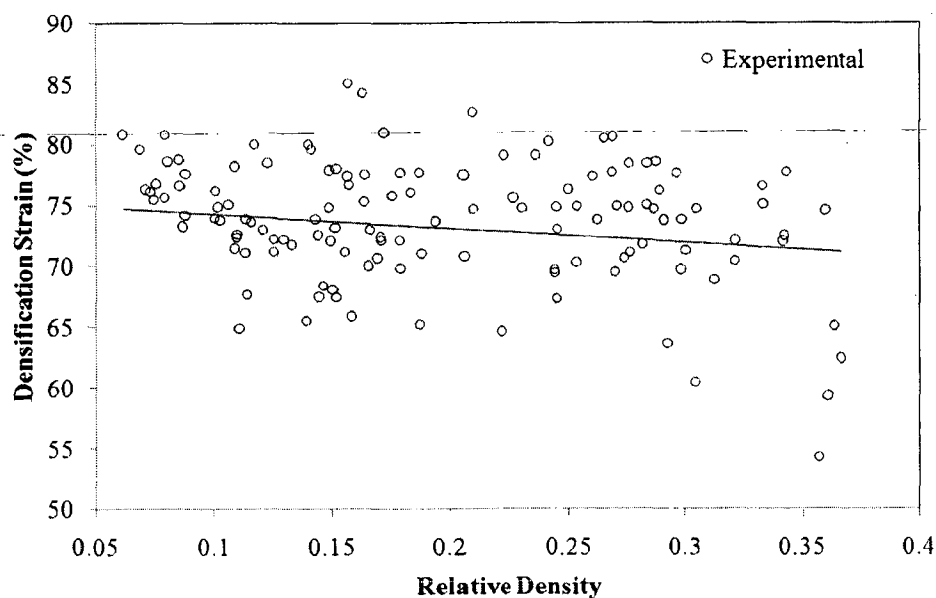


Fig. 4.38. Experimental densification strain of the foam samples showing an inverse trend with respect to relative density.

proportional to relative density and the values are plotted against the relative density and shown in Fig. 4.38.

The energy absorption is also found to have direct correlation with the foam density. The compressive stress-strain curve has a wide plateau region (Fig. 4.32); they contribute to the increase of the area under the stress-strain curve, which is usually defined as the energy absorbability of materials (Kurauchi et al., 1984). However, the plateau stress defines the stress level at which the energy absorption occurs when the material is used for the energy absorption applications.

Large compressive strains at nominally constant stress levels is required to absorb large energy at force levels appropriate for crash and blast protection system (Evans et al., 1999; Miyoshi et al., 1999; Greene et al., 2002; Ramachandra et al., 2003; Sriram et al., 2006). The results reported in this work represent comparatively the force levels appropriate for these applications. Experiments are also being carried out at higher strain rates commensurate with automobile crash and the results are reported in the next section.

The entire set of quasi-static compression data is tabulated along with the structural and mechanical property of foam in Table 4.18. Every third value in the table is used for testing/validating the developed multiple linear regression/ANN model, whereas the remaining was used for developing those models.

Table 4.18. Quasi-static compression test results of the closed-cell aluminum foam which were used for training/formulating and testing/validating the ANN and multiple linear regression models.

Sl. No.	Relative density	Aver. pore dia. mm	Cell aspect ratio	Plateau strength	Young's modulus	Energy absorption	Densification strain	ϕ
				MPa	GPa	MJ/m ³	%	
1	0.062	3.204	1.10	1.540	0.098	0.951	80.84	0.46
2	0.069	3.644	1.03	0.808	0.048	1.122	79.62	0.62
3	0.071	4.486	1.26	1.050	0.138	1.347	76.31	0.69
4	0.073	3.644	1.03	1.382	0.103	1.340	76.10	0.62
5	0.074	3.204	1.10	1.328	0.094	1.443	75.49	0.46
6	0.076	4.486	1.26	1.208	0.075	1.435	76.79	0.69
7	0.079	4.486	1.26	1.384	0.120	1.603	75.63	0.69
8	0.080	3.251	1.08	0.956	0.147	1.344	80.82	0.61
9	0.081	3.640	1.06	1.065	0.124	1.246	78.62	0.62
10	0.085	3.640	1.06	1.194	0.106	1.523	78.77	0.62
11	0.085	3.251	1.08	1.419	0.139	1.696	76.63	0.61
12	0.087	4.486	1.26	1.737	0.174	2.166	73.28	0.69
13	0.088	3.251	1.08	1.326	0.071	1.680	77.61	0.61
14	0.088	4.486	1.26	1.740	0.153	2.090	74.19	0.69
15	0.101	2.931	1.09	1.756	0.104	2.080	76.19	0.59
16	0.101	3.232	1.11	2.658	0.119	2.780	73.97	0.56
17	0.102	3.251	1.08	2.556	0.259	2.901	74.87	0.61
18	0.103	2.931	1.09	1.914	0.148	2.369	73.80	0.59
19	0.106	3.232	1.11	2.471	0.297	3.071	75.05	0.56
20	0.109	2.931	1.09	2.780	0.255	3.166	78.21	0.59
21	0.109	3.644	1.03	2.705	0.235	3.006	71.45	0.62
22	0.110	3.644	1.03	2.929	0.153	3.366	72.35	0.62
23	0.110	3.232	1.11	2.652	0.393	3.087	72.60	0.56
24	0.111	3.204	1.10	3.492	0.334	3.203	64.91	0.46
25	0.113	2.931	1.09	2.643	0.289	2.923	71.12	0.59
26	0.114	3.640	1.06	2.584	0.201	3.178	73.88	0.62

Sl. No.	Relative density	Aver. pore dia. mm	Cell aspect ratio	Plateau strength MPa	Young's modulus GPa	Energy absorption MJ/m ³	Densification strain %	ϕ
27	0.114	3.644	1.03	2.490	0.186	2.665	67.70	0.62
28	0.116	2.931	1.09	2.890	0.250	3.045	73.63	0.59
29	0.117	4.495	1.03	2.914	0.416	2.917	80.00	0.41
30	0.121	3.232	1.11	2.355	0.165	3.690	73.00	0.56
31	0.123	3.407	1.12	2.784	0.179	2.678	78.51	0.48
32	0.126	3.640	1.06	3.299	0.218	4.127	72.19	0.62
33	0.126	3.204	1.10	3.855	0.277	4.860	71.18	0.46
34	0.130	3.640	1.06	3.640	0.356	4.409	72.20	0.62
35	0.133	3.200	1.09	4.278	0.258	4.381	71.76	0.31
36	0.137	3.300	1.20	2.660	0.341	2.711	77.01	0.40
37	0.139	3.204	1.10	4.676	0.417	4.787	65.50	0.46
38	0.140	3.822	1.03	2.071	0.073	3.361	80.00	0.58
39	0.142	4.495	1.03	4.329	0.772	4.506	79.60	0.41
40	0.143	3.232	1.11	3.510	0.418	5.304	73.87	0.56
41	0.144	3.200	1.09	4.233	0.653	5.138	72.57	0.31
42	0.145	3.251	1.08	5.362	0.437	5.447	67.47	0.61
43	0.146	2.559	1.01	5.219	0.312	4.666	68.39	0.32
44	0.149	2.559	1.01	4.950	0.469	5.858	74.82	0.32
45	0.149	2.968	1.02	3.391	0.225	3.411	77.89	0.50
46	0.150	2.559	1.01	5.067	0.382	5.249	72.09	0.32
47	0.150	3.300	1.20	4.471	0.551	4.119	68.08	0.40
48	0.152	3.200	1.09	4.984	0.428	6.277	73.17	0.31
49	0.152	3.200	1.09	5.839	0.573	6.032	67.41	0.31
50	0.152	3.822	1.03	3.231	0.397	4.981	78.00	0.58
51	0.156	3.822	1.03	3.106	0.121	4.478	71.20	0.58
52	0.157	2.968	1.022	3.57	0.320	3.137	77.41	0.50
53	0.157	4.440	1.071	5.34	0.455	6.227	85.00	0.32
54	0.157	2.690	1.007	4.49	0.843	4.023	76.70	0.69

Sl. No.	Relative density	Aver. pore dia. mm	Cell aspect ratio	Plateau strength MPa	Young's modulus GPa	Energy absorption MJ/m ³	Densification strain %	ϕ
55	0.159	3.200	1.087	6.28	0.647	5.964	65.89	0.31
56	0.163	4.286	1.019	2.51	0.748	3.460	84.20	0.25
57	0.164	3.822	1.032	3.88	0.296	6.333	75.30	0.58
58	0.164	2.968	1.022	4.62	0.677	4.795	77.54	0.50
59	0.166	3.407	1.120	5.21	0.257	5.460	70.03	0.48
60	0.166	2.968	1.022	4.75	0.272	4.064	73.00	0.50
61	0.169	2.559	1.010	7.40	0.496	7.188	70.67	0.32
62	0.171	2.690	1.007	6.89	0.786	5.864	72.40	0.69
63	0.171	3.407	1.120	5.46	0.552	6.203	72.14	0.48
64	0.172	4.440	1.071	5.92	0.662	6.436	81.00	0.32
65	0.176	3.300	1.200	5.16	0.435	5.636	75.79	0.40
66	0.179	3.300	1.200	6.41	0.663	5.804	72.11	0.40
67	0.179	3.822	1.032	5.02	0.341	7.116	77.70	0.58
68	0.179	2.559	1.010	5.78	0.262	6.215	69.83	0.32
69	0.183	2.968	1.022	5.37	0.456	5.692	76.02	0.50
70	0.187	2.690	1.007	6.88	1.005	6.748	77.70	0.69
71	0.188	2.690	1.007	7.23	1.024	5.449	65.20	0.69
72	0.188	3.822	1.032	5.32	0.241	6.668	71.00	0.58
73	0.194	3.407	1.120	7.77	0.880	9.583	73.67	0.48
74	0.206	4.495	1.034	6.24	0.452	9.320	77.50	0.41
75	0.206	3.407	1.120	10.43	0.873	10.806	70.80	0.48
76	0.209	3.020	1.054	5.84	0.339	5.547	82.65	0.33
77	0.209	3.300	1.200	8.03	0.758	8.267	74.70	0.40
78	0.222	3.020	1.054	8.04	0.862	5.047	64.62	0.33
79	0.223	4.286	1.019	7.60	1.108	8.530	79.10	0.25
80	0.226	3.120	1.364	6.97	0.844	6.252	75.60	0.69
81	0.230	3.325	1.180	9.91	1.193	8.133	74.73	0.11
82	0.233	4.286	1.019	8.59	0.962	9.111	78.65	0.25

Sl. No.	Relative density	Aver. pore dia. mm	Cell aspect ratio	Plateau strength MPa	Young's modulus GPa	Energy absorption MJ/m ³	Densification strain %	ϕ
83	0.236	4.286	1.019	8.87	1.364	9.978	79.10	0.25
84	0.242	3.120	1.364	8.69	1.242	7.575	80.20	0.69
85	0.244	4.090	1.220	8.06	0.638	7.744	69.40	0.39
86	0.244	3.020	1.054	15.41	1.485	12.172	69.65	0.33
87	0.245	3.020	1.054	9.03	1.241	9.299	74.85	0.33
88	0.245	3.020	1.054	17.71	1.387	13.479	67.28	0.33
89	0.245	4.286	1.019	10.18	1.220	9.079	73.00	0.25
90	0.250	2.690	1.007	15.34	1.097	14.612	76.30	0.69
91	0.253	2.690	1.007	16.18	1.657	13.123	70.30	0.69
92	0.254	2.883	1.019	13.52	0.873	12.486	74.90	0.10
93	0.260	2.116	1.226	8.55	0.609	8.340	77.40	0.35
94	0.262	2.883	1.019	14.05	1.035	12.634	73.80	0.10
95	0.265	4.090	1.220	6.60	0.573	8.794	80.50	0.39
96	0.269	3.530	1.040	8.50	1.453	9.092	77.72	0.23
97	0.269	2.116	1.226	8.85	0.697	7.418	80.60	0.35
98	0.270	3.120	1.364	15.43	2.241	11.651	69.50	0.69
99	0.271	4.495	1.034	14.76	1.214	13.439	74.90	0.41
100	0.274	3.120	1.364	16.02	1.097	12.401	70.60	0.69
101	0.276	3.325	1.180	12.52	1.315	11.784	74.80	0.11
102	0.276	4.080	1.285	14.97	1.837	12.423	78.40	0.20
103	0.277	2.240	1.091	10.34	1.306	10.529	71.10	0.10
104	0.282	3.530	1.040	12.63	1.931	9.697	71.76	0.23
105	0.284	3.120	1.364	12.58	1.338	12.826	75.00	0.69
106	0.284	2.883	1.019	14.97	1.568	15.557	78.40	0.10
107	0.287	2.883	1.019	19.21	1.194	16.857	74.70	0.10
108	0.288	3.120	1.364	12.687	1.06	14.229	78.60	0.69
109	0.289	3.325	1.180	16.694	1.69	13.731	76.18	0.11
110	0.291	3.530	1.040	12.926	1.50	11.096	73.75	0.23

Sl. No.	Relative density	Aver. pore dia. mm	Cell aspect ratio	Plateau strength	Young's modulus	Energy absorption	Densification strain	ϕ
				MPa	GPa	MJ/m ³	%	
111	0.293	3.325	1.180	17.457	1.69	11.833	63.60	0.11
112	0.297	4.090	1.220	10.767	1.27	11.164	77.60	0.39
113	0.298	4.090	1.220	10.475	1.22	10.372	69.70	0.39
114	0.299	4.080	1.285	14.054	1.67	17.325	73.80	0.20
115	0.301	4.090	1.220	10.448	0.82	10.096	71.23	0.39
116	0.305	4.090	1.220	9.488	1.10	6.195	60.43	0.39
117	0.305	4.080	1.285	19.210	1.03	13.126	74.70	0.20
118	0.313	3.530	1.040	17.391	1.83	12.406	68.86	0.23
119	0.321	3.530	1.040	17.702	1.02	13.771	70.39	0.23
120	0.322	2.186	1.008	18.630	1.67	12.993	72.09	0.10
121	0.333	4.080	1.285	22.016	1.88	18.820	76.60	0.20
122	0.333	2.678	1.152	10.794	0.82	12.951	75.10	0.43
123	0.342	3.325	1.180	22.042	1.90	17.333	72.00	0.11
124	0.343	2.240	1.091	21.452	2.02	15.518	72.48	0.10
125	0.343	2.678	1.152	17.185	1.29	18.321	77.70	0.43
126	0.357	2.186	1.008	31.440	2.05	15.268	54.24	0.10
127	0.360	2.186	1.008	24.784	1.68	16.589	74.56	0.10
128	0.361	2.240	1.091	30.496	2.05	18.515	59.28	0.10
129	0.364	2.186	1.008	23.485	1.67	15.400	65.07	0.10
130	0.367	2.240	1.091	29.084	1.78	16.268	62.37	0.10
131	0.400	2.240	1.091	38.095	1.69	26.152	67.95	0.10

4.4.2. Dynamic Compression Test

The general description and working principle of the split Hopkinson pressure bar (SHPB) apparatus is given in section 3.4.7.2. The typical incident, ε_i , reflected, ε_r , and transmitted, ε_t , strain pulse obtained from the dynamic compression test of aluminum foam sample in SHPB apparatus is shown in Fig. 4.39.

The stress-strain values of the foam tested are determined from the strain gauge readings. From one dimensional theory of elastic wave propagation, the axial displacement $x(t)$ at time t is related to the axial strain history $\varepsilon(t)$ by

$$x = C \int_0^t \varepsilon dt \quad (4.9)$$

where C is the longitudinal wave speed in the bars given by:

$$C = \sqrt{E_b / \rho_b} \quad (4.10)$$

where E_b is the Young's modulus of the bar (Aluminum =69 GPa) and ρ_b is the density of the bar (Aluminum =2700 kg/m³). The axial displacement x_1 of the incident bar-specimen interface is due to the incident strain pulse, ε_i , travelling in the positive axial

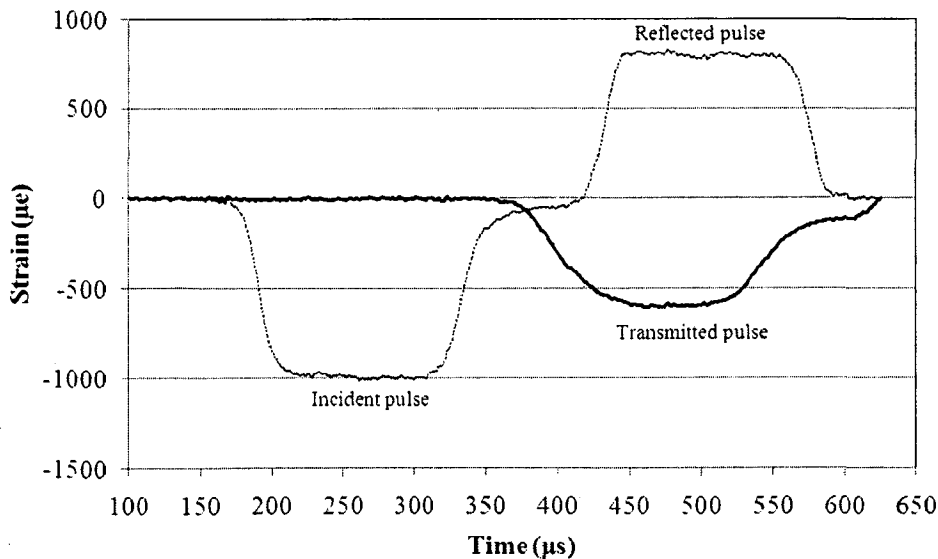


Fig. 4.39. Typical recorded strain histories by the strain gauges while conducting dynamic compression test in SHPB apparatus on an aluminum foam specimen.

direction and the reflected pulse, ε_r , travelling in the negative axial direction. Thus

$$x_1 = C \int_0^t (\varepsilon_i - \varepsilon_r) dt \quad (4.11)$$

Similarly, the displacement x_2 of the specimen-transmitter bar interface is obtained from the transmitted pulse, ε_t , as

$$x_2 = C \int_0^t \varepsilon_t dt \quad (4.12)$$

The compressive strain in the specimen, ε_{sp} is given as

$$\varepsilon_{sp} = \frac{x_1 - x_2}{L_{sp}} = \frac{C}{L_{sp}} \int_0^t (\varepsilon_i - \varepsilon_r - \varepsilon_t) dt \quad (4.13)$$

The equation (4.13) is applicable when the specimen is in stress equilibrium, i.e., the axial forces acting on the two loading surfaces of the specimen have the same magnitude. One such force equilibrium recorded for a sample during testing is shown in Fig. 4.40.

From force balance it can be written as

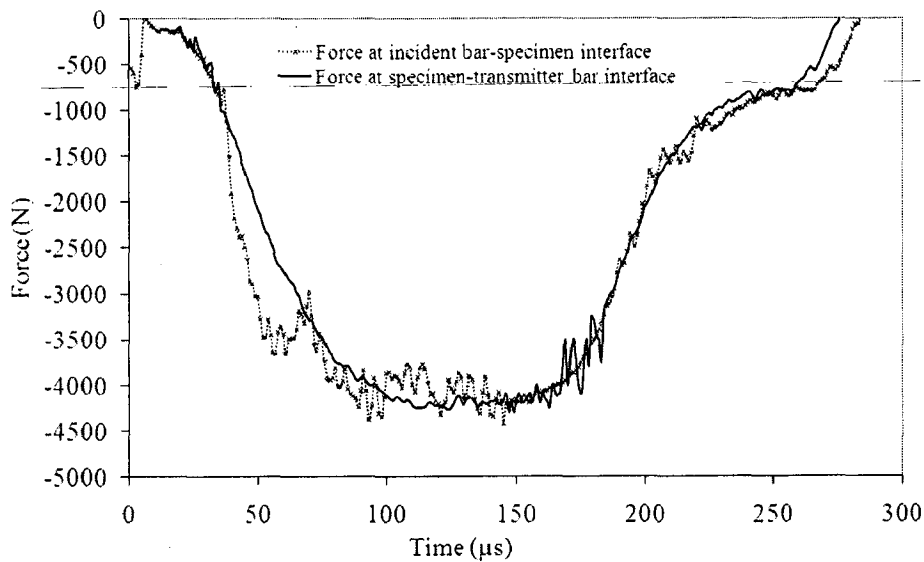


Fig. 4.40. The load histories at the two interface of the sample with the incident and transmitter bar showing equilibrium of forces.

$$E_i(\varepsilon_i + \varepsilon_r)A_i = E_t \varepsilon_t A_t \quad (4.14)$$

$$\varepsilon_t = \frac{A_i}{A_t}(\varepsilon_i + \varepsilon_r) \quad (4.15)$$

where A_i and A_t are the cross-sectional areas, E_i and E_t are the Young's modulus of the incident and the hollow transmitter bars, respectively. Substitution of equation (4.15) in equation (4.13) gives the expression for determining the compressive strain in the specimen when using hollow-transmitter bar as

$$\varepsilon_{sp}^* = \frac{C}{L_{sp}} \left[\left(1 - \frac{A_t}{A_i}\right) \int_0^t \varepsilon_i dt - \left(1 + \frac{A_t}{A_i}\right) \int_0^t \varepsilon_r dt \right] \quad (4.16)$$

The strain rate in the specimen is calculated by differentiating equation (4.16) with respect to time.

The average measured compressive strain rate in the specimens tested by SHPB apparatus is $7.5 \times 10^2 \text{ s}^{-1}$. The compressive stress in the specimen, σ_{sp} , is determined by the equation (3.2). The average velocity of impact by the striker during the testing of the specimens is 10 m/s. A typical strain rate in the specimen and velocity of striker during a dynamic test is shown in Fig. 4.41.

Forty two samples are tested under dynamic compression conditions, as two each from each set of experiments (8 in phase-I and 13 in phase-II). Similar number of foam samples with similar densities is also tested under quasi-static condition to compare the test results with the dynamic condition. In general, the mechanical properties of aluminum foam mainly depend on their relative density (Papadopoulos et al., 2004; Konstantinidis et al., 2005). The plateau stress increases with relative density, since increase in density means availability of more metal on the cell faces and edges, providing larger load bearing cross-section. For similar density foams, the plateau stress increases with pore diameter which can be explained on the basis of increasing cell wall thickness (Edwin and Daniel, 2008a).

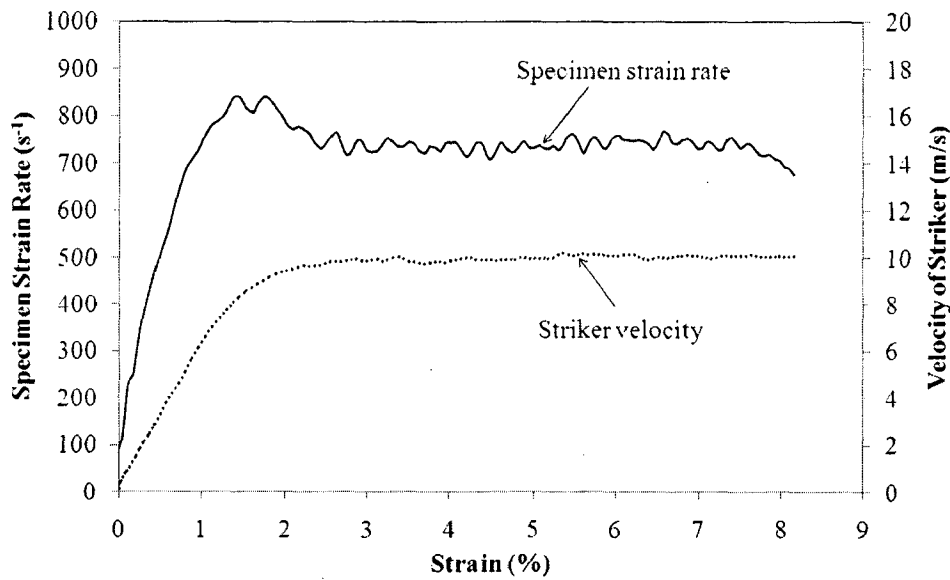


Fig. 4.41. Typical plot showing the strain rate of the specimen and the velocity of striker during a dynamic compression test in SHPB apparatus.

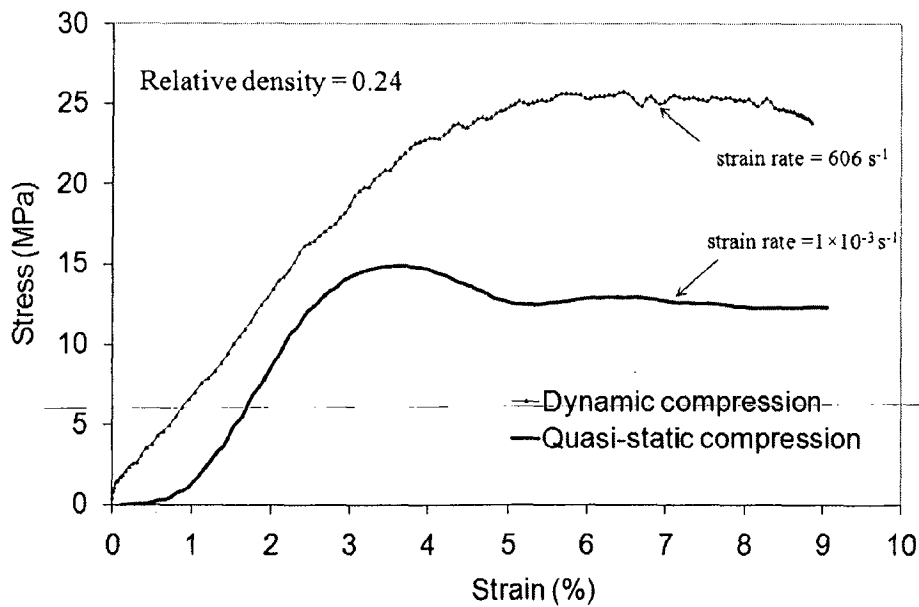


Fig. 4.42. A typical stress-strain plot of foam specimens having 0.24 relative densities tested under dynamic and quasi-static conditions.

A typical compressive stress-strain plot of the aluminum foam tested at dynamic and quasi-static conditions for the foam of relative density 0.24 is shown in Fig. 4.42. The plateau stress during dynamic compression test is higher than the foam specimens of

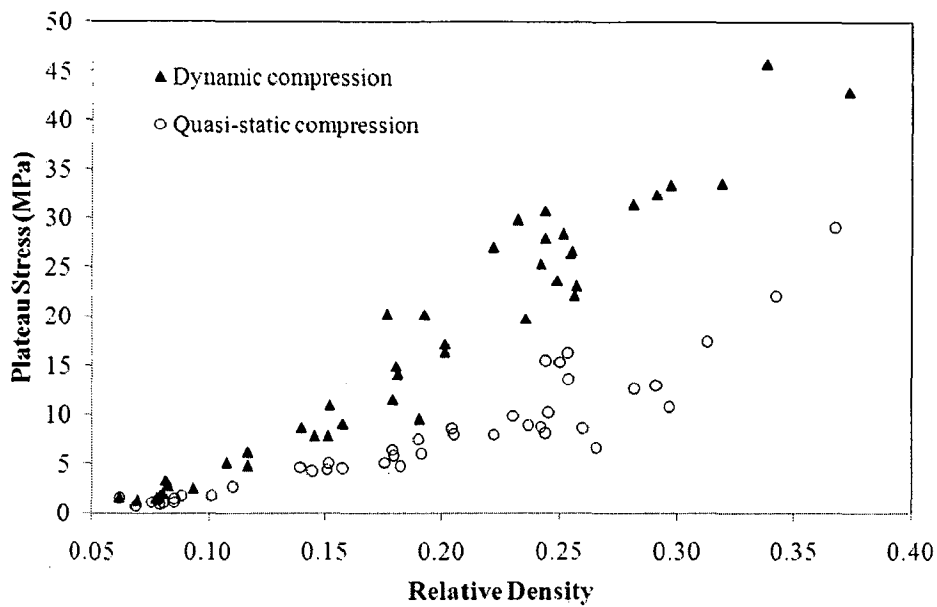


Fig. 4.43. Graph showing increase in plateau stress with respect to relative density and also to dynamic compression (higher strain rate) in comparison with quasi-static compression.

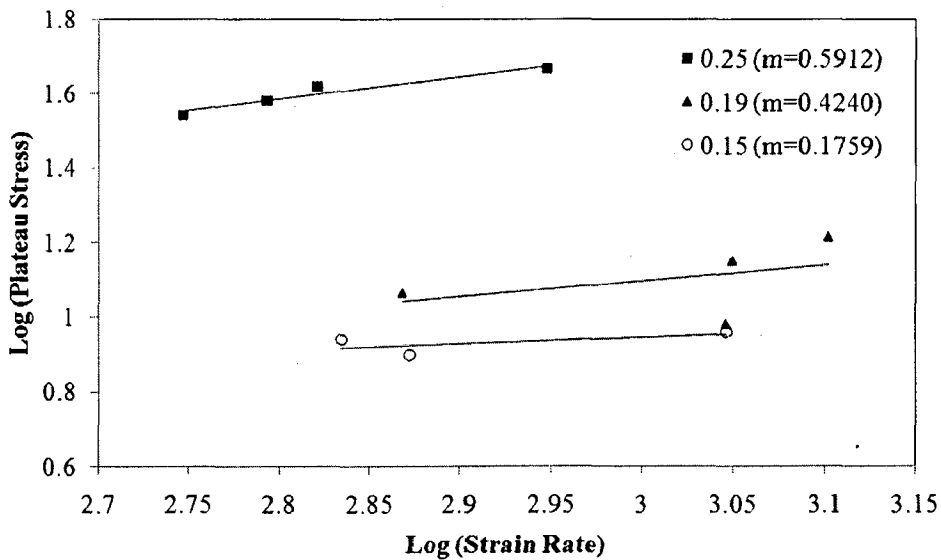


Fig. 4.44. Strain rate sensitivity increase with relative density foam as seen by increase in strain rate dependent term.

similar density when tested in quasi-static conditions. However, the enhanced plateau stress for dynamic condition is more prominent for high density foams (Fig. 4.43). At lower relative density, the strain rate sensitivity is rather insignificant. Moreover, the actual experimental strain rates for different compression tests in the SHPB apparatus

varied from 500 s^{-1} to 1000 s^{-1} . Strain rate sensitivity within the dynamic range was assessed by plotting the average plateau stress versus strain rate as shown in Fig. 4.44. The experimental result shows that the strain rate sensitivity parameter increases marginally with relative density. The structural properties of foam samples subjected to dynamic compression testing in SHPB apparatus along with their experimental specification and mechanical properties obtained are given in Table 4.19.

The internal mechanisms contributing to the phenomenon of increased stress levels at higher strain rates are not fully understood. However, one or more of the three reasons put forward may be behind the increased force-displacement response in dynamic compression (Yi et al., 2001). (1) In dynamic compression, the concentration of deformation at a given instant is on a thin layer, often adjacent to the loading face (Fig. 4.45). This leads to geometric softening causing local stress levels to increase. TEM bright field image of the deformed section in Fig. 4.46 reveals increased dislocation activity. (2) The micro-inertia associated with rotation and lateral motion of cell walls when they buckle in dynamic condition. Micro-inertia tends to suppress the more compliant buckling modes so it increases the crushing stress and (3) When closed-cell foam are deformed, the cell fluid inside is compressed/expanded and resist the deformation. This contribution from the fluid increases the resistance to deformation more in the dynamic case, causing the plateau stress to increase. The permeability of the fluid in the closed-cell foam of higher relative density is less due to thick cell walls with negligible cracks. Therefore, foams with higher relative density are more sensitive to strain rate, which is true in this system studied and reported here. Gibson and Ashby (1997) have studied the dynamic compression behaviour of closed cell polyethylene foam and reported similar reasons for the increased plateau stress.

In lower relative density foams, compression is throughout due to high velocity of impact, eliminating the

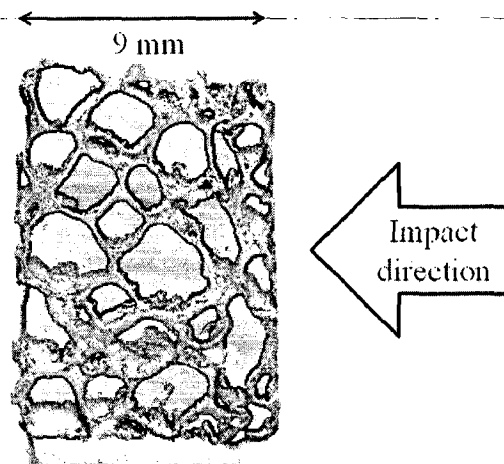


Fig. 4.45. Macrograph of a specimen after dynamic compression in SHPB apparatus.

localized strain condition for increased strain rate sensitivity. Moreover, at lower relative density the cell walls are very thin and usually have many hair line cracks on it, which may give up very easily during compression. This inadequate entrapment of gas inside the cells cause the gas to escape without offering any resistance such that they do not cause an increased stress during dynamic compression. However, at higher relative density the cell walls are thicker without defects effectively trapping the cell fluid during the sub-critical velocity impact. The effective participation of the cell wall material in strength enhancement is evidenced by the increased dislocation activity as shown in Fig. 4.46.

When the foam specimen is subjected to compression, the energy absorption capacity is defined as the energy necessary to deform a given specimen to a specific strain. So the absorption energy per unit volume of a sample, up to any particular strain ϵ_0 , can be evaluated by integrating the area under the stress-strain curve as given by the expression:

$$W = \int_0^{\epsilon_0} \sigma(\epsilon) d\epsilon \quad (4.17)$$



Fig. 4.46. Bright field TEM image of sample deformed at a strain rate of 750 s^{-1} showing increased dislocation activity within the cell wall.

The energy is first absorbed by elastic deformation followed by crushing of a layer, releasing part of its stored energy, and the energy absorption is again done by the deformation of the uncrushed layer and so on. From Fig. 4.45, it can be observed that the initiation of cell wall rupture occurs at the weakest link. This results in stress concentration on the cells located around the broken cell in the same layer, and the remaining cells in the layer breaks successively. Similarly the crushing phenomenon of cell wall layer spreads to other layer until all layers are crushed.

The energy absorption capacity of aluminum foams up to 8% is studied under quasi-static and dynamic conditions. The influence of strain rate upon energy absorption capacity for foams is readily apparent as seen from Fig. 4.47. The energy absorption capacity of foam increases with the relative density and the strain rate. Since this increase is connected with the plateau stress, similar reasons are valid for this phenomenon also. This increase in plateau stress and thereby energy absorption capacity at higher strain rate is very encouraging for high impact energy absorption applications. As reviewed in details in section 2.5.1.5, closed-cell aluminum foams have generally showed strain rate dependence as reported in the present work (Mukai et al., 2006; Mukai et al., 1999; Dannemann and Lankford, 2000; Ramachandra et al., 2003; Paul and Ramamurty, 2000).

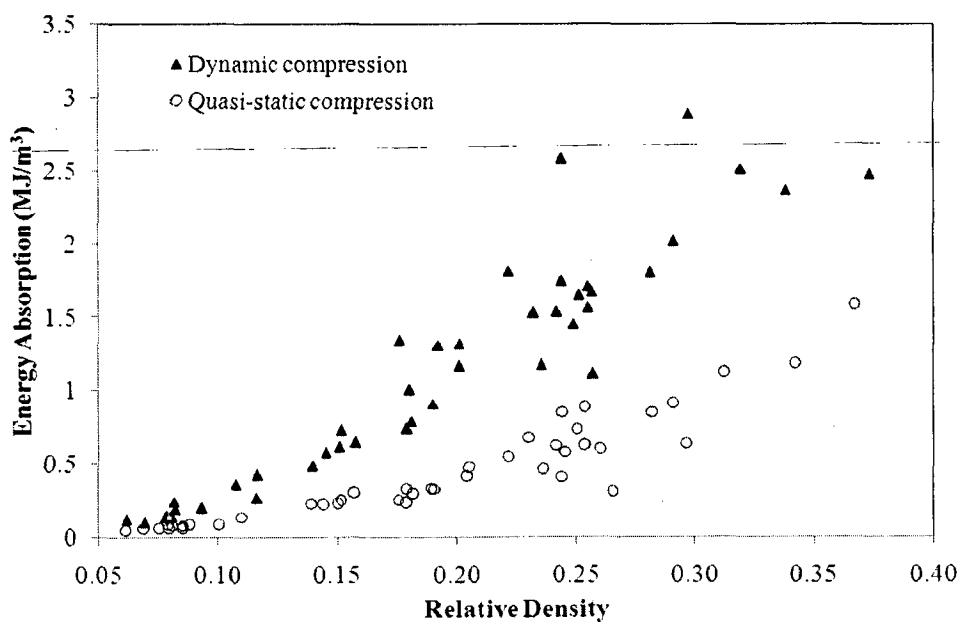


Fig. 4.47. Graph showing increase in energy absorption capacity up to 8% strain with respect to relative density and strain rate during compression.

Table 4.19. Dynamic compression test results of the closed-cell aluminum foam conducted using split Hopkinson pressure bar (SHPB) apparatus at higher strain rates.

Sl. No.	Rel. Density	Average Pore Dia. mm	Aspect Ratio	Velocity of the striker m/s	Strain Rate s ⁻¹	Plateau Stress MPa	Energy Absorption (up to 8% strain) MJ/m ³	Specific Strength kJ/kg
1	0.062	4.486	1.259	8.590	812.470	1.706	0.121	10.176
2	0.069	3.251	1.084	7.540	715.170	1.320	0.100	7.018
3	0.078	3.640	1.063	9.240	724.330	1.551	0.137	7.334
4	0.079	3.251	1.084	7.760	694.730	1.719	0.144	8.019
5	0.080	3.644	1.025	9.400	924.990	2.102	0.143	9.621
6	0.082	3.204	1.101	8.220	738.780	3.370	0.244	15.196
7	0.082	4.486	1.259	8.420	663.460	2.842	0.191	12.708
8	0.093	3.644	1.025	8.310	712.790	2.587	0.199	10.213
9	0.108	3.232	1.107	9.250	850.520	5.107	0.361	17.459
10	0.116	3.640	1.063	10.000	874.260	4.784	0.271	15.117
11	0.117	3.200	1.087	8.930	672.030	6.170	0.424	19.465
12	0.140	3.232	1.107	8.310	683.040	8.712	0.484	22.920
13	0.145	3.407	1.120	10.040	919.560	7.869	0.575	19.946
14	0.151	3.204	1.101	9.010	745.590	7.895	0.618	19.241
15	0.152	3.251	1.084	9.500	687.860	11.012	0.730	26.677
16	0.157	2.931	1.085	13.200	1113.240	9.121	0.650	21.296
17	0.176	5.180	1.072	10.440	728.780	20.246	1.341	42.252
18	0.179	3.300	1.200	9.740	737.960	11.603	0.740	23.836
19	0.180	2.968	1.022	9.390	659.550	14.962	1.005	30.530
20	0.181	2.931	1.085	12.550	1120.730	14.169	0.792	28.802
21	0.190	3.407	1.120	12.620	1112.200	9.585	0.909	18.530
22	0.192	2.690	1.007	9.470	507.590	20.198	1.306	38.621
23	0.201	2.559	1.010	14.850	1265.340	16.407	1.315	29.999
24	0.201	3.200	1.087	8.140	574.670	17.247	1.164	31.503
25	0.221	2.690	1.007	10.720	638.950	27.051	1.812	44.902

26	0.232	5.180	1.072	9.690	401.700	29.850	1.526	47.326
27	0.235	2.883	1.019	9.260	630.340	19.803	1.172	30.943
28	0.242	3.020	1.054	10.020	594.690	25.350	1.532	38.545
29	0.244	2.559	1.010	12.790	886.560	30.804	2.581	46.455
30	0.244	3.120	1.364	10.240	560.120	28.019	1.743	42.236
31	0.249	2.883	1.019	9.730	558.600	23.656	1.451	34.972
32	0.251	3.020	1.054	10.640	662.480	28.450	1.646	41.656
33	0.255	3.120	1.364	10.250	621.110	26.450	1.563	38.180
34	0.255	3.300	1.200	9.420	544.220	26.720	1.703	38.540
35	0.256	2.968	1.022	10.400	609.860	22.118	1.669	31.715
36	0.257	3.325	1.180	9.094	821.780	23.099	1.112	33.032
37	0.281	3.530	1.040	10.610	560.270	31.418	1.802	41.090
38	0.291	3.530	1.040	10.380	548.100	32.470	2.014	41.008
39	0.297	3.325	1.180	14.050	921.820	33.389	2.884	41.288
40	0.319	2.186	1.008	12.050	726.180	33.664	2.511	38.772
41	0.338	2.240	1.091	12.890	795.660	45.805	2.366	49.804
42	0.373	2.186	1.008	11.010	711.280	42.974	2.477	42.342

4.5. Statistical Modelling and Analysis

The limitations of the various modelling tools used to predict the mechanical properties of aluminum foam are reviewed in section 2.7. The high variability in the foam cell structure and complex relationship between structural and mechanical properties makes, analytical modelling highly involved. The Gibson and Ashby's analytical model is tried in this system and the results were compared with experimental results, but the results were not encouraging, especially for the Young's modulus prediction. Under these circumstances it is decided to try out the popular linear and non-linear statistical modelling tools for simulation of mechanical property. Since large data base correlating the structural properties with the mechanical properties of foam are available from the quasi-static compression test, an attempt is made to predict the mechanical properties using two statistical tools, namely, multiple linear regression and artificial neural network (ANN). The basics of these modelling tools are briefed in section 3.5.2 and 3.5.3 respectively. The advantage of using the multiple linear regression analysis is that it gives a correlation equation based on the structural properties used for each of its model and also it is very flexible and simple in estimation. On the other hand, ANN model is a black box approach of input-output mapping; but the advantage is that they can handle non-linear relation rather effectively. Both the models have incorporated the contribution of pore diameter and cell aspect ratio variation in the cell structure of the foam, which were not taken into consideration in analytical models. Once the model is trained properly, they can predict the output very efficiently within the experimental range.

Recent literature on the mechanical property correlation studies with structural parameters confirms the effect of cell diameter along with relative density for aluminum foam (Yu et al., 2007; Cao et al., 2006; Bin et al., 2007). Yu et al. (2007) have reported that, for the same relative density, the peak stress and Young's modulus of aluminum foam increases with increase in cell diameter. However, bigger cell size induces inhomogeneity in the structure resulting in marked oscillation in stress values. Such phenomenon is observed in the present work as well. For the foams of similar density, the foam having larger pore diameter exhibits higher plateau stress than the one with smaller pore diameter (see Fig. 4.34). The cell size effects on the energy absorption capacity are not as significant as those on the modulus and strength of foams (Cao et al., 2006). Direct

dependence of plateau stress and Young's modulus with relative density is also reported in the literature (Koza et al., 2003; Olurin et al., 2000; Fushong and Zhengang, 1999; Banhart and Baumeister, 1998). All these results points to the fact that the mechanical property of foam along with the physical property of the foam depends on the morphological features as well.

The quasi-static compression test data are tabulated in the ascending order of the relative density in Table 4.18. Every third data is separated and used for testing and validating those developed models. However, the remaining two third of the data is initially used for formulating the regression coefficients in multiple linear regressions and for training the ANN models. By this way, care is taken to cover the entire experimental range for developing and testing the models.

4.5.1. Multiple Linear Regression Model

In the first case, multiple linear regression technique is employed by using the structural parameters such as relative density, average pore diameter and cell aspect ratio as the independent variables. The dependent variable is one of the mechanical properties such as plateau stress, Young's modulus and energy absorption capacity.

In the present study, the structural properties of foam selected as independent variables are relative density (ρ^*/ρ_s), cell diameter effect (d/D), and cell aspect ratio effect (K/K_p), where d is the average cell diameter, D is the crucible diameter taken as 100 mm, K is the cell aspect ratio and K_p is the ideal cell aspect ratio taken as unity. Models have been developed for each dependent variable: plateau stress, Young's modulus and energy absorption capacity of the foam. The regression model equations based on the best correlation coefficient are given below:

The plateau stress of the foam is given by

$$\left(\frac{\sigma_{pl}^*}{\sigma_{ys}}\right) = 0.208022 + 2.270552\left(\frac{\rho}{\rho_s}\right)^{3/2} - 3.66982\left(\frac{d}{D}\right) - 0.11336\left(\frac{K}{K_p}\right) \quad (4.18)$$

The Young's modulus of the foam is given by

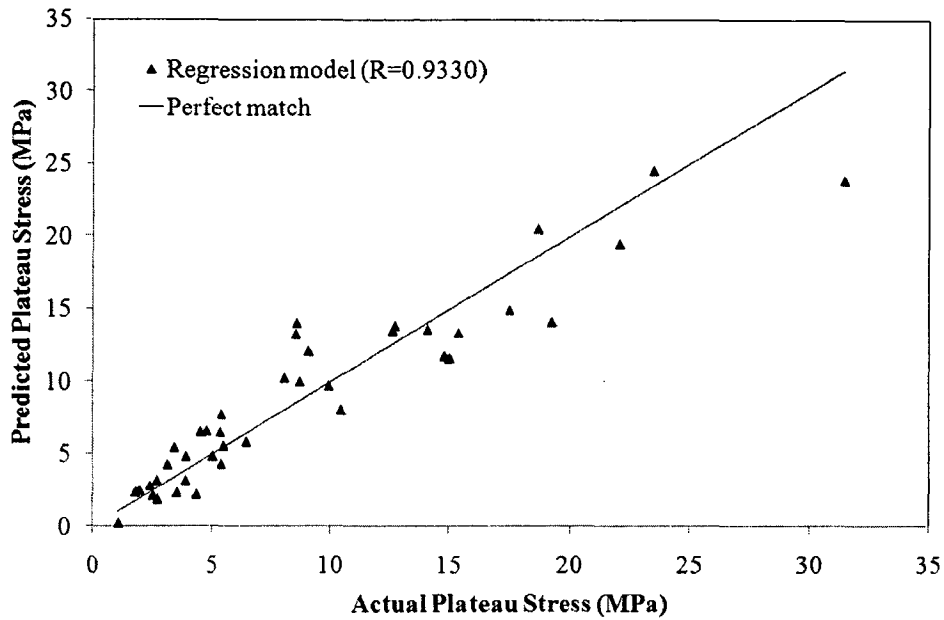


Fig. 4.48. Regression model predicted plateau stress values compared with experimental results.

$$\left(\frac{E^*}{E_s}\right) = 0.006297 + 0.224663\left(\frac{\rho}{\rho_s}\right)^2 + 0.002584\left(\frac{d}{D}\right) - 0.00424\left(\frac{K}{K_p}\right) \quad (4.19)$$

The Gibson and Ashby model for the plateau stress includes the terms $(\rho^*/\rho_s)^{3/2}$ and (ρ^*/ρ_s) which are due to the cell edge effect and the cell face effect, respectively (see equation (4.4)). However in the regression analysis of the experimental data, inclusion of the term (ρ^*/ρ_s) along with $(\rho^*/\rho_s)^{3/2}$ does not improve the correlation coefficient suggesting that there is significantly less contribution from the cell face in this system. Furthermore, by changing the powers of independent variable and comparing the correlation coefficient value, it is confirmed that the power of 3/2 on relative density gave the best fit, which is the contribution of cell edge effect. The developed correlation equation (4.18) is used to simulate the plateau stress values by using 43 structural data sets (Table 4.18) and checked with the experimental plateau stress results (Fig. 4.48). The correlation of 0.9330 indicates that the model prediction is adequate.

The Young's modulus model for regular hexagonal closed-cell foam, given by Gibson and Ashby, includes two terms $(\rho^*/\rho_s)^2$ and (ρ^*/ρ_s) which are the cell edge and

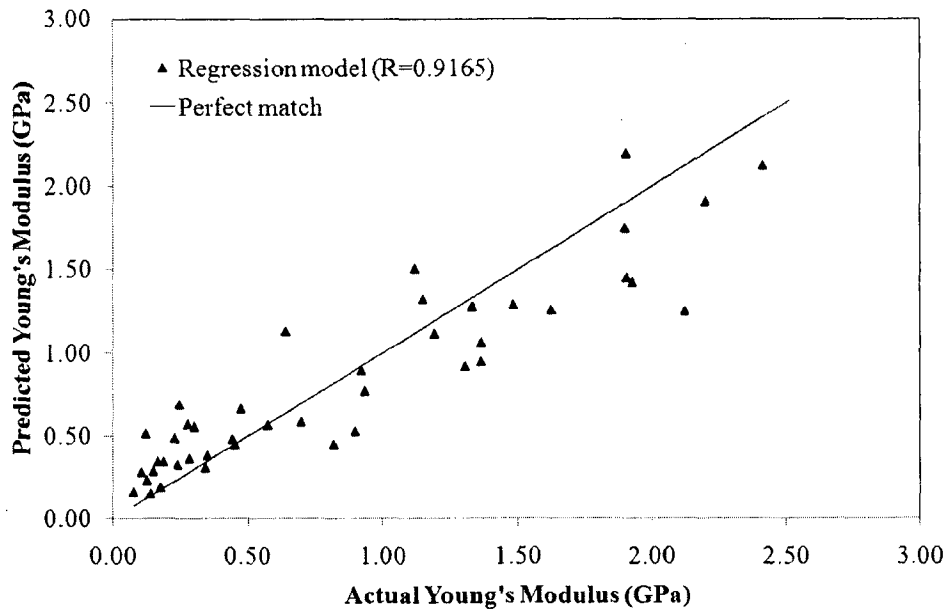


Fig. 4.49. Comparison of the Young's modulus prediction values by regression model with the experimental values.

cell face effects respectively as shown in equation (4.5). However inclusion of the term (ρ^*/ρ_s) is found to be insignificant in the regression analysis suggesting again that the cell face effect is negligible in this system. The regression model with best correlation coefficient for Young's modulus is obtained when the square of relative density is used as given in equation (4.19). From this it is clear that the cell edge effect supersedes the cell face effects in this system. Fig. 4.49 shows the regression analysis results of Young's modulus plotted against the actual experimental results. The perfect match line is nothing but a one to one correlation of predicted and actual values.

Aluminum foams are good energy absorbers and the experimental energy absorption capacity per unit volume (W) of closed-cell aluminum foam is calculated by the equation (3.1), reproduced for convenience below

$$W = \int_0^{\varepsilon_d} \sigma(\varepsilon) d\varepsilon$$

where σ is the stress when the strain is ε and ε_d is the densification strain. The energy absorption capacity of aluminum foam is also modelled by multiple linear regressions. The best fit is obtained for the energy absorption (W in MJ/m^3) equation of the form:

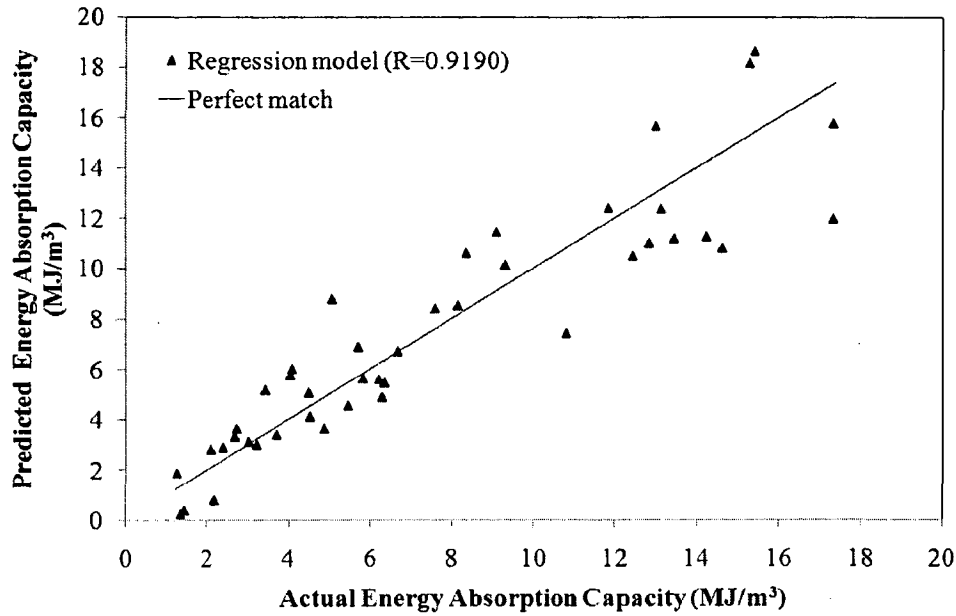


Fig. 4.50. Comparison of the energy absorption capacity prediction values by regression model with the experimental values.

$$W = 6.751746 + 80.73748 \left(\frac{\rho}{\rho_s} \right)^{3/2} + 43.1547 \left(\frac{d}{D} \right) - 4.83488 \left(\frac{K}{K_p} \right) \quad (4.20)$$

The predicted energy absorption capacity of foam is plotted against the experimental results is shown in Fig. 4.50. Once again the best correlation is obtained with the power of 3/2 for the relative density term which is similar to the plateau stress regression given in equation (4.18). This is because the energy absorption is a summation of stress over strain until densification. The regression models are inclusive of structural effects with good agreement with the actual experimental results. The regression coefficient equations obtained can be used to predict the mechanical properties if the simple structural parameters such as the relative density, the average pore diameter and cell aspect ratio are known.

4.5.2. Artificial Neural Network Model

A brief overview of artificial neural network (ANN) is already given in section 3.5.3. In this work, neural network modelling is used to correlate the physical and morphological properties of the foam to the compressive properties of the foam. Two third of the quasi-static compression test data (88 data sets) are used for training the ANN model and the remaining one third of the data set (43 data sets) are used for testing the

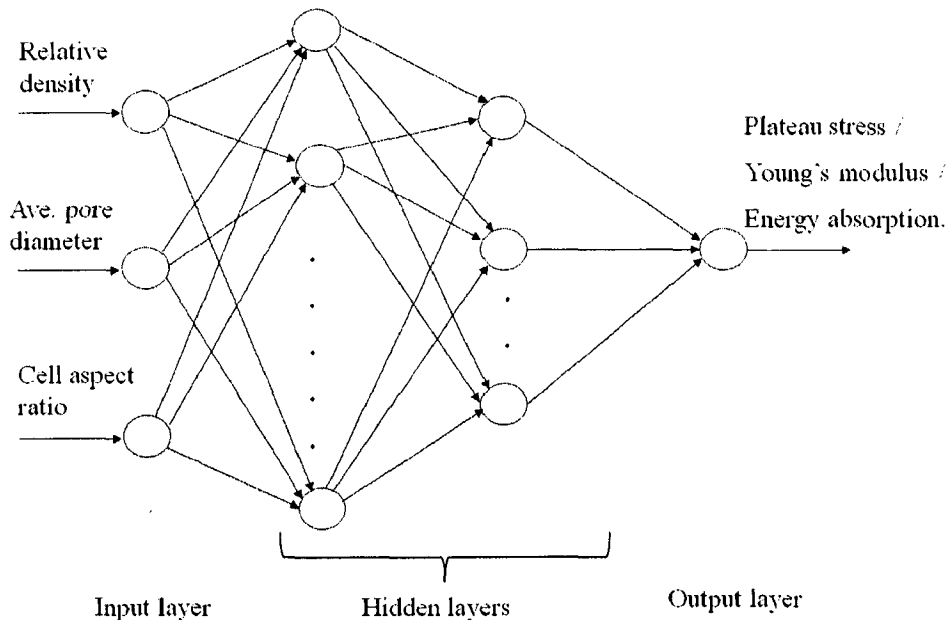


Fig. 4.51. Typical schematic diagram of the feed forward neural network used for the development of models.

model. The data are tabulated in Table 4.18 along with the corresponding structural parameters. The use of neural network is gaining importance in the metallurgy field recently, due to its robustness in predicting complex, ill-defined and non-linear property correlations (Rajasekara and Pai, 2003; Kishan et al., 1997; Freeman and Skapura, 1991).

The modelling of mechanical properties of composite materials has been reviewed and the results have shown the predictive quality of ANN to be better than the conventional methods (El Kadi, 2006; Singh and Deo, 1996). The non-linear mapping relation between the components, the flexural strength, and the fracture toughness of the ceramic tool was investigated and accurately modelled using ANN (Huang et al., 2002). A neural network model for the prediction of the correlation between alloy composition, microstructure and its tensile properties was developed for gamma-based titanium aluminate alloy (McBride et al., 2004). The model was extended to optimize processing parameters in conjunction with its tensile properties. Based on the experimental database for short fibre reinforced polyamide 4-6 composite, the specific wear rate, frictional coefficient and some mechanical properties, such as compressive strength and modulus were successfully predicted by well-trained ANN model (Jiang et al., 2007). It is reported that the prediction accuracy is reasonable and were in good agreement with the actual

data. Similarly, the mechanical properties of other materials were simulated using artificial neural network model and reported that ANN is showing excellent capability (Li et al., 2002; Zhang and Friedrich, 2003; Hsiang and Kuo, 2005; Bezerra et al., 2007; Hosseini et al., 2004).

4.5.2.1. Model Development

ANN models are developed separately for the prediction of mechanical properties of foam, namely, the plateau stress, the Young's modulus and the energy absorption capacity of the closed-cell aluminum foam from the structural properties of foam (Edwin and Daniel, 2008b). These are the significant mechanical properties to evaluate the quality and strength of the aluminum foam. The three structural properties of foam such as, the relative density, average pore diameter and cell aspect ratio are commonly taken as input variables for all the models developed. However, the output is varied for each ANN model with one of the compressive properties: plateau stress, Young's modulus and energy absorption capacity of the aluminum foam (Fig. 4.51). The input parameters are chosen in such a way that determination of these properties of foam is rather straight forward and simple.

The Fig. 4.52 and Fig. 4.53 show the non-linear complex dependence of the average pore diameter with the physical and mechanical property of the aluminum foam.

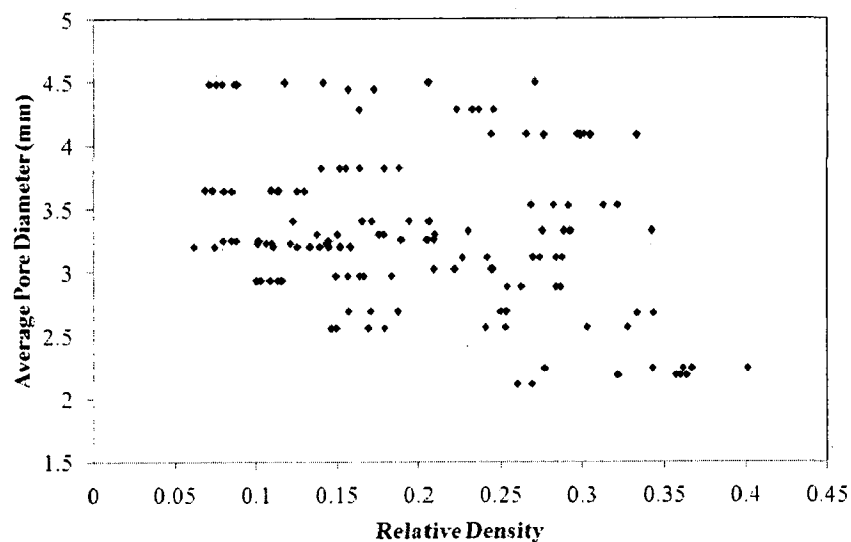


Fig. 4.52. Scattered distribution of average pore diameter of the foam with respect to relative density showing complex dependence.

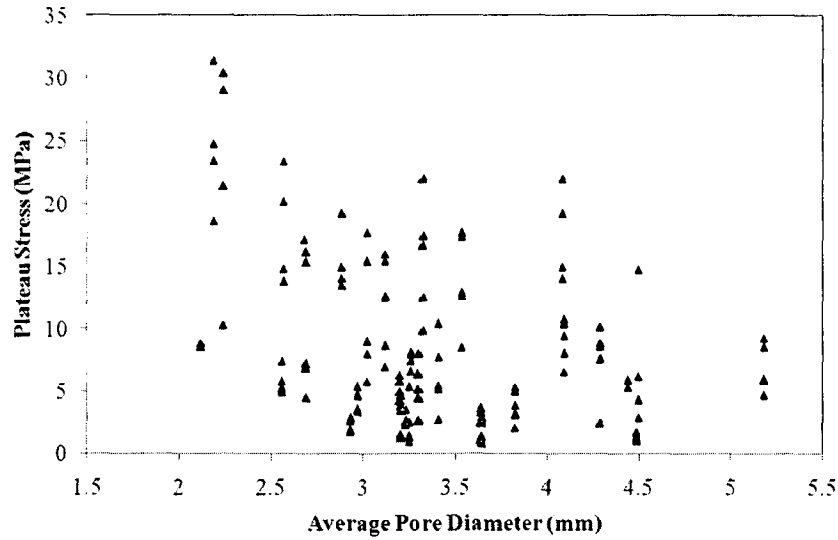


Fig. 4.53. Plateau stress variation with respect to average pore diameter showing a fully random and scattered plot.

The correlation study of all the structural parameters with the compressive properties are also done to justify the use of the variable in ANN models. For example, the correlation of plateau stress with relative density is as high as 0.9119, followed by its correlation with average pore diameter at 0.3708 and with the cell aspect ratio at least correlation of 0.1670. Since ANN is widely accepted as a technology offering an alternative way to tackle complex and ill-defined problems, an attempt is made to develop models for the prediction of mechanical properties of foam using the structural parameters.

4.5.2.2. Data Analysis

As mentioned earlier, two-third of the data is used for training the ANN models and the remaining one-third of the data is used for testing and validating the developed model. During training of a neural network, the higher valued variables may suppress the influence of smaller valued variables. Normalization helps to minimize the effects of magnitude variation in the data. Hence, the input and output variables are normalized according to the relation given below:

$$X_N = 0.8 \times \frac{(X - X_{min})}{(X_{max} - X_{min})} + 0.1 \quad (4.18)$$

where X_N is the normalized value of the variable X that have maximum and minimum values given by X_{max} and X_{min} , respectively.

4.5.2.3. Estimation of Plateau Stress

The experimental plateau stress values of the dataset vary from 0.808 to 38.095 MPa. Number of neural network architectures were tried to train the data set. The best topology is selected, when the training and the testing errors produced are satisfactory. The suitable topology finalized for the plateau stress model is 3-8-9-1 (3 neurons in the input layer, 8 neurons in first hidden layer, 9 neurons in the second hidden layer and one neuron in the output layer). The activation functions used are hyperbolic tangent, 'tansig' in the first hidden layer, 'logsig' in the second hidden layer and the linear transfer function, 'purelin' in the output layer. The neural network training performance curve is shown in Fig. 4.54, which indicates that the convergence to mean square error of 8.8463×10^{-4} is achieved in the eighth iteration itself. The obtained model is tested with data not considered in the training data set and the mean square error of 3.3×10^{-3} is obtained. The ANN model prediction of plateau stress along with the experimental values is shown in Fig. 4.55 is an indication of fairly good accuracy in prediction. The predicted values and the experimental values are plotted against each other and are shown in Fig. 4.56. Good correlation is obtained between the predicted and measured values with correlation coefficient, R of 0.9602 indicating very good agreement with the actual values.

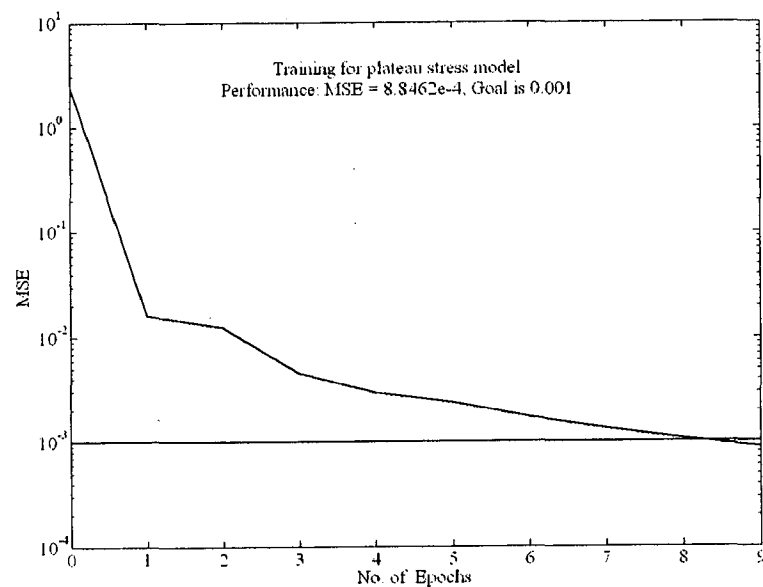


Fig. 4.54. Mean square error convergence during training of the ANN model 3-8-9-1 for plateau stress.

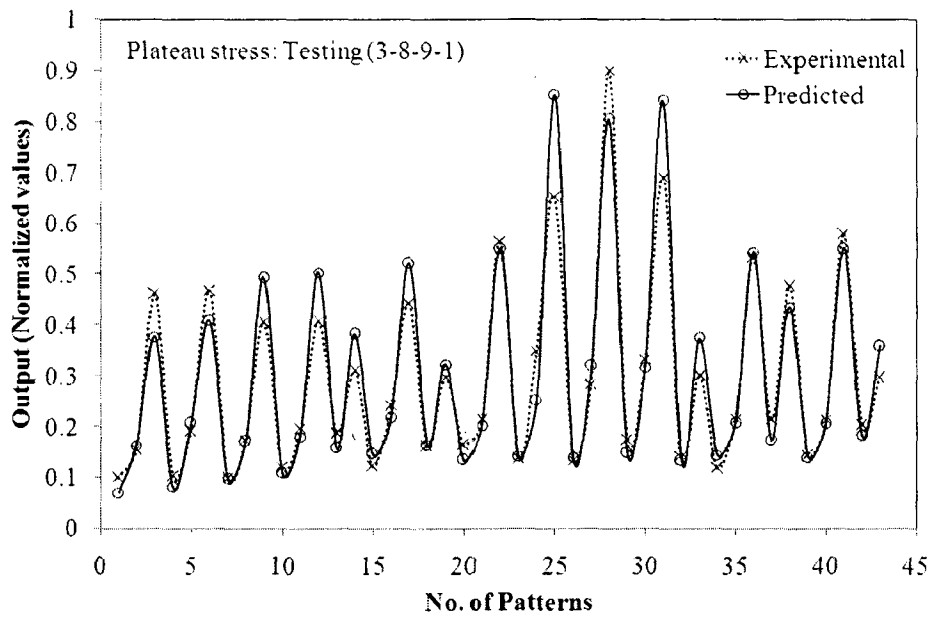


Fig. 4.55. Predicted values of the test patterns for the plateau stress along with experimental values.

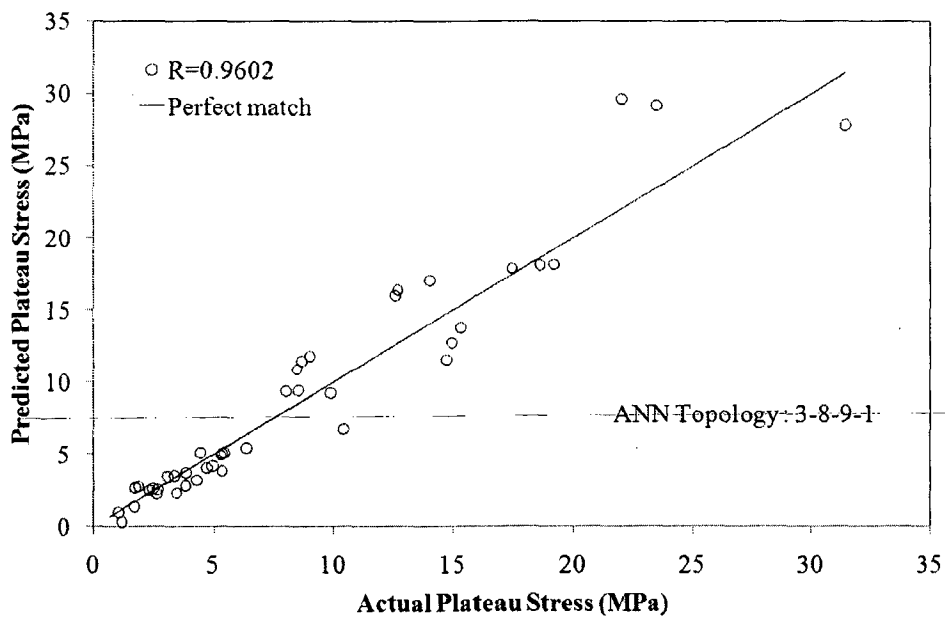


Fig. 4.56. ANN model simulation results compared with experimental results for plateau stress shown along with the perfect match line.

4.5.2.4. Estimation of Young's Modulus

The unsureness to determine the experimental values of Young's modulus persist during compression testing of aluminum foam. However, it is obtained from the initial linear region of stress-strain curve. The Young's modulus values range from 0.048 GPa to 2.679 GPa for the mentioned input variables. The correlation of Young's modulus with

these input variables is quite complex and non-linear. This can be observed by the scatter in the experimental plot and also signified in the poor prediction by Gibson and Ashby model. After several trials with different neural network topology, the best topology which produced satisfactory results is 3-2-1 (3 neurons in the input layer, 2 neurons in the hidden layer, and one neuron in the output layer). In this case the activation functions used are 'logsig' in the hidden layer and 'purelin' in the output layer. The training performance curve is shown in Fig. 4.57. The convergence to mean square error of 9.2×10^{-3} is achieved. However, the tested model (Fig. 4.58.) with data not used during training gave MSE of 9.0×10^{-3} . The predicted and the experimental Young's modulus values are studied for correlation and plotted together in Fig. 4.59. A fairly good correlation coefficient, R of 0.9270 is found between the model prediction and the experimental Young's modulus values.

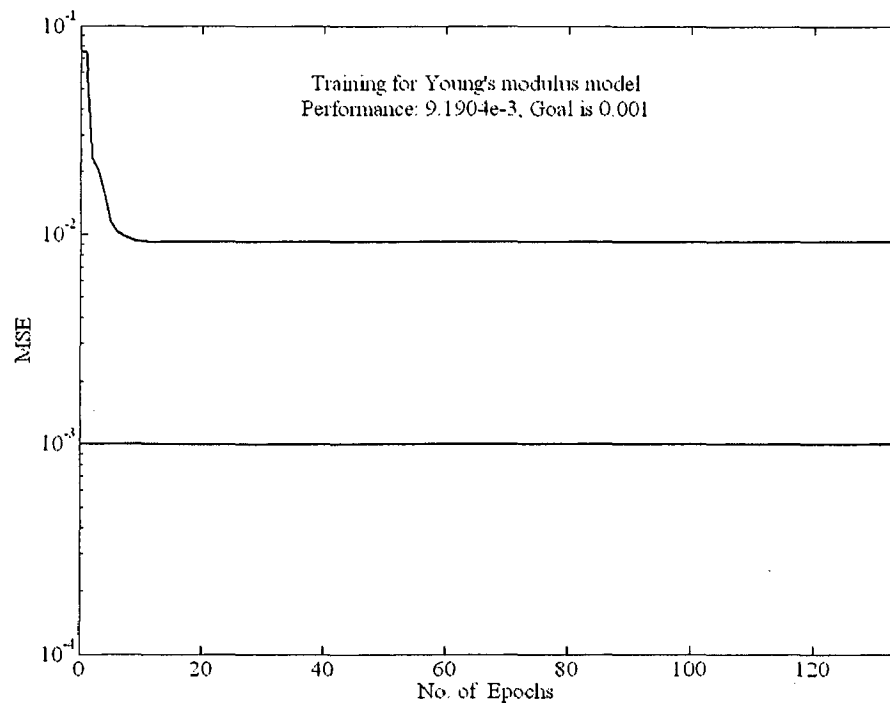


Fig. 4.57. Mean square error convergence during training of the ANN model 3-2-1 for Young's modulus.

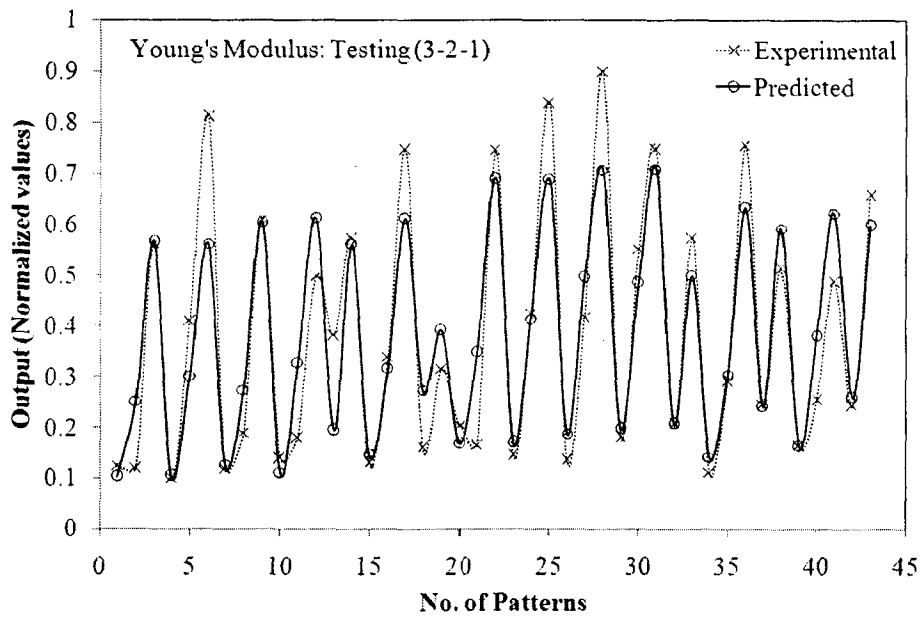


Fig. 4.58. Predicted values of the test patterns for the Young's modulus along with experimental values.

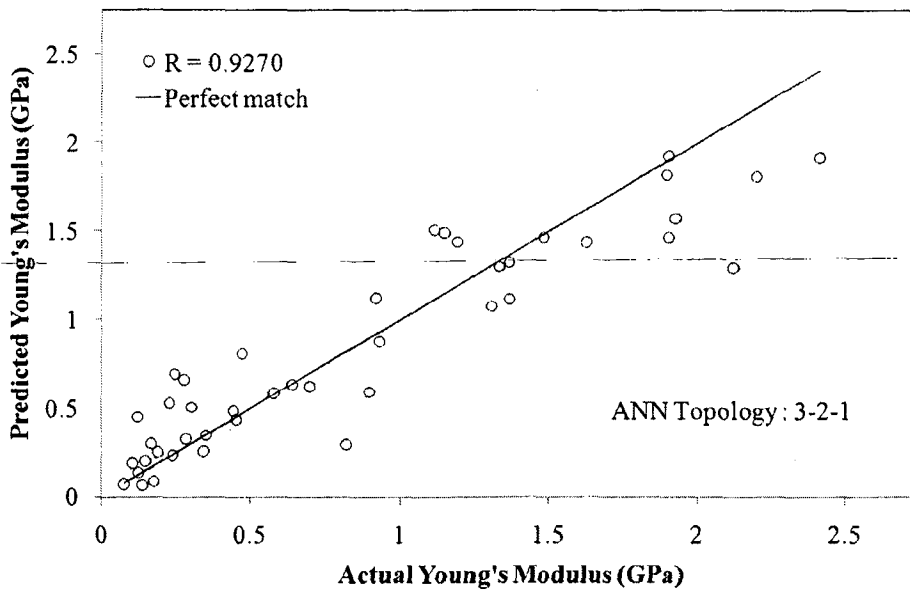


Fig.4.59. ANN model simulation results compared with experimental results for Young's modulus shown along with the perfect match line.

4.5.2.5. Estimation of Energy Absorption

Two cases are taken for developing ANN models for the estimation of energy absorption capacity of the closed-cell aluminum foam. The energy absorption per unit volume and the plateau stress are the two important properties that determine the potential application of the foam for energy absorption. The energy absorption per unit volume determines the thickness/volume of foam structure required for the particular impact/blast energy absorption application. The maximum allowable plateau stress levels are governed by the force the structures can withstand. The energy absorption capacity varies from 0.951 MJ/m^3 to 26.152 MJ/m^3 for the mentioned input variables.

4.5.2.5.1. Model I

This model is developed by considering only the structural properties of foam as input variables. They are the relative density, average cell diameter and cell aspect ratio, as considered previously for other models. These properties are easily measurable structural characteristics of closed-cell aluminum foam. The output of the model I is the energy absorption capacity. Different topologies are tried and the best neural network topology which provide good training and testing result is 3-6-6-1 (3 neurons in the input layer, 6 neurons in the first hidden layer, 6 neurons in the second hidden layer and one neuron in the output layer). The performance curve during training of the data pattern in MATLAB software is shown in Fig. 4.60.

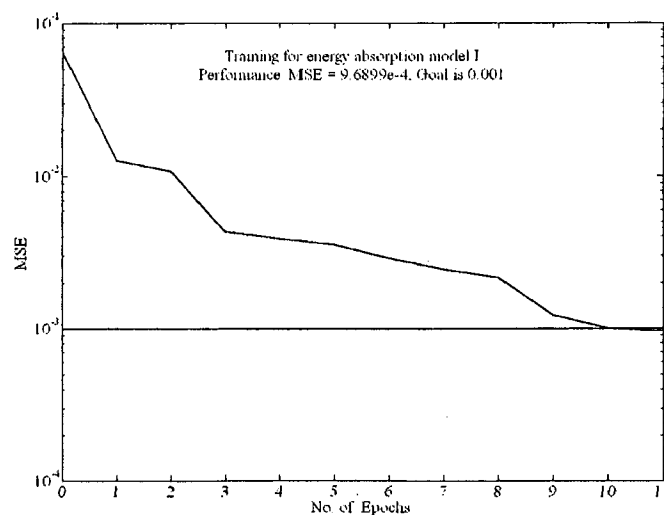


Fig. 4.60. Training performance plot showing convergence of MSE of the ANN model I 3-6-6-1 for energy absorption capacity evaluation.

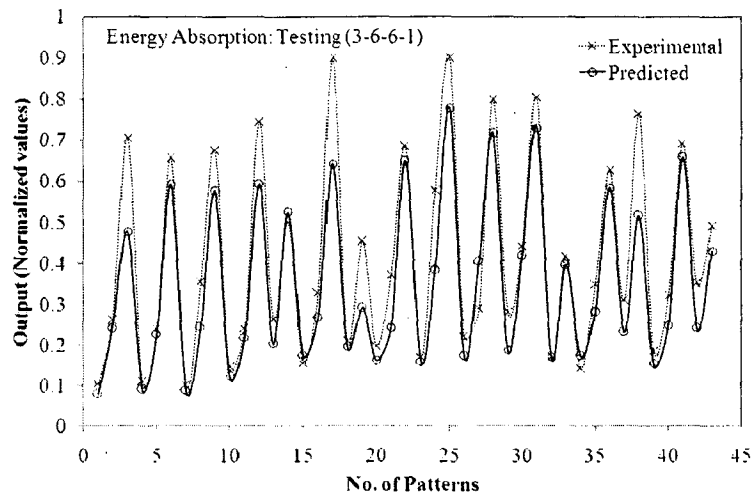


Fig. 4.61. Testing results of the ANN model I 3-6-6-1 for energy absorption prediction.

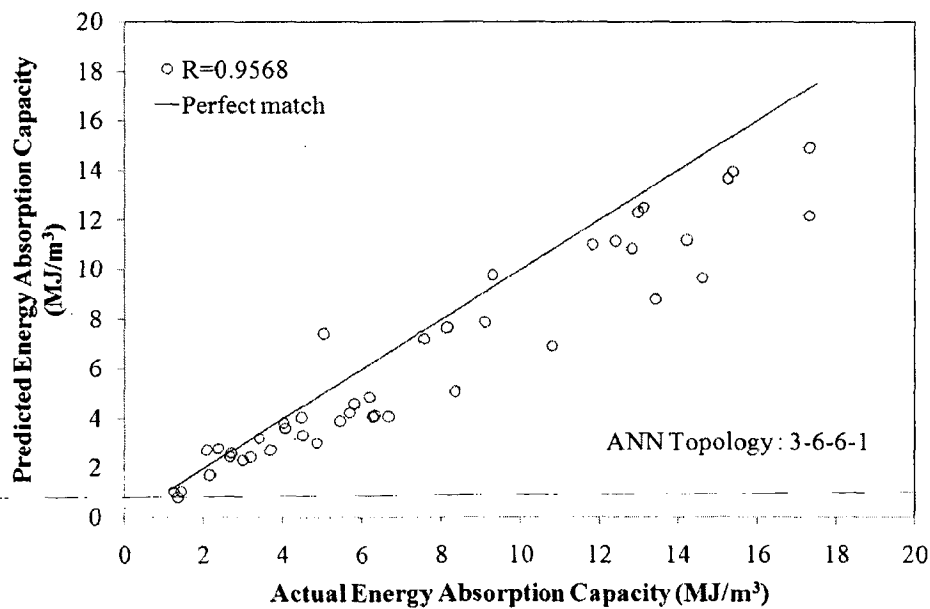


Fig. 4.62. Performance evaluation of model I simulation results for energy absorption capacity in comparison with experimental values.

The mean square error got saturated after 15 iterations and remains constant at 9.6899×10^{-4} . The activation function like ‘tansig’ and ‘purelin’ are used in the neural network. The trained neural network is tested with new set of data not used for training and the model prediction is shown in Fig. 4.61. The mean square error of the tested ANN model is 9.6×10^{-3} . The predicted and the experimental values are plotted against each

other along with perfect match line and shown in Fig. 4.62. The results are in good agreement with the actual values which is indicated by the correlation coefficient of $R = 0.9568$.

4.5.2.5.2. Model II

In actual application the plateau stress determines the sustainable force levels specified for a particular foam material. Moreover, the density of foam governs the thickness required for that particular energy absorption capacity. Therefore the second model for energy absorption capacity is developed by considering the plateau stress and relative density of foam as the input variables for the neural network. After several trials with different topologies, the best topology is selected when the training and testing errors are within the satisfactory limits. The best topology finalized for this model is 2-2-4-1 (2 neurons in the input layer, 2 neurons in the first hidden layer, 4 neurons in the second hidden layer and one neuron in the output layer). The hyperbolic transfer function 'tansig' is used in the hidden layers and linear transfer function 'purelin' in the output layer. The training performance curve of the neural network is shown in Fig. 4.63 with a mean square error of 9.8988×10^{-4} .

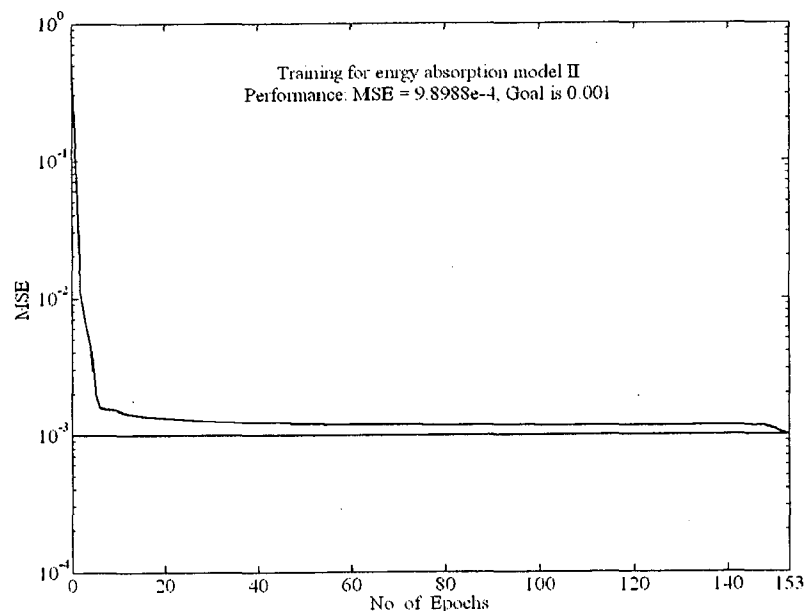


Fig. 4.63. Training performance plot showing convergence of MSE of the ANN model II 2-2-4-1 for energy absorption capacity evaluation.

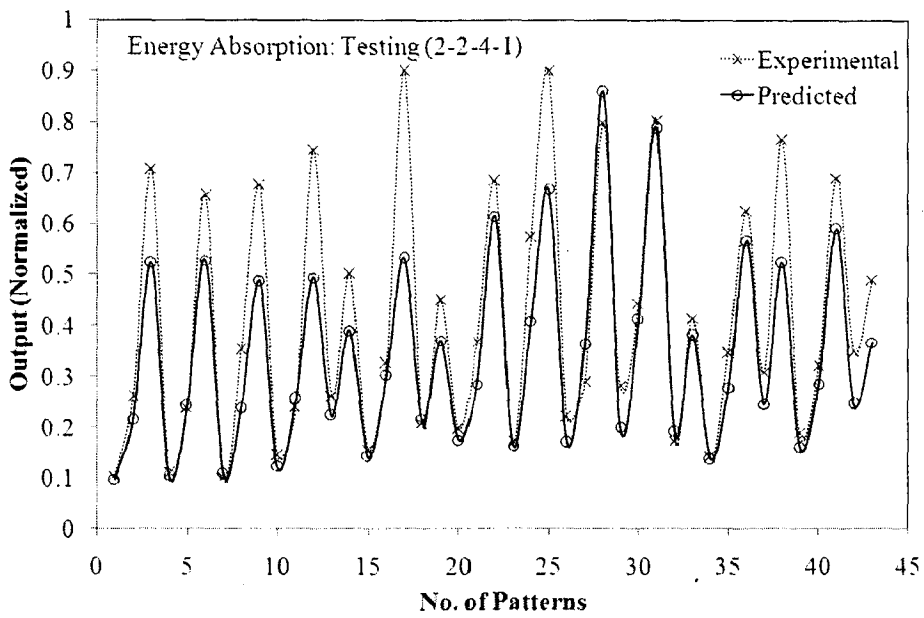


Fig. 4.64. Testing results of the ANN model II 2-2-4-1 for energy absorption prediction.

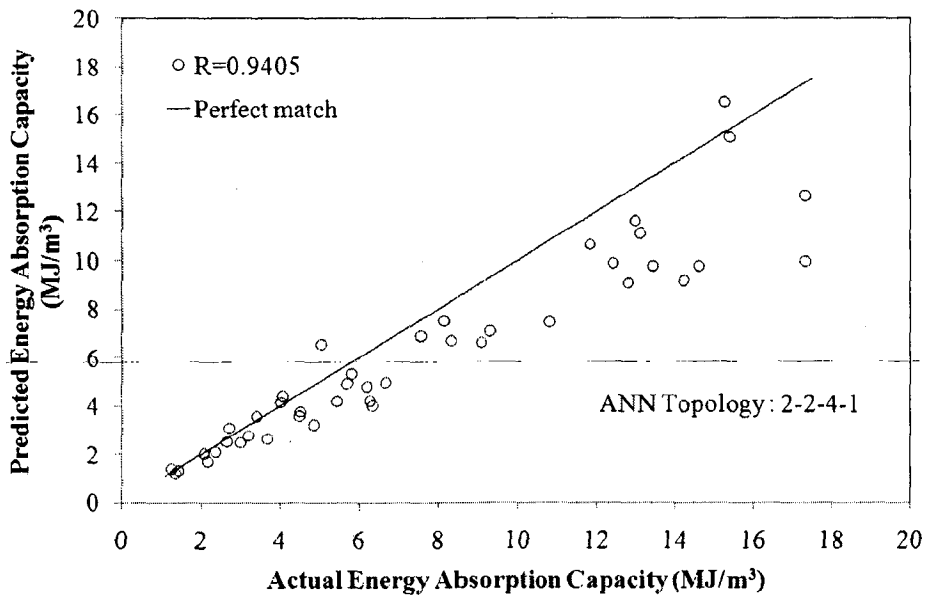


Fig. 4.65. Performance evaluation of model II simulation results for energy absorption by comparison with the experimental values.

The obtained model II is tested with data not considered for training and the model prediction is shown in Fig. 4.64. The mean square error for testing is 1.27×10^{-2} . The predicted results of the model are plotted against the corresponding experimental

results along with perfect match line and shown in Fig. 4.65. The correlation coefficient, $R=0.9405$ is observed between the prediction and the actual values, indicating the results obtained are satisfactory.

4.5.3. Inference from Modelling

Statistical models have been successfully used for the prediction of mechanical properties of closed-cell aluminum foam in compression such as plateau stress, Young's modulus and energy absorption capacity. Once the simple observable structural characteristics of closed-cell foam: relative density, average pore diameter and cell aspect ratio is known, these models can simulate their corresponding compressive properties. Of the two statistical modelling techniques used, the multiple linear regression analysis gives the correlation equations for each model. These simple correlation equations can be easily used for the prediction of compressive properties. The prediction accuracy of these models tested with the experimental data sets gave the coefficients of correlation above 0.90 for all developed models. However, the ANN modelling technique has shown its ability to handle non-linear problems effectively by giving better model prediction accuracy with coefficient of correlation values greater than 0.95, in general, for compressive properties, except that for Young's modulus model at 0.9249.

All the models developed by both modelling tools are of acceptable accuracy and found to be satisfactory and are in good agreement with experimental results. These modelling techniques offer a better alternative where analytical modelling is difficult and highly involved due to the complex relationships arising due to the heterogeneous structure of foam. Both the regression models and the ANN models developed in this work will be beneficial to the foam manufactures and also to the design engineers to design the desired foam characteristics and also to adopt this material for suitable structural applications.

Chapter 5

CONCLUSIONS

Light and stiff structures made of aluminum foam/foam sandwich panels can replace components made of conventional materials in the automobile, rail and aerospace industry, thereby reducing the vehicular weight and substantially reducing fuel consumption. Along with reduced weight, aluminum foams provide safety by improving crash worthiness due to its unique property to efficiently absorb and dissipate impact energy. Metal foam as structural elements will additionally provide thermal insulation and vibration damping which are attractive features for the transportation sector.

The melt foaming route to process closed-cell aluminum foam by degassing TiH_2 , which has the potential for producing foam on commercial scale was studied to analyze process parameter – foam structure – mechanical property correlation. It was necessary to

demonstrate the reproducibility and reliability of metal foam before it can challenge conventional materials as a better alternative. To this end, the important inferences drawn from the present work are summarised under four sections below:

a) Process analysis and its influence of macrostructure.

It was necessary to add 4 wt.% copper to 6061 aluminum alloy for foaming to occur. The copper addition caused the formation of aluminum dendrites with Al_2Cu lamella present as a continuous network throughout the microstructure. TiH_2 addition and degassing in a calcium modified melt is a liquid process route with several parameters which influence the foam macrostructure. In the present work, aluminum foams were synthesised with density ranging from 0.17 to 1.08 g/cm^3 , average pore diameter varying from 2.116 to 4.495 mm and cell aspect ratio varying from unity to 1.36.

Preliminary experiments helped identify that (i) the amount of calcium metal addition, (ii) the stirring time after calcium addition, (iii) the amount of TiH_2 addition and (iv) the holding time after TiH_2 addition are the four important process parameters which allow us to access a wide range of foam structure. Design of experiments methodology was adapted to further refine the study and to quantitatively identify the most significant process parameters. In the first phase of experiments, half-fractional factorial experimental design revealed that (i) the amount of TiH_2 addition and (ii) the holding time after TiH_2 addition as the most significant process parameters to tailor the foam structure. In the second phase of experiments, central composite design along with the response surface methodology helped identify the type of dependence of structural parameters such as the relative density, pore size and cell aspect ratio on the two most significant process parameters identified earlier.

The relative density exhibited maximum variation with the amount of TiH_2 addition in comparison to the holding time. The nonlinear behaviour typically shows saturation in relative density at about 1.25 wt.% TiH_2 addition, beyond which there is no further decrease in relative density. On the other hand, the average pore diameter increases with the amount of TiH_2 addition and holding time proportionally, though the mechanism is different. The increase in pore size with amount of TiH_2 addition is probably due to the agglomeration of TiH_2 particles in the melt. On the other hand, the pore size increase with holding time is due to the drainage of melt leading to coalescence

of cells. The cell wall collapse is dominant beyond 1 wt.% TiH₂ and 100 s holding time which causes additional load on the remaining cell edges leading to increased cell aspect ratio transverse to the foaming direction.

b) Microstructural analysis and stability of foam structure.

The X-ray analysis of the extracted particles from the cell wall materials revealed the presence of intermetallics and oxides such as Al₂Ca, TiAl₃, Al₂CuO₄ and Al₂O₃. Additionally, the EDS analysis indicated the presence of lamellar Al₂Cu and blocky Al₂₀CaTi₄ precipitates within the cell wall. In the foams synthesized with stainless steel stirrer, Al₁₃Fe₄ as elongated platelets are seen within the cell walls. The elemental area map confirmed the presence of intermetallics within the cell walls, whereas the Al₂O₃ oxide film is confined to the surface of the pores. The SEM micrographs have shown the sizes of the dispersed intermetallics to be in the tens of micrometer range. TEM micrographs of the cell wall indicate the presence of nano sized particles dispersed within the aluminum matrix in between the coarse intermetallics.

Alloying with copper and calcium addition to the melt before TiH₂ degassing are important steps taken to modify the melt viscosity to enhance foamability. Additionally, the morphology of intermetallics present in the cell wall play an important role in hindering drainage and thereby promote stability which is defined as delaying cell wall rupture leading to coarsening. For example, Al₁₃Fe₄ as high aspect ratio platelets retard the pressure difference driven drainage of metal from the cell face to the cell edge enabling better control of the foam structure. However, Al₁₃Fe₄ particles make the foam slightly brittle in nature thereby negating the advantage of having higher plateau stress to obtain higher energy absorption capacity.

c) Mechanical property and analysis.

The stress strain curve in compression showed typical foam characteristics of the elastic region followed by the extended plateau stress until densification strain when the stress increases sharply. The Al₁₃Fe₄ containing foam showed higher plateau stress, but due to the brittle nature of the cell walls, the energy absorption capacity was rather limited and not considered further. Young's modulus in the range of 0.1 – 2.7 GPa, plateau stress in the range of 1 – 32 MPa, densification strain in the range of 54 – 86 %

and energy absorption capacity in the range of 1 – 19 MJ/m³ are reported for a wide range of foam structures assessed in the present work. The improved plateau stress and energy absorption capacity, better than those reported in the literature for similar foams, is attributed to strengthening due to particle dispersion in the aluminum cell wall material down to the hundreds of nm scale.

The mechanical properties show a direct dependence on relative density as the Gibson and Ashby model suggests. For a given relative density, the plateau stress increases with pore diameter due to the increasing cell wall thickness. However, the disparity in the prediction of the Gibson and Ashby model is attributed to the non-uniformity associated with the actual foam structure, uncertainty in the determination of cell wall material property and the estimation of ϕ , which is the fraction of solid contained in the cell edges.

Dynamic compression tests were carried out on the split Hopkinson's pressure bar apparatus in the strain rate range of $5 \times 10^2 - 1 \times 10^3 \text{ s}^{-1}$ which is commensurate with automobile impact velocities. The resulting plateau stress, which ranged from 1 to 45 MPa, showed improvement over quasi-static test values proportional to the relative density. In the strain rate range tested, a strain rate sensitivity variation of 0.18 to 0.59 is reported for relative density variation of 0.15 to 0.25, respectively. The increased plateau stress value at high strain rate, which is an attractive feature for high velocity impact absorption applications of foam could be due to (i) dynamic compression concentrating deformation to a thin section, (ii) micro-inertia associated with rotation and lateral motion of cell walls and/or (iii) higher compressible resistance of the cell fluid.

d) Statistical modelling and analysis.

Analytical modelling approach such as the Gibson and Ashby model which assumes regular and repetitive cell structure falls short as they are far removed from the actual foam structure. Mathematical modelling was undertaken to predict the mechanical properties of aluminum foam with a few easily measurable structural parameters as input variables. The empirical relationships developed by multiple linear regression model for Young's modulus, plateau stress and energy absorption capacity confirmed their strong dependence on relative density and are useful for easy prediction of aluminum foam property.

The complex nature of the aluminum foam structure and its importance in determining the foam properties calls for an involved statistical modelling approach such as ANN. The non-linear mapping power of ANN is exploited to predict the mechanical properties of foam using the same structural parameters as input variables. The predictive capability of the ANN model was better than the multi-linear regression model with the same input parameters. The multi-linear regression and ANN models developed are useful for predicting the mechanical properties of foam on the basis of known, easily quantifiable structural parameters and will serve as a useful guiding tool for design engineers to process foam with required properties for specific engineering applications.

Chapter 6

SCOPE FOR FUTURE WORK

This research work was undertaken with the objective to optimize the processing of aluminum foam by TiH_2 degassing to achieve properties which will be attractive enough to replace conventional materials in the automobile, rail and aerospace industry. Foams which are lighter than water with better plateau stress, energy absorption capacity and work hardening under dynamic impact conditions hold good promise. Along with the weight saving and safety aspects, there are economics and reliability issues which need to be addressed before foams can become acceptable replacements. The present work has thrown up some materials engineering problems quite unique to metallic foams, highlighting their difference from polymeric foams, which call for fundamental studies of their mechanical behaviour. Some of these issues are highlighted below as areas for future research endeavour.

1. Aluminum foam processed from the liquid state is expected to have a cast structure with inferior properties. But, it has been shown that the alloying and precipitation of intermetallics down to the nano-scale improves the properties by pinning grain boundaries and/or hindering dislocation motion. The influence of the particle scale effects on strengthening of the cell walls need to be studied in conjunction with alloying additives and cooling rate.
2. Analytical modelling approaches have been quite successful in predicting the properties of polymeric foams due to the regularity of the structure. Those equations are invalid due to the inhomogeneity of the metal foam structure in the macroscale. To account for this, statistical modelling approaches have been found to be fairly successful in the present work. But to accurately model metallic foams, important factors such as the cell size distribution, wall thickness and shape needs to be considered.
3. The present work has shown that the extended plateau region and work hardening effects at sub-critical velocity impact conditions are desirable properties for automotive applications. It is understood that when individual cell walls break, the load is distributed to the other cells until the layer collapse. Additionally, the knowledge of the cell wall collapse behaviour under fatigue conditions is also important. It will be interesting to know how the material degradation progresses under cyclic loading when individual cell walls rupture.
4. Metal foams are usually produced near net shaped. Joining and repair of foams is an entirely unexplored area. Both metallurgical and mechanical joining solutions such as welding, mechanical fastening and adhesive bonding need to be explored.
5. The use of aluminum foam in ship building industry is gaining significance to obtain light and stiff structures making use of the natural buoyancy of closed-cell foam. In this context, corrosion studies in harsh environments such as NaCl need to be undertaken, as this is also a problem for automobiles in coastal regions.

REFERENCES

- [1] Allen, B.C., (1963), US Patent 3,087,807.
- [2] Andrews, E., Sanders, W. and Gibson, L.J., (1999), "Compressive and tensile behaviour of aluminum foams", *Mater. Sci. and Eng. A.*, Vol. 270, pp. 113–124.
- [3] Andrews, E.W., Gioux, G., Onck, P. and Gibson, L.J., (2001), "Size effects in ductile cellular solids. Part II: experimental results", *Int. J. of Mechanical Sci.*, Vol. 43, pp. 701-713.
- [4] Asavavisithchai, S. and Kennedy, A.R., (2006), "The effect of Mg addition on the stability of Al-Al₂O₃ foams made by a powder metallurgy route", *Scripta Mater.*, Vol. 54, pp. 1331-1334.
- [5] Ashby, M.F., (2005), "Materials Selection in Mechanical Design", Butterworth-Heinemann, An imprint of Elsevier, Burlington, MA.
- [6] Ashby, M.F., Evans, A.G., Fleck, N.A., Gibson, L.J., Hutchinson, J.W., and Wadley, H.N.G., (2000), "Metal Foams: A Design Guide", Butterworth-Heinemann, Boston.
- [7] Asholt, P., (1999), "Metal foams and porous metal structures", In: Banhart, J., Ashby, M.F., Fleck, N.A., editors. *Int. Conf.*, Bremen, Germany, 14–16 June. Bremen: MIT Press–Verlag.
- [8] Babcsan, N., Leitlmeier, D. and Banhart, J., (2005), "Metal foams – high temperature colloids part I- Ex-situ analysis of metal foams", *Colloids and Surfaces A: Physicochem Eng Aspects*, Vol. 261, pp. 123-130.
- [9] Babcsan, N., Leitlmeier, D. and Degischser, H.P., (2003), "Foamability of particle reinforced aluminum melt", *Mat.-wiss. U. Werkstofftech*, Vol. 34, pp. 22-29.
- [10] Babcsan, N., Leitlmeier, D., Degischser, H.P. and Banhart, J., (2004), "The role of oxidation in blowing particle-stabilised aluminium foams", *Adv. Eng. Mater.*, Vol. 6, pp. 421-428.
- [11] Banhart, J. and Baumeister, J., (1998), "Deformation characteristics of metal foams", *J. of Mater. Sci.*, Vol. 33, pp. 1431-1440.
- [12] Banhart, J., (1999), "Foam metal: The recipe", *Europhysics*, Vol. 30, pp. 17-20.
- [13] Banhart, J., (2001), "Manufacture, characterisation, and application of cellular metals and metal foams", *Progress in Mater. Sci.*, Vol. 46, pp. 559-632.

- [14] Banhart, J., (2005), "Aluminium foams for lighter vehicles", *Int. J. Vehicle Design*, Vol. 37, pp. 114-124.
- [15] Banhart, J., (2006), "Metal Foams: Production and Stability", *Adv. Eng. Mater.*, Vol. 8, pp. 781-794 .
- [16] Baumeister, J., Banhart, J. and Weber, M., (1997), "Aluminium foams for transport industry", *Materials & Design*, Vol. 18, pp. 217-220.
- [17] Berry, C.B., (1972), US Patent 3,669,654.
- [18] Bezerra, E.M., Ancelotti, A.C., Pardini, L.C., Rocco, J.A.F.F., Iha, K. and Ribeiro, C.H.C., (2007), "Artificial neural networks applied to epoxy composites reinforced with carbon and E-glass fibers: Analysis of the shear mechanical properties", *Mat. Sci. and Eng. A.*, Vol. 464, pp. 177-185.
- [19] Bin, J., Zejun, W. and Naiqin, Z., (2007), "Effect of pore size and relative density on the mechanical properties of open cell aluminum foams", *Scripta Mater.*, Vol. 56, pp. 169-172.
- [20] Bjorksten, J. and Rock, E.J., (1972), US Patent 3,707,367.
- [21] Bram, M., Stiller, C., Buchkremer, H.P., Stover, D. and Baur, H., (2000), "High-porosity titanium, stainless steel, and superalloy parts", *Advanced Engineering Materials*, Vol. 2, pp. 196-199.
- [22] Cao, X.Q., Wang, Z.H., Ma, H.W., Zhao, L.M. and Yang, G.T., (2006), "Effects of cell size on compressive properties of aluminum foam", *Trans. Nonferrous Met. Sci. China*, Vol. 16, pp. 351-356.
- [23] Chen, C. and Lu, T.J., (2000), "A phenomenological framework constitutive modelling of incompressible and compressible elasto-plastic solids", *Int. J. of Solids and Structures*, Vol. 37, pp. 7769-7786.
- [24] Chen, W. and Ravichandran, G., (1997), "Dynamic compressive failure of a glass ceramic under lateral confinement," *J. Mech. Phys. Solids*, Vol. 45, pp. 1303-1328.
- [25] Chen, W., Subhash, G. and Ravichandran, G., (1994), "Evaluation of ceramic specimen geometries used in split Hopkinson pressure bar," *DYMAT J.*, Vol. 1, pp. 193-210.

- [26] Chen, W., Zhang, B. and Forrestal, M.J., (1999), "A split Hopkinson bar technique for low-impedance materials," *Experimental Mechanics*, Vol. 39, pp. 81-85.
- [27] Cherepin, V.K., and Mallik, A.K., (1967), "Experimental techniques in physical metallurgy", Asia publishing house, Mumbai, India.
- [28] Cochran, G. and Cox, G.M., (1962), "Experimental Design", Asia publishing house, New Delhi.
- [29] Contorno, D., Filice, L., Fratini, L. and Micari, F., (2006), "Forming of aluminum foam sandwich panels: Numerical simulations and experimental tests," *J. of Mat. Proc. Technol.*, Vol.177, pp. 364-367.
- [30] Daniel, B.S.S. and Edwin Raj, R., (2007), "Criteria for foam stabilisation in aluminum foam synthesis", *Sixteenth International Conference on Processing and Fabrication of Advanced Materials*, pp. 63-68, Singapore.
- [31] Daniel, J.S., Chehab, G.R. and Kim, Y.R., (2004), "Issues Affecting Measurement of the Complex Modulus of Asphalt Concrete", *J. Mater. in Civil Eng.*, Vol. 16, pp. 469-476 .
- [32] Dannemann, K., and Lankford, J., (2000), "High strain rate compression of closed-cell aluminium foams," *Mater. Sci. and Eng. A.*, Vol. 293, pp. 157-164.
- [33] Degischer, H.P., (1997), "Innovative light metals: metal matrix composites and foamed aluminium", *Materials & Design* , Vol. 18, pp. 221-226.
- [34] Demsetz, L.A and Gibson, L.J., (1987), "Minimum weight design for stiffness in sandwich plates with rigid foam cores," *Mat. Sci. and Eng.* Vol.85, pp. 33-42.
- [35] Deqing, D., Weiwei, X., Xiangjun, M. and Ziyuan, S., (2005), "Cell structure and compressive behaviour of an aluminum foam", *J. of Mater. Sci.*, Vol. 40, pp. 3475-3480.
- [36] Deqing, D., Weiwei, X., Xiangjun, M. and Ziyuan, S., (2006), "Effect of processing parameters on cell structure of an aluminum foam", *Mater. Sci. and Eng. A.*, Vol. 420, pp. 235-239.
- [37] Deqing, W. and Ziyuan, S., (2003), "Effect of ceramic particles on cell size and wall thickness of aluminum foam", *Mater. Sci. and Eng. A.*, Vol. 361, pp. 45-49.
- [38] Deshpande, V.S. and Fleck, N.A., (2000), "Isotropic constitutive models for metallic foams", *J. of the Mech. and Physics of Solids*, Vol. 48, pp. 1253-1283.

- [39] Deshpande, V.S., and Fleck, N.A., (2000), "High strain rate compressive behaviour of aluminum alloy foams," *Int. J. of Impact Eng.*, Vol. 24, pp. 277-298.
- [40] Doyoyo, M. and Mohr, D. (2006), "Experimental determination of the mechanical effects of mass density gradient in metallic foams under large multiaxial inelastic deformation," *Mechanics of Mater.*, Vol. 38, pp. 325-339.
- [41] Draper, N.R. and Smith, H., (1966), "Applied regression analysis", John Wiley & Sons, Inc., USA.
- [42] Edwin Raj, R. and Daniel, B.S.S., (2007a), "Aluminum melt foam processing for light-weight structures", *Mat. & Manuf. Processes*, Vol. 22, pp. 525-530.
- [43] Edwin Raj, R. and Daniel, B.S.S., (2007b), "Manufacturing challenges in obtaining tailor-made closed-cell structure in metallic foams", *Int. J. Adv. Manuf. Technol.*, doi 10.1007/s00170-007-1254-y.
- [44] Edwin Raj, R. and Daniel, B.S.S., (2008a), "Structural and compressive property correlation of closed-cell aluminum foam", *J. of Alloys and Compd.*, doi:10.1016/j.jallcom.2007.12.040.
- [45] Edwin Raj, R. and Daniel, B.S.S., (2008b), "Prediction of compressive properties of closed-cell aluminum foam using artificial neural network", *Computational Mater. Sci.*, doi:10.1016/j.commat.2008.01.041.
- [46] El Kadi, H., (2006), "Modelling the mechanical behaviour of fiber-reinforced polymeric composite materials using artificial neural networks—A review", *Compos. Struct.*, Vol. 73, pp. 1-23.
- [47] Elbir, S., Yilmaz, S., Tokso, A.K. and Guden, M., (2003), "SiC-particulate aluminum composite foams produced by powder compacts: Foaming and compression behaviour", Vol. 38, pp. 4745-4755.
- [48] Elliot, J.C., (1956), US Patent 2,751,289.
- [49] Evans, A.G., Hutchinson, J.W. and Ashby, M.F., (1999), "Multifunctionality of cellular metal systems," *Prog. in Mater. Sci.*, Vol.43, pp. 171-221.
- [50] Fiedler, W.S., (1965), US Patent 3,214,265.
- [51] Follansbee, P.S., (1985), "The Hopkinson bar," *Mechanical Testing, Metals handbook*, 9th ed., American Society for Metals, Metals Park, OH, pp. 198-217.
- [52] Freeman J.A. and Skapura D.M., (1991), "Neural Network Algorithms, Applications and Programming Techniques", Addison-Wesley Publishing Company, Inc., New York.

- [53] Frew, D.J., Forrestal, M.J. and Chen, W., (2001), "A split Hopkinson pressure bar technique to determine compressive stress-strain data for rock materials", *Experimental Mechanics*, Vol. 41, pp. 40-46.
- [54] Frew, D.J., Forrestal, M.J. and Chen, W., (2002), "Pulse shaping techniques for testing brittle materials with a split Hopkinson pressure bar," *Experimental Mechanics*, Vol. 42, pp. 93-106.
- [55] Fushong, H. and Zhengang, Z., (1999), "Mechanical behaviour of foamed aluminum", *J. mater. Sci.*, Vol. 34, pp. 291-299.
- [56] Gibson, L.J. and Ashby, M.F., (1997), "Cellular solids, structures and properties", 2nd ed. Cambridge University Press, UK.
- [57] Gibson, L.J., Ashby, M.F., Zhang, J. and Triantafillou, T.C., (1989), "Failure surfaces for cellular materials and multiaxial loads: Part I. Modelling", *Int. J. of Mechanical Sci.*, Vol. 31, pp. 635-663.
- [58] Greene, S.A., Hall, I.W. and Guden, M., (2002), "Improving the energy absorption of closed cell aluminum foams," *J. of Mate. Sci. Letters*, Vol.21, pp. 1591-1593.
- [59] Haibel, A., Rack, A. and Banhart, J., (2006), "Why are metal foams stable? ", *Appl. Phys. Lett.*, Vol. 89: 154102, pp. 1-3.
- [60] Han, F., Cheng, H., Wang, J. and Wang, Q., (2004), "Effect of pore combination on the mechanical properties of an open cell aluminum foam," *Scrip. Mater.*, Vol.50, pp. 13-17.
- [61] Hansen, A.G., Hopperstad, O.S., Langseth, M. and Ilstad, H., (2000), "Validation of constitutive models applicable to aluminum foams", *Int. J. of Mechanical Sci.*, Vol. 44, pp. 359-406.
- [62] Hardy, P.W. and Peisker, G.W., (1967), US Patent 3,300,296.
- [63] Hayden, N.G.W., (2002), "Cellular metals manufacturing", *Adv. Eng. Mater.*, Vol. 4, pp. 726-733.
- [64] Haykin, S., (2004), "Neural Networks A Comprehensive Foundation", Pearson Education, Inc., Singapore.
- [65] Hosseini, S.M.K., Hanzaki, Z.A., Parah, Y.M.J. and You, S., (2004), "ANN model for prediction of the effects of composition and process parameters on tensile

- strength and percent elongation of Si-Mn TRIP steels”, *Mat. Sci. and Eng. A.*, Vol. 374, pp. 122-128.
- [66] Hsiang, S.H. and Kuo, J.L., (2005), “Applying ANN to predict the forming load and mechanical property of magnesium alloy under hot extrusion”, *Int. J. Adv. Manuf. Technol.*, Vol. 26, pp. 970-977.
- [67] Huang, C.Z., Zhang, L., He, L., Sun, J., Fang, B., Zou, B., Li, Z.Q. and Zhang, L., (2002), “A study on the prediction of the mechanical properties of a ceramic tool based on an artificial neural network”, *J. of Mat. Proces. Technol.*, Vol. 129, pp. 399-402.
- [68] Ip, S.W., Wang, Y. and Toguri, J.M., (1998), “Aluminum foam stabilization by solid particles”, *Canadian Metallurgical Quarterly*, Vol. 38, pp. 81-92.
- [69] Jiang, Z., Zhang, Z. and Friedrich, K., (2007), “Prediction on wear properties of polymer composites with artificial neural networks”, *Composites Sci. and Technol.*, Vol. 67, pp. 168-176.
- [70] Jiejun, W., Chenggong, L., Dianbin, W. and Manchang, G., (2003), “Damping and sound absorption properties of particle reinforced Al matrix composite foams”, *Composites Sci. and Technology*, Vol. 63, pp. 569–574.
- [71] Kanahashi, H., Mukai, T., Yamada, Y., Shinojima, K., Mabuchi, M., Nich, T.G., and Higashi, K., (2000), “Dynamic compression of an ultra-low density aluminum foam,” *Mater. Sci. and Eng. A.*, Vol. 280, pp. 349-353.
- [72] Kanthal Handbook, “Appliance heating alloys”, Kanthal lab, Hallstahammer, Sweden.
- [73] Kennedy, A.R. and Asavavisithchai, S., (2004a), “Effect of ceramic particle additions on foam expansion and stability in compacted Al-TiH₂ powder precursors”, *Adv. Eng. Mater.*, Vol. 6, pp. 400-402.
- [74] Kennedy, A.R. and Asavavisithchai, S., (2004b), “Effects of TiB₂ particle addition on the expansion, structure and mechanical properties of PM Al foams,” *Scrip. Mater.* Vol.50, pp. 115–119.
- [75] Kennedy, A.R. and Lopez, V.H., (2003), “The decomposition behaviour of as-received and oxidized TiH₂ foaming-agent powder”, *Mater. Sci. and Eng. A*, Vol. 357, pp. 258-263.

- [76] Kennedy, A.R., (2002), "The effect of TiH₂ heat treatment on gas release and foaming in Al-TiH₂ preforms", *Scripta Mater.*, Vol. 47, pp. 763-767.
- [77] Kenny, L.D., (1996), In: *Materials science forum*, Vol. 217-222. Switzerland: Transtec Publications.
- [78] Kim, A., Hasan, M.A., Nahm, S.H. and Cho, S.S., (2005), "Evaluation of compressive mechanical properties of Al-foams using electrical conductivity", *Composite Structures*, Vol. 71, pp. 191-198.
- [79] Kishan Mehrotra, Chilukuri K. Mohan and Sanjay Ranka, (1997), "Elements of Artificial Neural Networks", Penram International Publishing, India.
- [80] Kolsky, H., (1949), "An investigation of mechanical properties of materials at very high rates of loading," *Proc. Phys. Soc. Lon. B*, Vol. 62, pp. 676-700.
- [81] Konstantinidis, I.Ch., Papadopoulos, D.P., Lefakis, H. and Tsipas, D.N., (2005), "Model for determining mechanical properties of aluminum closed-cell foams," *Theoretical and Appl. Fracture Mechanics*, Vol.43, pp. 157-167.
- [82] Korner, C., Arnold, M, Thies, M. and Singer, R.F., (2002), "The physics of foaming: Structure, formation and stability", IN *Handbook of cellular metals*, edited by Degischer, H.-P. and Kriszt, B., Wiley-VCH Verlag GmbH, Weinheim.
- [83] Korner, C., Arnold, M. and Singer, R.F., (2005), "Metal foam stabilization by oxide network particles", *Mater. Sci. and Eng. A*, Vol. 396, pp. 28-40.
- [84] Kovacik, J., (1998), "The tensile behaviour of porous metals made by Gasar process", *Acta Materialia*, Vol. 46, pp. 5413-5422.
- [85] Koza, E., Leonowicza, M., Wojciechowska, S., Simancik, F., (2003), "Compressive strength of aluminium foams", *Materials Letters*, Vol. 58, pp. 132-135.
- [86] Kurauchi, T., Sato, N., Kamigaito, O. and Komatsu, N., (1984), "Mechanism of high energy absorption by foamed materials -foamed rigid polyurethane and foamed glass", *J. of Mater. Sci.*, Vol. 19, pp. 871-880.
- [87] Lee, Y.C., Dahle, A.K. and Stjon, D.H., (2000), "The role of grain refinement of magnesium", *Metallurgical and Materials Transaction*, Vol. 31A, pp. 2895- 3000.
- [88] Leitlmeier, D., Degischer, H.P. and Flankl, H.J., (2002), "Development of a foaming process for particle reinforced aluminum melts", *Adv. Eng. Mater.*, Vol. 4, pp. 735-740.

- [89] Li, B.-Y., Rong, L.-J., Li, Y.-Y., and Gjunter, V. E., (2000), "An investigation of the synthesis of Ti-50 At. Pct. Ni alloys through combustion synthesis and conventional powder sintering", *Metallurgical and Materials Transactions A*, Vol. 31, pp. 1867-1871.
- [90] Li, M., Liu, X. and Xiong, A., (2002), "Prediction of the mechanical properties of forged TC11 titanium alloy by ANN", *J. of Mat. Proces. Technol.*, Vol. 121, pp. 1-4.
- [91] Lu, T.J., and Ong, J.M., (2001), "Characterization of close-celled cellular aluminum alloys", *J. of Mater. Sci.*, Vol. 36, pp 2773 – 2786.
- [92] Ma, L. and Song, Z., (1998), "Cellular structure control of aluminium foams during foaming process of aluminium melt" *Scripta Mater.*, Vol. 39, pp. 1523–1528.
- [93] Mangapatnam Adamvalli and Venkitanarayanan Parameswaran, (2007), "Dynamic strength of adhesive single lap joints at high temperature," *Int. J. of Adhesion and Adhesives*, doi:10.1016/j.ijadhadh.2007.10.005.
- [94] Mark Evans, (2003), "Optimisation of manufacturing processes: A response surface approach", Maney Publishing, London.
- [95] Markaki, A.E. and Clyne, T.W., (2001), "The effect of cell wall microstructure on the deformation and fracture of aluminum-based foams", *Acta Mater.*, Vol. 49, pp. 1677-1686.
- [96] Martin T. Hagan, Howard B. Demuth and Mark Beale, (1996), "Neural Network Design", Vikas Publishing House Pvt. Ltd., New Delhi.
- [97] Matijasevic, B.-L., Banhart, J., Fiechter, S., Gorke, O. and Wanderka, N., (2006), "Modification of titanium hydride for improved aluminium foam manufacture", *Acta Mater.*, Vol. 54, pp. 1887–1900.
- [98] Matijasevic, B. and Banhart, J., (2006), "Improvement of aluminum foam technology by tailoring of blowing agent", *Scripta Mater.*, Vol. 54, pp. 503-508.
- [99] McBride, J., Malinov, S. and Sha, W., (2004), "Modelling tensile properties of gamma-based titanium aluminides using artificial neural network", *Mat. Sci. and Eng. A.*, Vol. 384, pp. 129-137.

- [100] McCormack, T.M., Miller, R., Kesler, O. and Gibson, L.J., (2001), "Failure of sandwich beams with metallic foam cores", *Int. J. of Solids and Structures*, Vol. 38, pp. 4901-4920.
- [101] McCullough, K.Y.G., Fleck, N.A. and Ashby, M.F., (1999), "Toughness of aluminium alloy foams", *Acta mater.*, Vol. 47, pp. 2331-2343.
- [102] Miller, R., (2000), "Continuum plasticity model for the constitutive and indentation behaviour of foamed metals", *Int. J. of Mechanical Sci.*, Vol. 42, pp. 729-754.
- [103] Miyoshi, T., Itoh, M., Mukai, T., Kanahashi, H., Kohzu, H., Tanabe, S. and Higashi, K., (1999), "Enhancement of energy absorption in a closed-cell aluminum by the modification of cellular structures," *Scripta Mater.*, Vol. 41, pp. 1055-1060.
- [104] Mondal, D.P., Ramakrishnan, N., Suresh, K.S. and Das, S., (2007), "On the moduli of closed-cell aluminum foam", *Scripta Mater.*, Vol. 57, pp. 929-932.
- [105] Montanini, R., (2005), "Measurement of strain rate sensitivity of aluminum foams for energy absorption", *Int. J. of Mechanical Sci.*, Vol. 47, pp. 26-42.
- [106] Montgomery, D.C., (2001), "Design and analysis of experiments", 5th ed. John Wiley & Sons. Inc., India.
- [107] Mukai, T., Kanahashi, H., Miyoshi, T., Mabuchi, M., Nieh, T.G., Higashi, K., (1999), "Experimental study of energy absorption in a closed-celled aluminum foam under dynamic loading," *Scrip. Mater.*, Vol. 40, pp. 921-927.
- [108] Mukai, T., Miyoshi, T., Nakano, S., Somekawa, H. and Higashi, K., (2006), "Compressive response of a closed-cell aluminum foam at high strain rate", *Scripta Mater.*, Vol. 54, pp. 533-537.
- [109] Nasser, N.S., Kang, W.J., McGee, J.D., Guo, W.G. and Isaacs, J.B., (2007), "Experimental investigation of energy-absorption characteristics of components of sandwich structures," *Int. J. of Impact Eng.*, Vol.34, pp. 1119-1146.
- [110] Niebylski, L.M., Jarema, C.P. and Lee, T.E., (1974), US Patent 3,816,952.
- [111] Olurin, O.B., Fleck, N.A. and Ashby, M.F., (2000), "Deformation and fracture of aluminum foams", *Mater. Sci. and Eng. A*, Vol. 291, pp. 136-146.
- [112] Onck, P.R., (2001), "Application of a continuum constitutive model to metallic foam Den-Specimen in compression", *Int. J. of Mechanical Sci.*, Vol. 43, pp. 2947-2959.

- [113] Onck, P.R., Andrews, E.W. and Gibson, L.J., (2001), "Size effects in ductile cellular solids: Part I. Modelling," *Int. J. of Mechanical Sci.*, Vol.43, pp. 681–699.
- [114] Papadopoulos, D.P., Konstantinidis, I.Ch., Papanastasiou, N., Skolianos, S., Lefakis, H. and Tsipas, D.N., (2004), "Mechanical properties of Al metal foams," *Materials Letters*, Vol.58, pp. 2574– 2578.
- [115] Paserin, V., Marcuson, S., Shu, J. and Wilkinson, D.S., (2004), "CVD technique for Inco nickel foam production", *Adv. Eng. Mater.*, Vol. 6, pp. 454-459.
- [116] Paul, A., and Ramamurty, U., (2000), "Strain rate sensitivity of a closed-cell aluminum foam," *Mater. Sci. and Eng. A.*, Vol. 281, pp. 1-7.
- [117] Queheillalt, D.T., Choi, B.W., Schwartz, D.S., and Wadley, H.N.G., (2000), "Creep expansion of porous Ti-6Al-4V sandwich structures", *Metallurgical and Materials Transactions A*, Vol. 31, pp. 261-273.
- [118] Queheillalt, D.T., Hass, D.D., Sypeck, D.J., and Wadley, H.N.G., (2001), "Synthesis of open-cell metal foams by templated directed vapor deposition", *Journal of Materials Research*, Vol. 16, pp. 1028-1036.
- [119] Rajasekaran, S. and Pai, G.A.V., (2003), "Neural network, fuzzy logic and genetic algorithms synthesis and applications", Prentice-Hall of India Pvt. Ltd., New Delhi.
- [120] Ramachandra, S., Kumar, S.P. and Ramamurty, U., (2003), "Impact energy absorption in an Al foam at low velocities," *Scripta Mater.*, Vol.49, pp. 741-745.
- [121] Ramamurty, U. and Kumaran, M.C., (2004), "Mechanical property extraction through conical indentation of a closed-cell aluminum foam," *Acta Mater.*, Vol.52, pp. 181–189.
- [122] Ramamurty, U. and Paul, A., (2004), "Variability in mechanical properties of a metal foam", *Acta Mater.*, Vol. 52, pp. 869–876.
- [123] Ravichandran, G. and Subash, G., (1994), "Critical appraisal of limiting strain rates for compression testing of ceramics in split Hopkinson pressure bar," *J. American Ceramic Soc.*, Vol. 77, pp. 263-267.
- [124] Ray, S., (1993), "Review synthesis of cast metal matrix particulate composites", *J. of Mater. Sci.*, Vol. 28, pp. 5397-5413.
- [125] Renault, G.M., (2008), "Lightweight vehicle design: contribution to fuel savings", Guyancourt –France, Available Website dated 13-05-08:
www.materia.coppe.ufrj.br/mirror/sarra/artigos/artigo10107/index.html

- [126] Robinson, M and Carruthers, J., 2007, 'Composite applications in rail industry', Int. conf. on recent advances in composite materials, Allied publishers Pvt. Ltd., New Delhi, pp. 348-357.
- [127] Ross, C.A., (1996), "Moisture and strain rate effects on concrete strength," *ACI Mat. J.*, Vol. 93, pp. 293-300.
- [128] Ruan, D., Lu, G., Chen, F.L., and Siores, E., (2002), "Compressive behaviour of aluminum foams at low and medium strain rate," *Composite Structures*, Vol. 57, pp. 331-336.
- [129] Ryan, T.P., (1990), "Handbook of statistical methods for engineers and scientists – Linear regression", 2nd edition, edited by Harrison M. Wadsworth, The McGraw-Hill Companies, Inc., USA.
- [130] Schroers, J., Veazey, C., and Johnson, W.L., (2003), "Amorphous metallic foam", *Applied Physics Letters*, Vol. 82, pp. 370-372.
- [131] Schwingel, D., Seeliger, H.W., Vecchionaces, C., Alwes, D. and Dittrich, J., (2007), "Aluminium foam sandwich structures for space application," *Acta Astronautica*, Vol.61, pp. 326-330.
- [132] Seeliger, H.-W., (2004), "Aluminum foam sandwich (AFS) ready for market introduction", *Adv. Eng. Mater.*, Vol. 6, pp. 448-451.
- [133] Simancik, F. and Kovacik, J., (2002), "Electrical, thermal and acoustic properties of cellular metals", In – *Handbook of cellular metals*, edited by Degischer, H.-P. and Kriszt, B., Wiley-VCH Verlag GmbH, Weinheim.
- [134] Simone, A.E. and Gibson, L.J., (1998), "Aluminum foams produced by liquid-state processes", *Acta mater.*, Vol. 46, pp. 3109-3123.
- [135] Singh, H. and Deo, B., (1996), "Prediction of the coke rate in blast furnaces with artificial neural nets", *Fuel and Energy Abstracts*, Vol. 37, pp. 212-220.
- [136] Song, H.W., Fan, Z.J. Yu, G., Wang, Q.C. and Tobota, A., (2005), "Partition nergy absorption of axially crushed aluminum foam-filled hat sections," *Int. J. of Solids and Structures*, Vol.42, pp. 2575-2600.
- [137] Song, Z. and Nutt, S.R., (2007), "Rheology of foaming aluminum melts," *Mater. Sci. and Eng. A*, Vol.458, pp. 108–115.
- [138] Song, Z.-L., Ma, L.-Q., Wu, Z.-J. and He, D.-P., (2000), "Effect of viscosity on cellular structure of foamed aluminum in foaming process", *J. of Mater. Sci.*, Vol. 35, pp. 15-20.

- [139] Song, Z.-L., Zhu, J.-S., Ma, L.-Q. and He, D.-P., (2001), "Evolution of foamed aluminum structure in foaming process", *Mater. Sci. and Eng. A*, Vol. 298, pp. 137-143.
- [140] Sosnik, B., (1948), US Patent 2,434,775.
- [141] Sreeja Kumari, S.S., Pillai, R.M. and Pai, B.C., (2005), "Role of calcium in aluminum based alloys and composites", *Int. Materials Reviews*, Vol. 50, pp. 216-238.
- [142] Sriram, R., Vaidya, U.K. and Kim, J.E., (2006), "Blast impact response of aluminum foam sandwich composites," *J. Mater. Sci.*, Vol.41, pp. 4023-4039.
- [143] Sugimura, Y., Meyer, J., He, M.Y., Bart-Smith, H., Grenstedt, J.L. and Evans, A.G., (1997), "On the mechanical performance of closed cell Al alloy foams", *Acta Mater.*, Vol. 45, pp. 5245-5259.
- [144] Sugishita, J., Fujiyoshi, S., Imura, T., and Ishii, M., (1982), "A study of cast alloys with partially dispersed graphite I: the process of partial dispersion with uncoated carbon microballoons", *Wear*, Vol. 81, pp. 209-220.
- [145] Tekoglu, C. and Onck, P.R., (2005), "Size effects in the mechanical behaviour of cellular materials", *J. of Mater. Sci.*, Vol. 40, pp. 5911–5917.
- [146] Thomas, H.W. and Ronald, J.W., (1981), "Regression: A second course in statistics", John Wiley & Sons, Inc., USA.
- [147] Thomas, M., Kenny, D., and Sang, H., (1997), U. S. Patent 5,622,542.
- [148] Triantafillou, T.C., Zhang, J., Shercliff, T.L., Gibson, L.J. and Ashby, M.F., (1989), "Failure surfaces for cellular materials and multiaxial loads: Part II. Comparison of models with experiment", *Int. J. of Mechanical Sci.*, Vol. 31, pp. 665-678.
- [149] Tzeng, S.-C. and Ma, W.-P., (2006), "A novel approach to manufacturing and experimental investigation of closed-cell Al foams", *Int. J. Adv. Manuf. Technol.*, Vol. 28, pp. 1122-1128.
- [150] Wang, Y., (1995), "Aluminum foam stabilization by solid particle", A thesis for the degree of master of applied science, University of Toronto.
- [151] Weaire, D. and Hutzler, S., (1999), "The physics of foams", Oxford University. New York.

- [152] Wood, J., (1998), "Metal foams", In: Banhart, J. and Eifert, H., editors. Proc. Fraunhofer USA Symposium on Metal Foams, Stanton, USA, Bremen: MIT Press-Verlag.
- [153] Wubben, T., Stanzick, H., Banhart, J., and Odenbach, S., (2003), "Stability of Metallic Foams Studied under Microgravity", *Journal of Physics - Condensed Matter*, Vol. 15, PP. 427-433.
- [154] Wubben, T.H., Odenbach, S., (2005), "Stabilisation of liquid metallic foams by solid particles", *Colloids and Surfaces A: Physicochem Eng Aspects*, Vol. 266, pp. 207-213.
- [155] Yamada, Y., Shimojima, K., Sakaguchi, Y., Mabuchi, M., Nakamura, M., Asahina, T., Mukai, T., Kanahashi, H., and Higashi, K., (1999), "Processing of an Open-Cellular Z91 Magnesium Alloy with a Low Density of 0.05 g/cm³", *Journal of Materials Science Letters*, Vol. 18, pp. 1477-1480.
- [156] Yang, C.C. and Nakae, H., (2000), "Foaming characteristics control during production of aluminum alloy foam", *J. of alloys and Compounds*, Vol. 313, pp. 188-191.
- [157] Yang, C.C. and Nakae, H., (2003), "The effect of viscosity and cooling conditions on the foamability of aluminum alloy", *J. of Mater. Process. Technol.*, Vol. 141, pp. 202-206.
- [158] Yang, D.H., Hura, B.Y., He, D.P. and Yang, S.R., (2007), "Effect of decomposition properties of titanium hydride on the foaming process and pore structures of Al alloy melt foam," *Mater. Sci. and Eng. A*, Vol.445-446, pp. 415-426.
- [159] Yi, F., Zhu, Z., Zu, F., Hu, S., and Yi, P., (2001), "Strain rate effects on the compressive property and energy-absorbing capacity of aluminum alloy foams," *Materials Characterization*, Vol. 47, pp. 417-422.
- [160] Yu, C.-J., Eifert, H.H., Banhart, J., and Baumeister, J., (1998), "Metal foaming by a powder metallurgy method: production, properties and applications", *Materials Research Innovations*, Vol. 2, pp. 181-188.
- [161] Yu, H., Guo, Z., Li, B., Yao, G., Luo, H. and Liu, Y., (2007), "Research into the effect of cell diameter of aluminum foam on its compressive and energy absorption properties", *Mat. Sci. and Eng. A.*, Vol. 454-455, pp. 542-546.

- [162] Yu, H., Yao, G., Wang, X., Liu, Y. and Li, H.,(2006), "Sound insulation property of Al-Si closed-cell aluminum foam sandwich panels", *Applied Acoustics*, Vol.68, pp. 1502-1510.
- [163] Zhang, Z. and Friedrich, K., (2003), "Artificial neural networks applied to polymer composites: a review", *Composites Sci. and Technol.*, Vol. 63, pp. 2029-2044.

LIST OF PUBLICATION

Journals:

1. R. Edwin Raj, B.S.S. Daniel, "Aluminum melt foam processing for light-weight structures", *Materials and Manufacturing Processes*, Taylor & Francis Group, Vol.22, pp 525-530, 2007.
2. R. Edwin Raj, B.S.S. Daniel, "Manufacturing challenges in obtaining tailor-made closed-cell structures in metallic foams", *International Journal for Advanced Manufacturing Technology*, Springer. DOI 10.1007/s00170-007-1254-y (Available online)
3. R. Edwin Raj, B.S.S. Daniel, "Structural and compressive property correlation of closed-cell aluminum foam", *Journal of Alloys and Compounds*, Elsevier Publications. DOI: 10.1016/j.jallcom.2007.12.040 (Available online)
4. R. Edwin Raj, B.S.S. Daniel, "Structural property correlation with process parameters in the manufacture of closed-cell aluminum foam", *Journal of Manufacturing Engineering*. (In Press)
5. R. Edwin Raj, B.S.S. Daniel, "Prediction of compressive properties of closed-cell aluminum foam using artificial neural network", *Computational Materials Science*. Elsevier Publications. (Available online)
6. R. Edwin Raj, B.S.S. Daniel, "Microstructural influence in closed cell aluminum foam for structural application", *International Journal of Microstructure and Materials properties*, Inderscience Publishers. (Accepted)
7. R. Edwin Raj, B.S.S. Daniel, "Evaluation and prediction of energy absorption capacity of closed-cell aluminum foam using artificial neural network", *Soft Materials*, Taylor & Francis Group. (Under review)
8. R. Edwin Raj, B.S.S. Daniel, "Assessment of mechanical properties and energy absorption capacity of closed-cell aluminum foam", *Metallurgical and Materials Transaction B*, Springer. (In preparation)
9. R. Edwin Raj, B.S.S. Daniel, "Design of process variables influencing foam structure in processing closed-cell aluminum foam", *Materials Science and Engineering A*. Elsevier Publications. (In preparation)

P. Venkitanarayanan

10. R. Edwin Raj, B.S.S. Daniel, "Dynamic compression property analysis in comparison with quasi-static condition of closed-cell aluminum foam", Journal of Alloys and Compounds, Elsevier Publications. (In preparation)

Conferences:

11. R. Edwin Raj, M.S. Khan, P. Gupta, P.K. Ghosh and B.S.S. Daniel, "Development of Metallic Foam by Gas Dispersion in Molten Aluminum", Proceedings of the International Conference on Advanced Materials Design & Development 2005, Goa, pp 96-97, (2005).
12. R. Edwin Raj, B.S.S. Daniel, "Aluminium Melt Foam Processing for Light Weight Structures" , Proceedings of the International Conference on Advances in Material and Materials Processing 2006, IIT Kharagpur, pp 877-883, (2006)
13. R. Edwin Raj, B.S.S. Daniel, "Manufacturing challenges in obtaining tailor-made closed cell structures in metallic foam", 1st International & 22nd AIMTDR Conference, IIT Roorkee, pp 503-508, (2006).
14. R. Edwin Raj, B.S.S. Daniel, "Mechanical behaviour of calcia modified closed-cell aluminum foams processed by TiH₂ decomposition", International Symposium for Research Scholars on Metallurgy, Materials Science and Engineering, IIT Madras, pp 800-805, (2006).
15. R. Edwin Raj, B.S.S. Daniel, "Aluminum foam for ultra light weight structures and energy absorption", International Conference on Recent Advance in Materials & Processing, PSG Tech, Coimbatore, pp 72-73, (2006).
16. R. Edwin Raj, B.S.S. Daniel, "Structural and mechanical property correlation in closed-cell aluminum in-situ composite foam", Second International Conference on Recent Advances in Composite Materials, IT-BHU, New Delhi, pp 948-952, (2007).
17. B.S.S. Daniel, R. Edwin Raj, "Criteria for foam stabilisation in aluminum foam synthesis", Sixteenth International Conference on Processing and Fabrication of Advanced Materials, 63-68 December 2007, Singapore.